Describing motions in biological tissues: a continuum active model and improving measurements

Michał Józef Bogdan

Department of Engineering
University of Cambridge

This dissertation is submitted for the degree of
Doctor of Philosophy

Trinity College September 2019

Declaration

This dissertation is the result of my own work. It includes nothing which is the outcome of collaboration except where specifically indicated in the text. This dissertation contains fewer than 65,000 words including appendices, footnotes, captions, tables and equations. It has fewer than 150 figures. It is an account of work done under the supervision of Dr Thierry Savin in the Department of Engineering of the University of Cambridge. None of it has been previously submitted to satisfy a degree requirement at any institution. This PhD thesis reproduces large exerpts from my published articles [1, 2], distributed through the text.

Michał Józef Bogdan
September 2019

Abstract

Describing motions in biological tissues: a continuum active model and improving measurements

Michał Józef Bogdan

Motions in biological tissues strongly influence their properties and are crucial for their functions. This is true starting from the scale of single molecules, all the way up to the scale of entire tissues. One of the key properties distinguishing motions in living systems from those in dead matter is activity: using chemical energy to generate self-propulsion. Effective theoretical, physics-based models are necessary both to interpret the rich new experimental observations in the field of biological motions, and to properly account for the inherent errors of the experimental methods. In this work we study models related to motion both on the level of tissues and individual molecules.

One of our models is driven by the observation that many growing tissues form multicellular protrusions at their edges. It is not fully understood how these are initiated, therefore we propose a minimal continuum physical model to suggest a possible mechanism. We apply our model to a growing circular tumour. We employ our approach to understand how activity affects the tumour's dynamics and the tendency to form "fingers" at its boundary. This approach rests on just four key biophysical parameters and we can estimate them based on experiments described in the literature. Our modelling of a tumour is experimentally well justified and analytically solvable in many systems. It is, to the best of our knowledge, the first analytical description of tumour interface dynamics incorporating the activity of the tumour bulk. We can explain the propensity of tissues to fingering instabilities, as conditioned by the magnitude of active traction and the growth kinetics. We are also able to derive predictions

for the tumour size at the onset of metastasis, and predictions for the number of subsequent invasive fingers.

Microscopy-based techniques are essential for observing biological motions at all aforementioned length scales. Brownian particle videotracking is one example of such a technique. In the second part of this thesis, we apply physics-based theory to understand inherent errors and limitations of this method. Using analytic solutions and simulations, we show the effects of errors in particle videotracking on recovering energy landscapes from the distributions of Brownian particles. We point out mechanisms that result in nontrivial systematic biases in the measurements.

Acknowledgements

I would like to thank my supervisor, Dr. Thierry Savin for years of endless support and fruitful collaboration. I would like to thank my advisor, Dr. Vikram Deshpande, for practical advice. Interdisciplinary research, such as this, requires collecting bits of expertise and a fresh eye from specialists in various areas. I would therefore like to thank Dr. Jaques Prost, Dr. Sergio Lira, Dr. Adrien Hallou, Dr. Piotr Szymczak and Dr. Pierre Recho for their insightful comments on my research, and also to thank Caroline Giuglaris for her comments on the first draft of my thesis. I am also grateful to my examiners, Dr. Alexandre Kabla and Dr. Chiu Fan Lee, for their constructive feedback and resultant improvements to the thesis.

I would like to thank my colleagues and friends in Cambridge and abroad, both in the lab and beyond, for their support and providing a steppingstone over the course of these years.

I am especially grateful for the support of my family: Mum and Dad, Artur and Asia. Thank you for your understanding and patience in difficult moments and for discussions on the first draft of my thesis.

Table of contents

Preface: motions in biological systems

All living species carry out certain key functions which distinguish them from dead matter[1]. These functions depend, among other factors, on motions across multiple length scales. Note we mention "motions" in plural. This is because there exists a wide range of species, carrying out multiple functions, each of which in turn utilizes different, numerous motion-based processes.

Examples start with those most apparent from everyday life, on the length scale of meters. It is on this length scale that we use motion of muscles to move the rest of our bodies and find shelter and food, swallow, drink, breathe and reproduce.

Directed motion carried out by muscles is necessary because distances covered by diffusion scale as a square root of time, while those covered by directed motion scale linearly with time, making the latter mode much more efficient on longer distances. The larger the length scales involved, the more complex and fine-tuned the mechanisms to conduct the motions efficiently: for example, the transport of blood in millimeter-sized organisms, such as insects, takes place openly across the cavities of the entire body, while larger animals need closed veins and arteries to efficiently carry it out.

An exhaustive review of motions with biological functions within this thesis would not be plausible. Ultimately, we formulate and examine several questions in this broad field. They are grouped into two separate research projects: one in each of the two categories (diffusive motion and directed motion) described above. One of them (Part II of this thesis) is related to measuring diffusive motion of individual bio-molecules. In this project we assess analytically and numerically the consequences of motion blur for the accuracy of using Brownian particle tracking to measure energetic landscapes. The other project (Part I of this thesis) focuses on modelling collective motion of cells during tissue growth. We design and explore a minimal model of fingering at the edges of growing, active carcinomas. We deal separately with each of the projects, starting with a comprehensive review of the relevant literature to present context for our work, proceeding to stating our hypothesis and conclusions. We now turn to the latter topic in detail.

---

[1] A website of the US National Cancer Institute, *https://training.seer.cancer.gov/anatomy/body/functions.html*, defines these as *organization, metabolism, responsiveness, movements, and reproduction*, adding that humans are also characterized by *growth, differentiation, respiration, digestion, and excretion*

Part I

Fingering instabilities in tissue invasion: an active fluid model

Chapter 1

Introduction

In this part of the thesis we are motivated by fingering patterns observed at the edges of growing cancers, which seem to be the first step to fatal cancer invasion of other tissues (metastasis). Inspired by reports that cancer cells actively exert forces on their surroundings, we are interested in whether these fingering patterns could result from a physical instability caused by active self-propulsion of cancer cells. We ultimately design a theoretical model that analytically tests this hypothesis in a simplified system, discusses its predictions and opportunities for testing them. However, to understand fully the need for our model, its experimental motivations, as well as the possibilities and limitations of present experimental methods to verify its predictions, a broad review of relevant literature is needed. It deals with all phenomena and concepts which are relevant to our work. It first covers available knowledge about physical properties of the relevant types of tissues and transformations they undergo, about collective motion of these tissues in general and circumstances in which fingering at their edges is observed in particular. It proceeds to biophysics of cancer and metastasis. It later discusses the role of activity and interfacial instabilities in biological systems. Ultimately, it describes the "how we know what we know": the experimental methods providing the data, which helps explain the limits to what we know and what we need to model.

1.1 Growth processes

Coordinated movements of large groups of cells are common in biological organisms. This in general takes place wherever there is large-scale tissue growth: during morphogenesis (the gradual growth of an embryo into a fully developed organism), wound healing and growth of malignant tumours. We focus on the latter two areas, since this is most relevant to our research.

In this context, we need to introduce and briefly discuss epithelial tissue. It is considered one of the four main types of animal tissue. It covers various interfaces inside the body, including surfaces of blood vessels, often forming effectively 2 dimensional layers, both *in vivo* and *in vitro* [3]. It is very important for our ultimate goal because it is frequently the place of formation of primary tumours [4–8]. Tumours originating in epithelial tissues are called carcinomas and constitute a vast majority of cancers. Mature epithelial tissue is quite coherent and solid-like, with cells holding tightly to each other [6, 3, 9]. This is a result of strong cell-cell adhesion, mediated by cell-cell junctions (such as tight junctions- parts of strongly adhering membrane [8]- and slightly weaker adherens junctions [8]). Cells of this tissue are typically not very motile, except for special circumstances, which we discuss later. Young epithelial tissue, on the other hand, tends to be more motile. The inhibition of its motion, together with increasing density, occurs as maturity is achieved [9]. Together, the growth in density and reduction in motility is referred to as contact inhibition of motion [10]. Some research on human bronchial epithelial cells, however, suggests it is the maturation of adhesion proteins and strengthening of cell-cell contacts that is key to the dynamical arrest, and not the increasing density [9]. The process becomes reversed during wound healing and cancerogenesis, when epithelial tissue becomes motile again.

1.1.1 Wound healing experiments

The reepithalisation, or restoration of destroyed epithelial tissue, is an element of the process of wound healing. *In vitro* experiments, in which epithelial layers on a substrate invade empty space, have been carried out to simulate wound healing [11, 12].

The invasion is usually studied when the tissues achieve characteristics of maturity. This includes confluence (lack of free space between cells) [11, 14]. The area available to invade is subsequently provided by removing a part of the layer or by removing a physical barrier, which previously inhibited motion in some of the directions. The invasion of the freed space is carried out by a wide front of the tissue. However, multi-cellular fingers at the boundary of the layer, which move faster than the bulk of the front, emerge [11, 13, 14]- see Fig. (1.1).

The growth of tissue area and resulting invasion occurs partly by proliferation in the bulk of the tissue and partly by increase in cell size close to the front [15], visible also in Fig. (1.1).

In most experimental settings, the cells adhere quite strongly to each other, and local neighbor rearrangements are rare. Many of the local rearrangements that do happen occur as a result of cell division, which has the potential to cause small vortexes of circulating cells [15, 16]. However, in general, vorticity is much higher in non-flowing tissues [15].

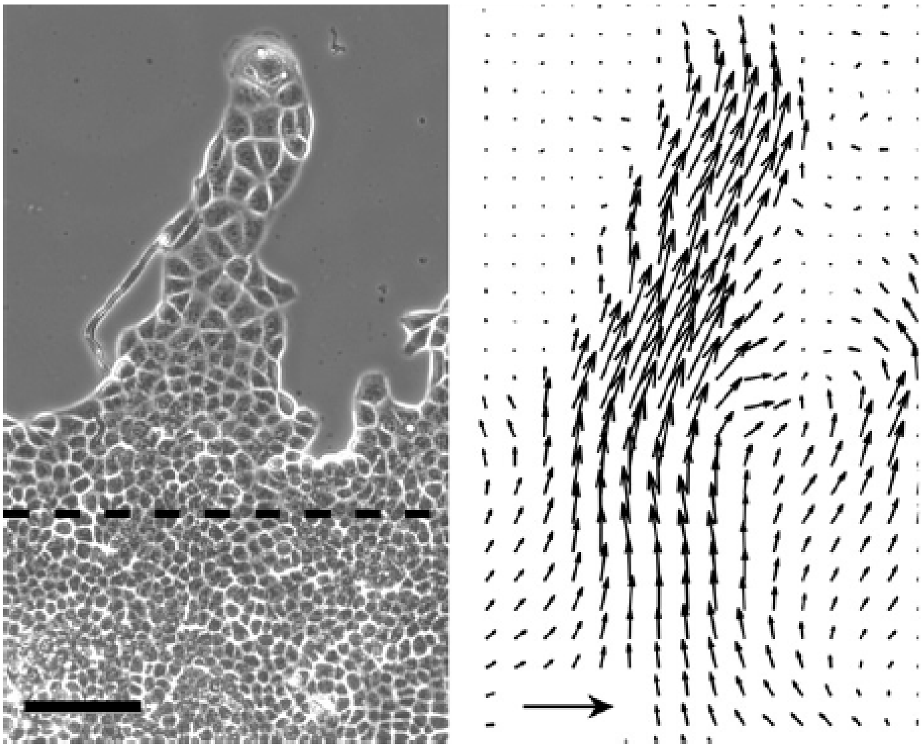

Fig. 1.1 Edges of an epithelia cell culture invading empty space. Velocity fields shown on the right. Pictures taken 22 hours after removal of a barrier (located along the dashed line). Scale bar of $100\mu m$. Re-printed from [13]

Experiments were also conducted to explore how epithelial tissues invade channels, adjacent to the tissue bulk. Invasion of wide channels, whose width is comparable to distances at which velocities of cells are correlated, or larger, is carried out in a complex manner, with the emergence of large-scale swirls [17, 18]. Invasion of narrower channels, on the other hand, has a simpler picture, with all cells travelling essentially in the direction of front propagation [18]; the process occurs much faster in narrower, than in wider channels [18].

An interesting experiment studied what happens after 2 growing cell sheets touch, with the conclusion that a stable front is formed even if the interactions between cells in each of the layers are weak, and both layers contain tissue of the same type. This led to speculation that jamming (inhibition of motion due to lack of free space to move in high density) might be the reason for formation of 2-dim stable fronts between tissues [19].

1.1.2 Motion within epithelial tissue

It is also instructive to examine how epithelial cells move within the tissue itself. As an epithelial sheet grows to cover empty space, swirls are generated within the tissue, even far from its edge [17].

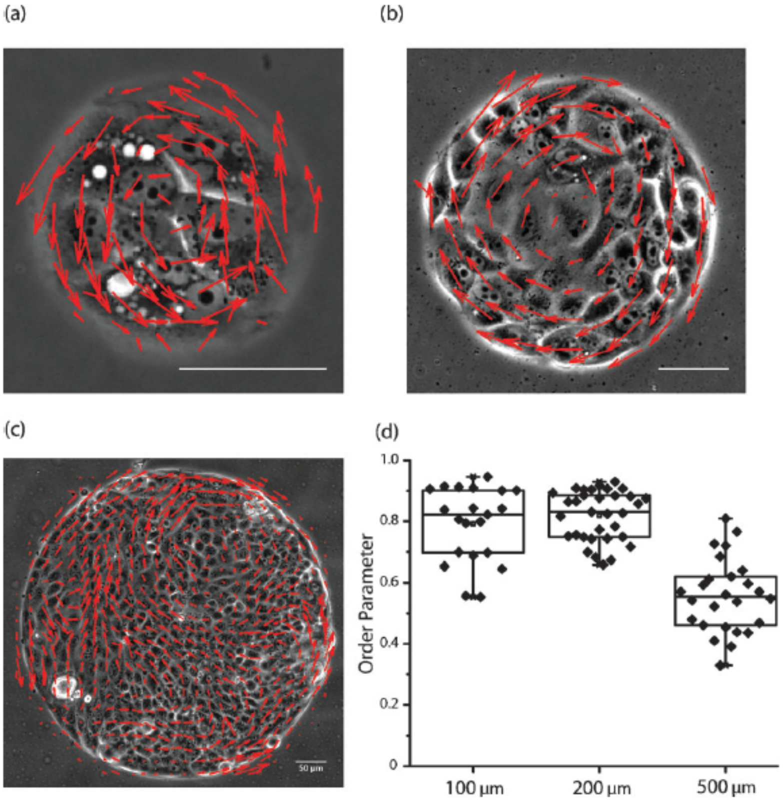

Fig. 1.2 Patterns of collective motion in epithelial cell colonies [20]. Larger patches of tissue do not get dominated by a single pattern of motion [20], as evidenced by a decreasing order parameter when diameter exceeds a certain threshold(d). Scalebars represent $50\mu m$. Graphics from [20].

Very interesting behaviours are observed in cultures of young epithelial cells, grown on artificial substrates. While cell density in the colony is small (before reaching confluence), cells move with persistent Brownian motion (as they do individually [21]). As they approach confluence and achieve it, directions of motion of neighboring cells become correlated [22] (some authors even describe this phenomenon as a kinetic phase transition between a disordered and ordered state [22]), and they start to form multi-cellular swirls (see Fig.1.2) [3]. The size of the swirls increases with growing cell density, while the magnitude of the velocity decreases at the same time [3]. Interestingly, cell cultures grown on smaller patches get dominated, over a certain density, by a single swirl, which is circular in a circularly shaped colony [23, 20].

The size of the colony at which its domination by a single pattern breaks down is close to the typical swirl size in larger colonies of the same cell type and density [20]. The increase of swirl size and decrease of cell velocity with growing density culminates in a dynamical arrest, in which the tissue basically stops flowing [3]. Experimental studies of this process [3], as well as simulation results, suggest this bears close phenomenological similarities with the classical glassy transition [3, 9], in which quickly cooling fluids undergo dynamical arrest,while maintaining amorphous structure. The analogy with the glassy transition encapsulates both general and certain detailed hallmarks [3].

1.2 Cancer growth and metastasis

Growth of epithelial tumours

Cancer is responsible for a large percentage of human deaths (estimated at 15.7 % as of 2015 [24]. While the global death rates for many other diseases- infectious, strokes, heart attacks- have greatly decreased in the previous decades, progress in decreasing the death rate due to cancer has been much slower. Finding successful treatment strategies is so difficult partly because cancer is in fact an entire diverse group of over 200 diseases [25]. Its common feature is a pathological, uncontrollable and rapid growth of a group of cells in the body.

One of the main hallmarks of cancer originating in epithelial tissue is the loss of the epithelial properties by cells, such as strong adhesion and inhibited mobility and acquirement, partially or completely, the phenotype of mesenchymal tissue [25]. It is an embryonic, primitive and functionally unspecified type of tissue, characterized by very loosely interacting and motile cells. It is quite common in early developmental processes of the body and is necessary for morphogenesis [26]. This process of phenotypic transformation is often called the epithelial to mesenchymal transition [27].

Metastasis is the phenomenon of cancer cells leaving the primary tumour and subsequently establishing secondary tumours in other parts of the body. It causes a vast majority of cancer-related deaths [28, 25]. Indeed, the potential to metastasize is what differentiates between deadly cancer, suggestively also referred to as malignant tumour, and equally suggestively named benign tumour, which cannot metastasize and is therefore most often harmless. Because of its large complexity and huge variability of employed strategies [29], despite decades of research, metastasis is still not very well understood [25].

However, new experimental techniques have provided a wealth of experimental results on this process. This challenges the scientific community with the task of comprehensively understanding the underlying principles governing metastasis. We discuss what the current conclusions and speculations based on these results are, with a focus on cancers originating in epithelial tissue (carcinoma).

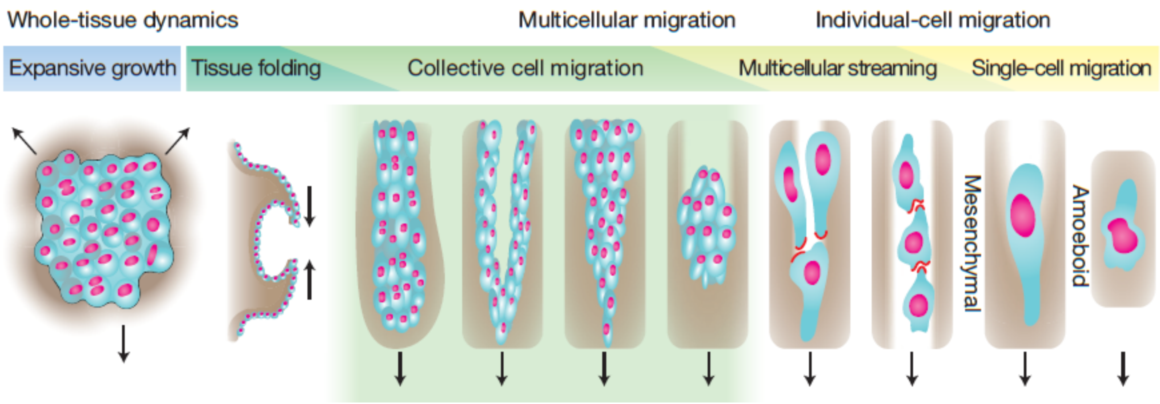

Fig. 1.3 An illustration of types of cancer invasion. Reprinted from [29]

Metastatic invasion can be roughly decomposed into 3 phases: (1) leaving of primary tumour by cancer cells and their motion through neighboring tissue (2) their entry into the bloodstream and (3) their extravasation from the bloodstream and formation of secondary tumors in new organs [25]. Since our work is related to phase (1) of this process, we mainly discuss experimental findings related to this phase.

The aforementioned, enormous variety of cancer diseases also manifests itself on the stage of invasion from the primary tumour into surrounding tissue. Employed invasion mechanisms vary and are partially organ-specific. However, this variety can be largely broken up into a group of patterns. A classification of cancer invasion was proposed (see Fig. 1.3) [29]. It features the following types of invasion: (1) single cell invasion, (2) multi-cellular streaming, (3) collective, cohesive cell migration and (4) expansive growth. In fact, a nearly continuous spectrum of modes between these types is observed.

(1) Individual cell migration mostly occurs in leukaemias and lymphomas (cancers of white blood cells and the lymphatic system, respectively). It is much less common than various types of collective migration [29]. It can be further classified into mesenchymal invasion and amoeboidal invasion. In the mesenchymal invasion mode cells are very motile and elongated. They use various strategies to move, frequently remodelling surrounding extracellular matrix (ECM). They are able to do this by applying proteolysis (the breakdown of proteins- see Fig. (1.4)) and cell-matrix adhesion [29]. Amoeboid invasion is carried out by rounded cells with a large ability for manipulating their shape and exerting capillary-like motion. It is an alternative mechanism of individual migration, less dependent on adhesion than individual mesenchymal migration [29, 5]. Since our work is not relevant to individual migration, it was just noted here for completeness and we do not discuss it further.

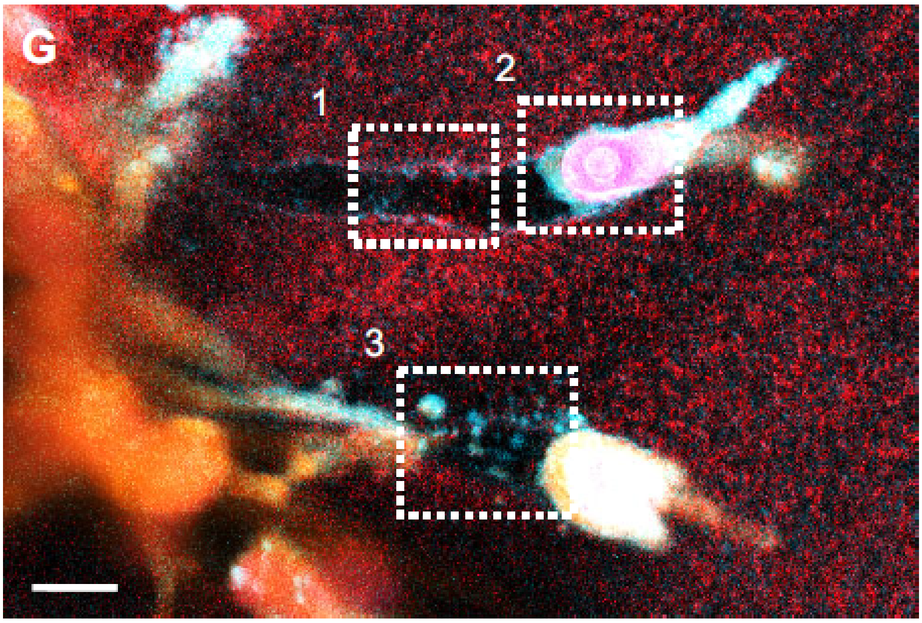

Fig. 1.4 Proteolysis of collagen matrix by invading fibrosarcoma (cancer of fibrous connective tissue) cells. Cells are visible in white (dashed box no. 2). Proteolytic tracks (dashed boxes no. 1 and 3) are visible in black on the dotted red background, representing the collagen matrix Scale bar represents $20\mu m$. Reprinted from [30].

(2) Multicellular streaming refers to a subgroup of migratory modes. Their common feature is the fact that entire groups of cells pursue directed motion, separately generating force on the surrounding matrix, while direct intercellular adhesions are very weak and temporary [29]. It can take the form of directed motion of groups of cells without any direct contact, small clusters moving together, or, most frequently, fingers of adhering cells moving in environmentally conditioned or self-generated tracks. The boundary between this type of migration and (3) collective, cohesive cell migration is somewhat fluid; the latter occurs when invasion is led by clusters of strongly adhering cells. Multicellular streaming can display various morphologies [29]; these include one- or two- cell wide fingers [29], knife-like structures, which are led by a leader cell capable of proteolising surrounding ECM and generating high traction forces on the ECM and subsequently widened by following cells [29] or wide fronts. The structures described here can be very coherent, such that individual cells far from the edge may be almost deprived of any contacts with the ECM [29]. The invasion can be also led by fibroblasts (a type of connective tissue), while cells far from the edge can participate in the invasion without losing their epithelial traits [29].

(3) Collective cell motion is widely employed by cancer. It has been long established that epithelial cells can move collectively, not only in cancer, but also in developmental processes, and the fact that mesenchymal cells can also perform collective motion with quite stable junctions between cells has been established quite recently. It can happen especially in response to confinement and jamming, when the cells' mutual contacts strenghten [31]. Collective migration is especially common for the extremely common breast and lung carcinomas [25]. Our work specifically aims at modelling and understanding this type of invasion.

For completeness, we also mention (4) expansive growth, which is a form of passive invasion, in which individual cells are deprived of any motility and press on the surrounding ECM or tissue because of proliferation and growth. This mode seems to be insufficient in itself to cause malignancy and metastatic invasion.

Determinants of collective metastasis

It seems that the parameters determining the occurring invasion mode include the strength of cell-cell adhesion and force traction levels; cell-ECM adhesion and forces, environmental confinement, and others. We are mostly interested in collective invasion, so describe the properties of the tissue that make it possible.

Biochemical markers related to the choice of invasion mode include, among others: proteases (enzymes carrying out proteolysis), which form migratory paths by degrading obstacle tissues [32]; integrin (a transmembrane receptor responsible for cell- ECM adhesion and force transmission to and from the cell, by connecting to actin filaments of the cell cytoskeleton); cadherin (a molecule responsible for cell-cell adhesion and force transmission [32]). The way these biochemical markers affect cancer invasion is usually by programming biophysical properties, such as adhesion strength (like in the case of aforementioned cadherins and integrins), motility, and tendency for directed migration [33], so understanding of biochemical factors in collective cell migration is often complementary to understanding biophysical factors.

External environmental conditions also play an important role in choosing the invasion mode. The important environmental parameters include the surrounding ECM dimension, stiffness (large ECM rigidity reinforces protrusion formation and, consequently, cell migration [5]) and spatial organization [5, 29] and ECM building material, with some work showing matrigel much more favourable to collective migration than collagen [34]. The width of available tracks and pores in the ECM is also important. Cells switch from individual to collective migration (with leader cells) due to larger density of collagen and smaller porosity of the artificial ECM matrix; the changes in ECM stiffness seem less important. Cells seem to adjust their own properties to enable migration under changing external conditions [5].

In vivo the surroundings the tumour invades tend to be highly heterogenous and complex [35, 30], with the presence of ECM, collagen bundles, membranes, fat cells, muscle and nerve fibers and microvessels, among others [35, 30]. Collective cancer invasion in vivo frequently proceeds in tracks along muscle and nervous fibers [35, 30]; sometimes these are widened by invading cancer cells, while sometimes the cells adjust their shape [35]. Proteolysis (see Fig. 1.4) and remodelling of ECM by leader cells has also been observed [30]. The presence of leader cells, distinct phenotypically from the cells following them, is an aspect of the fact that primary tumours are heterogenous objects in their own, with various cells carrying out various tasks.

The occurrence of collective migration also strongly depends on properties of the cells themselves, including strength of cell-cell and cell-ECM adhesions (respectively controlled by cadherins and integrins) and behaviour of the cytoskeleton (influencing the shapes of the cell) [5]. It seems that the onset of aggressive invasion is often enabled by the occurrence of the epithelial to mesenchymal transition in the primary tumour and especially the following changes of the cells that go with it: decreased adhesiveness between cells and increased motility [34, 27].

Proteolysis- the partial dissolution and remodelling of ECM and other barriers by cells- facilitates collective migration [36, 34]. Remodelled layers of ECM are observed in the neighborhood of travelling cancer cell strands in breast cancer, for example, as well as near the bulk of the tumour in cultures embedded in matrigel [34]. Mesenchymal cells remodel the surrounding matrix using proteolysis, and the created microtracks are later available for collective invasion [34]; follower cells tend to widen the tracks, using proteolysis as well; migration is possible without it, but more difficult [36]; in vivo microscopic techniques confirm ECM degradation and accumulation of collagen fibers in areas of invasion [37]. Blocking proteolysis in vitro may result in transition to individual, amoeboid-like invasion [38]

The role of heterogeneity in the properties of cells within a tumour seems important [25]. Tumour heterogeneity complicates diagnostics [39] and enhances metastasis [40, 41, 34, 42].

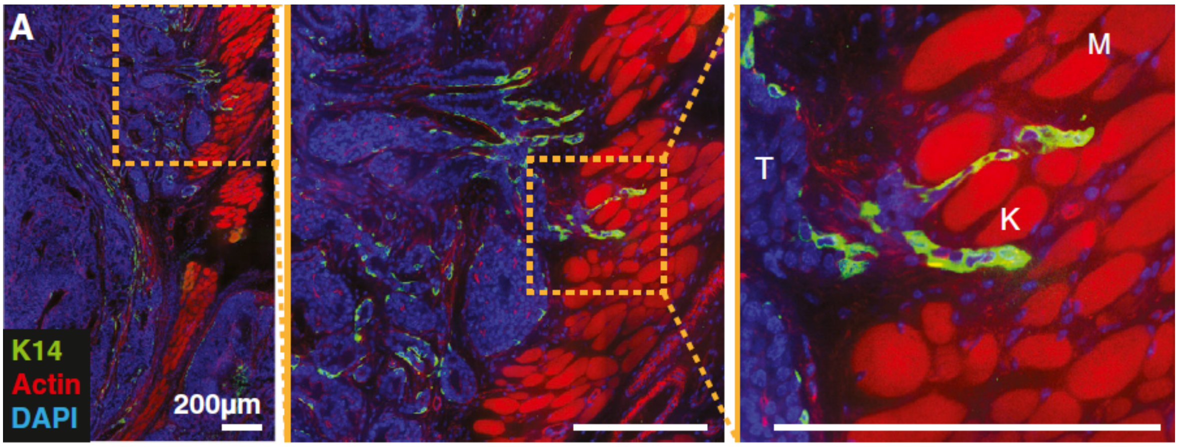

Fig. 1.5 Invasion of fluorescently stained mammary tumour (blue & green) into muscle (red). Green represents leader cells. Scalebar represents $200\mu m$. Reprinted from [40].

In vitro and *in vivo* studies show cancer cells of various combinations of mesenchymal or epithelial phenotype [42] are intermixed with stromal cells [34, 43]. The role of heterogeneity was confirmed in well-controlled conditions [40, 34], in matrigel and collagen artificial ECM [40, 34]. It seems that a subgroup of motile, mesenchymal cells has the role of leading collective invasion [34]. Leader cells (see Fig. 1.5) have a dual role here: (1) they individually migrate through the ECM, partially dissolving it via proteolysis, leaving behind microtracks of remodelled ECM, easier to penetrate for collective invasion [34, 42]; (2) They lead a front of collective invasion of heterogeneous cell groups by maintaining contacts with epithelial and less motile cells in the bulk of the invading tumour [40, 34, 42]; the invading cell groups then flood and expand the tracks [34].

1.3 Active motions

Activity, in our usage of the term, is the use of chemical energy by living systems to apply forces to their surroundings and generate mechanical energy and self-propelled motion, and active motions are ones generated according to this principle. They are a key ingredient in biological systems and are used by all living organisms. From nanometer-sized systems, such as transport of microscopic cargo along microtubules [44], to macroscopic ones, such as flight of birds and everywhere in between, they play essential roles, being arguably one of the fundamental physical hallmarks of life. Since we later model the role of activity might play in fingering seen at the edges of carcinomas, we go over the topic of active motions in more detail.

Much research into this type of motions is focused on understanding how large groups of active particles behave collectively. This raises many important questions on the fundamental level, since many key results of traditional physics do not apply to assemblies of such particles [45–47]. Many questions have to also be answered on the practical level: what types of motion and behaviour do we expect to observe in a specific active biological system? To name one example, turbulence is the answer in the case of certain bacterial suspensions [48].

Ample experimental evidence shows that cells also move by active self-propulsion [13, 49–53]. This also applies to the motions in wound healing and cancer we previously discussed.

Cells in two dimensional epithelial colonies move by exerting traction on the substrate. The traction is largely exerted by lamellipodia- protrusions of the cell which form at the leading edge and then pull the cell behind [54]. In the past it was supposed that cells at the edge of the tissue exert most of the traction [55, 52]. We now know this is not true and traction is exerted across the entire layer of the tissue [52, 53]. The direction of the force cells exert on the substrate is often coupled with their previous direction of motion, and this property alone can explain many observed properties of spreading epithelial layers [56]. This coupling is however, not always the case [57, 58], and the direction of the active force on the substrate can significantly deviate from the direction of the cell motion [58]. It can be influenced by deformations of the substrate [59], chemotaxis, kenotaxis [57] (the tendency of cells to fill empty space) and other phenomena.

1.4 Interfacial instabilities

Interfacial instabilities are a key physical concept, relevant to motions in biology in general and- if our hypothesis is true- to fingering observed at the edges of carcinomas in particular. They are related to the dynamics of interfaces between physical phases, such as between a fluid and a liquid, or between two immiscible fluids. An interfacial instability occurs if the local distribution of forces at the interface makes fluctuations of the shape of that interface grow in time, instead of decay.

One of the most well-known and widely studied interfacial instabilities is the so-called Saffmann-Taylor instability (or the viscous fingering instability), which occurs when a droplet of a fluid of low viscosity is injected into a highly-viscous fluid, located in a narrow gap between two plates. An instability is formed at the interface of the injected droplet, which,

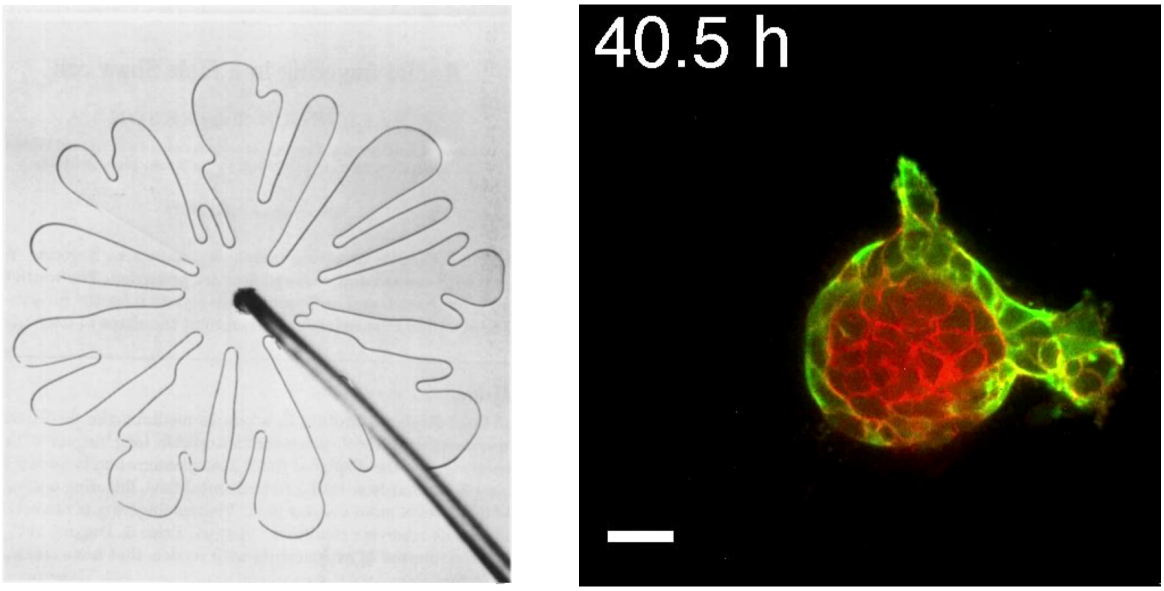

(a) Fingers on the interface between air (in the middle of the picture) and glycerine. Air is injected via the tube. Reprinted from [60]

(b) Fingers at the edge of a mouse breast carcinoma (red and green area), growing in a collagen matrix. Scale bar represents $20\mu m$. Reprinted from [63].

Fig. 1.6 Examples of fingering phenomena in physics (left) and biology (right)

as a result, does not grow uniformly. Instead, the growth gets concentrated in fingers at the edge of the droplet [60] (see Fig. (1.6a)).

We now know that certain biological growth processes are governed by physical interfacial instabilities. For example, formation of loops in a growing gut stems from a mismatch between the growth rate of the gut tube itself and other tissues it is attached to [61]. It has also been argued that the emergence of an undulated boundary of solid tumours, such as glioblastoma (a deadly brain tumour), may result from a mismatch between the growth rate of an outer, living and proliferating rim, and the lack of growth within the dead core [62].

As mentioned before, multi-cellular modes of cancer metastasis and wound healing in epithelial tissues involve the formation of fingers at the boundary of the tissue, resembling slightly the ones seen in a viscous fingering instability (see Fig. (1.6b). We also know that both of these biological processes are strongly dependent on mechanical properties of the tumour and its surroundings, in particular on the emergence of activity in the tissue involved. Therefore, we can plausibly speculate that cancer metastasis and wound healing might be initiated with an interfacial instability, like the other growth processes we just described, and that active forces should play an important role in it.

Investigating such possible instabilities requires constructing biologically and physically justified, simplified theoretical models of physics of biological systems, which enable capturing key elements of a system's dynamics. In the next Chapter, we briefly discuss the existing physical models of tissues, their accomplishments and shortcomings, and introduce our own model, which we then apply to the problem at hand.

Before we do so, we must however stress that results reported in this chapter so far require complex experimental methods. Correctly understanding the results these methods produce, their capabilities and limitations is key to identifying the role modelling efforts can play and the extent to which the outcomes of modelling can be tested experimentally.

1.5 Experimental methods

Most of the experimental techniques used for studying biological motions are based, one way or another, on microscopy. Both wound healing and cancer invasion has been experimentally studied *in vitro* (meaning in cell colonies in the lab), while the latter phenomenon has been also studied *in vivo* (in actual, living organisms). We now take a brief tour over the methods used, starting with those used for observing cancer metastasis *in vivo*.

1.5.1 Traditional diagnostic techniques

Many traditional, well-established techniques have been long used to study the structure of internal human and animal tissue, including sizes and shapes of tumours. These techniques include magnetic resonance imaging, ultrasound imaging, radio tracing and computer tomography. While diagnostically invaluable and irreplaceable so far, these older techniques are only sufficient for studying very large populations of cells and cannot go below large-scale tissue level.

1.5.2 *In vivo* microscopy techniques

Recent advances in techniques of *in vivo* tissue visualization have provided detailed pictures of metastasis, such as those of a metastasizing mouse breast cancer in Fig. (1.7). They are supplemented by in vitro studies of tumors in artificial cell cultures.

In vivo techniques involve microscopy-based studies of tissue in living animals, so arguably provide the most trustworthy insights. Results, however, are still not as abundant as for the case of *in vitro* techniques. We must also remember that the *in vivo* systems these

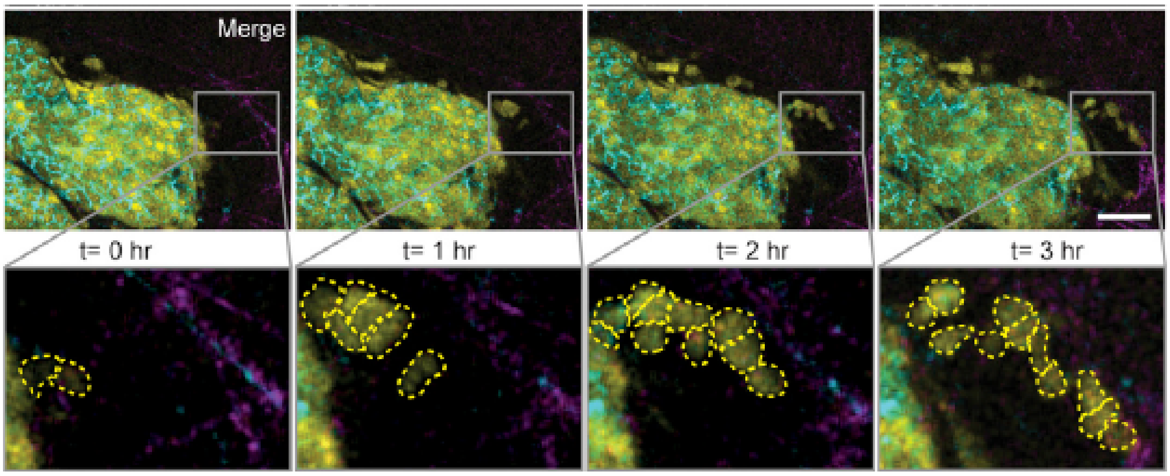

Fig. 1.7 Collective cancer invasion in live mice as observed by intravital, multiphoton microscopy techniques. Lower row shows a close up on a growing metastasising finger, with individual cells surrounded by dashed lines. Reprinted from [27].

techniques study are also not wholly natural: the cancer cells are surgically implanted into living animals, instead of growing there naturally, and have to be previously artificially cultured first [35, 64–67]. They are also cultured from a relatively small group of cell lines, whose representativeness for all cancers in nature can be contested. Arguably, this means that even these *in vivo* studies in fact model cancer, instead of studying "the real thing"[1]. Nevertheless, doubtless they are the closest we have to the "real thing" that can be studied under a microscope.

Fortunately, in the last years, intravital microscopy (IVM) techniques have enabled the study of small, dynamical populations of cells, including small primary tumours and secondary micrometastases (parts of the tumour which have metastized to new organs, in the embryonic phase) [64–66]. IVM encapsulates a very wide and rapidly growing spectrum of techniques [69]. Most of them are based on fluorescent microscopy [69].

IVM of tumours located very shallow within the body (primarily skin cancers, such as melanomas [35]) is achieved using confocal microscopy realized with a microscope placed outside of the animal's body [69, 35]. Confocal microscopy is a subcategory of fluorescent microscopy and uses a pinhole to highly focus excitory light on a small part of the tissue and a second pinhole to eliminate all out-of-focus light while collecting images. This method is sometimes aided in live animals by observing a part of their skin using a dorsal skinfold

---

[1] as Dr Pierre Recho once pointed out to me. I believe this is a good counterargument to any biologist who might question the usefulness of physics-based modelling of biological systems

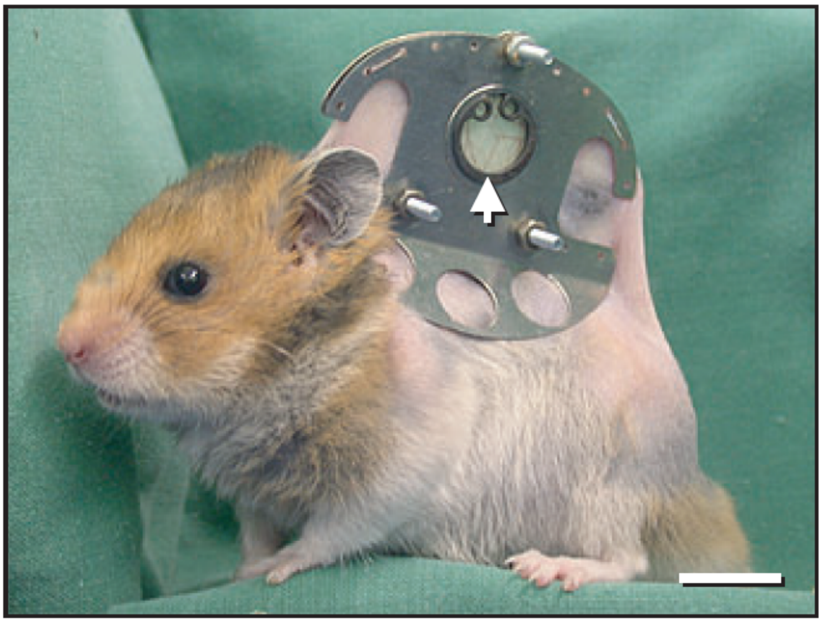

Fig. 1.8 Dorsal skinfold chamber attached to a Syrian golden hamster. The arrow points towards the imaging window, where actual microscopy takes place. In this case, it is used for visualising blood microcirculation. Scale bar represents 1.4 mm. Reprinted from [68].

chamber [35] (see Fig. 1.8)- a large frame, encapsulating a part of the animal's skin, which is firmly attached to its body and enables microscopy of the skin and underlying tissues via a glass window [70]. For example, these methods were used to obtain very detailed pictures of metastasis of melanoma [35].

To increase the depth of imaging, multiphoton microscopy is used [69]; it is based on using photons, whose energy is below the tissue's absorption spectrum (therefore, they can travel to deeper tissues). They are subsequently absorbed in pairs or larger groups in selected locations, where photon bundles coincide [35]. So-called second and third harmonic generations are most frequently used multiphoton microscopy techniques. They are based respectively on simultaneous absorption of 2 or 3 photons and emission of a single photon with an energy equal to the sum of energies of absorbed photons [69, 35]. Multiphoton microscopy has produced, among other results, detailed *in vivo* images of metastasis from a human breast cancer [71].

If the tumour is located deeper within the body, the site is sometimes surgically exposed, while the animal is subjected to anesthesia [72]. However, this method is highly invasive and can lead to the death of the animal.

A different, revolutionary group of techniques used is based on so-called imaging windows, especially abdominal imaging windows. They are millimeter-sized fluorescence-based devices for microscopy [73, 66, 67, 64, 65], which can be surgically implanted deep within the body of an animal [66, 67, 64, 65]. They are used to observe metastatic processes in internal organs, such as mouse spleen, intestine, kidney, liver [64] and connective tissue [37] and have provided detailed pictures of both initial [37] and later [64] stages of metastatic invasion. The imaging window can stay tightly fixed and collect images at a selected point in the animal's body for several weeks [64].

Another, less often practiced technique for obtaining in vivo images of metastasis, is freezing a tissue and performing microscopy on multiple cross-sections of the frozen tissue one-by-one to obtain a 3-dimensional picture [65].

1.5.3 *In vitro* techniques

In vitro techniques are based on studying cell cultures living in laboratory conditions. The conditions the cells live in are therefore less natural than *in vivo*. However, *in vitro* data on cancer metastasis and related phenomena is more abundant than *in vivo* data. *In vitro* techniques also enable measurement of properties not measurable *in vivo*, such as forces exerted by the cells [52, 53]. For studying metastasis, the most popular choice of cells to culture includes mouse mammary cells (MMC) [74]. Cultures (typically of 2 dim or 3 dim spheroidal shape [74]) are implanted into and permitted to grow in assays. A substrate capable of supporting their life has to be provided; for studies of metastasis, it is typically collagen [74] to mimic the structure and composition of natural ECM [74] (though other primary assay components, such as matrigel [63], have been used as well).

A great variety of microscopy techniques is used to observe behaviour of laboratory cell cultures. Classical bright-field microscopy, which obtains contrast in images directly from differences in light absorption by various elements of the sample, remains a relevant and efficient tool in the field, for example, being used for visualising channel-guided migration of epithelial colonies [15]. Phase-contrast microscopy, which creates images by translating phase shifts of light passing through a specimen into brightness variations, is a frequent choice [59, 58, 19, 34]. To name one example, it was used to observe migration of canine kidney cells [59]. Fluorescence imaging techniques are widely used in studying both developmental and oncological processes in cell cultures [74, 15, 58, 18], for example, to monitor mouse mammary tumour cells [74]. Fluorescence microscopy also enables particle image velocimetry (PIV- reconstructing flow profiles by following densely seeded tracer particles) for quantifying cell motility [59, 18]. A novel technique for tracking metastasizing tumours, enabling second-to-second tracking and subcellular accuracy, is based on so-called time-correlated single photon counting (TCSPC) from periodically excited tissue [74]. In this technique, one collects photons emitted by a tissue excited fluorescently. The tissue is excited using infrared photons. Therefore, a virtually simultaneous absorption of 2 photons in a single quantum event is necessary to enable excitation. The rate of excitation and emission is therefore sufficiently low to enable single photon counting. This technique was used, among other phenomena, to study mouse mammary tumour cell cultures [74].

Time-lapse microscopy is a popular technique for producing movies of all types of collective cell motion[15, 59, 58]. It is based on aquiring photographs of a system in regular time intervals via brightfield, phase-contrast or fluorescent microscopy, and replaying them at an accelerated rate to obtain a movie of the process involved. The movie whose single frame is presented in Fig. (1.6b) was also obtained using this method.

The so-called traction microscopy techniques have been proposed at the turn of this century to enable measuring forces exerted by cells. They are based on measuring the displacements of beads embedded in a substrate as it interacts with the cells, and reconstructing mathematically traction, based on the displacement field [75, 76]. Originally, they have been used to measure tractions exerted by individual fibroblasts [75]. They have since undergone significant refinements to improve accuracy, account for finite substrate thickness and other difficulties, and to be applicable to moving cell sheets [77, 78, 52]. It cannot be stressed enough that they constitute a major breakthrough: the experimental methods described previously (especially PIV) can tell us a lot about *kinematics* of cell motion; measuring forces, however, is what enables us to make the jump to try to understand the *dynamical laws* that govern it.

1.6 Goals of part I of this thesis

We have thus completed our brief review of selected experimental literature relevant to the topic of coordinated motions of entire tissues in general, and to fingering patterns observed at the edges of tissues, especially cancer, in particular.

We can now again outline our goal, which is contributing to understanding the role of active forces in the formation of fingers at the edges of active, motile and growing cancers, as seen in Figs. 1.5 and 1.6b. To this end we will design a minimal model of dynamics of the interface of such a tissue and investigate what is the effect of activity on the stability of the interface within the model. This part of the thesis is organized as follows.

Chapter 2 provides an overview of the state of the art of physics-based modelling of tumours and wound healing assays. We discuss the accomplishments of existing models, but clarify why none of them was quite suitable to the task at hand, necessitating a construction of our new model.

The model itself is presented in chapter 3. The assumptions, governing equations, estimations of parameters used and comparison with other models is presented in this chapter. Additional information and discussion is presented in the Appendices.

Chapter 4 applies our model to a growing, circular, active droplet, representing a tumour. Within this simplified system we use our model to analytically demonstrate and explain the role of activity in fingering at the edge of such a droplet. Appendices show applications of our model to several other simple systems.

In Chapter 5, we conclude this part of the thesis with a discussion summing up our results, discussing how their relation to actual biological phenomena could be tested, and outlining directions for future study.

Chapter 2

State of the art

Based on experimental literature reviewed in the previous section, we now have good motivation to try to understand the mechanical basis of fingering at the edges of tumours. This understanding in the practical sense must mean reproducing this key phenomenon within a simplified physical picture, which in turn requires postulating and justifying simplified effective physical laws which govern the system, and seeing what consequences they imply.

Many computational and analytical models were developed and used to model tissue dynamics. Only some of them directly study the problems we aim to tackle, but all provide a context for our model. This chapter gives a quick tour of them, with a special emphasis on those that account for front instabilities and fingering or activity.

We first review discrete models, which treat each cell explicitly. We then turn to methods closer to our own approach: continuum theories of tissue dynamics. We put special emphasis on continuum theories of tissue dynamics which treat tissues as active fluids, since these theories are closest to our strategy. We conclude with spelling out more detail on the gap that we intend to close.

2.1 Discrete computational models

The models in this group account for individual cells explicitly. Among them are the so-called self-propelled particle (SPP) models, vertex models, the Cellular Potts Model (CPM), and confluent ellipse-based models. Let us examine them one by one.

Self-propelled particle (SPP) models (see Fig. (2.1)) represent each cell as a point or a sphere (a "particle"). Mutual interactions between cells and other forces are introduced as

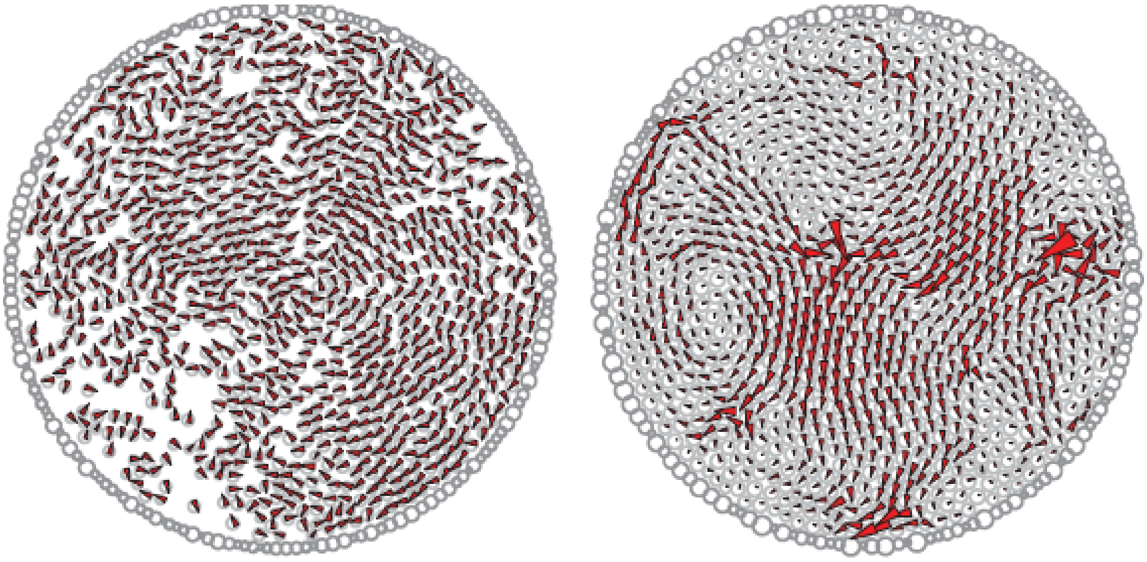

Fig. 2.1 An illustration of a self-propelled particle (SPP) model at two different particle densities. Particles (circles with gray boundaries with overwritten red arrows, representing their velocities) are allowed to move freely on the inside of a ring of soft spheres "glued" together (the circles without arrows). Reprinted from [79].

acting on these points (they can be functions of cell velocity, mutual distance and other observables) [17, 79, 80]. The dynamical laws in the system are also defined for these points. The "particles" usually also have a defined finite radius length, which is a basis for defining repulsion based on excluded volume interactions [79, 17]. Apart from tissues, these models have also been widely used for modelling various other active and passive systems. This includes bird flocks (indeed, the entire class of so called Vicsek-like flocking models- in which agents adjust their speed to that of their neighbors- is of this type [17]), colloids [79], etc.

Activity in these models is usually accounted for by postulating that particles follow persistent Brownian motion [80]. The Brownian movements occur along a preferred, gradually changing direction (hence *self-propelled particles*). The dynamics can be simulated essentially by Brownian Dynamics [17, 79].

These and similar models (see [81]) have been reported to reproduce patterns of collective motion encountered in epithelial layers, including fingering [80, 81]. Interestingly, these phenomena can occur within such models under various principles. Collective motion itself has occurred in them as a result of particles adjusting their speed to that of their neighbors [80] or as a result of coupling of the direction of activity with the direction of velocity [81]. Fingering was reported in [80] in the presence of additional curvature-dependent active forces at the boundary. Interestingly, these models also feature jamming in high density [79].

The downside of these models is that, since cells are represented in them as point particles, they cannot implement confluence, an observed feature of many tissues. Implementing cell-cell contact lines, adhesive interactions and shape fluctuations is impossible for the same reason, as well as accounting for an energetically preferred perimeter and surface area of the cell. These shortcomings explain the popularity of confluent models, to be discussed next.

2.1.1 Confluent models

Confluent models are based on partitioning the entire space between cells. This enables simulating those aforementioned cell properties the SPP models cannot implement. Dynamics can then be assigned based on an energy function related to cell perimeter, cell surface area and other properties [82].

The Cellular Potts Model (CPM) is one of the most popular confluent models [82–85]. In it, the space is discretized into lattice sites much smaller than the cells, and each of the sites is assigned to one of the cells (see Fig. (2.2)). A total energy function is assigned, depending on each cell's area, perimeter, and position of the cell centroid (on which body forces, such as the active motile force, act). The dynamics is obtained indirectly, instead of being assigned by explicit equations of motion. This is done by Monte Carlo sampling of the lattice sites distribution [82]. A lattice site is transferred to another cell if the total energy is minimized by that move. Notably, activity has been included in this model [82, 83]. It has been used to simulate spreading of tissue monolayers [83] and cancer metastasis and has captured the enhancing effect of the tumour's heterogeneity on metastatic dissemination [82].

Vertex models are based on tessellating the space between polygons [86, 87]. Dynamics (usually Brownian) is explicitly centered on and defined for the polygon vertexes, and not for cell centers, like in the SPP models. The forces on the vertices can be defined explicitly. They can also be obtained by defining an energy function based on vertex locations. The derivatives of that energy function over possible vertex positions provide forces on the vertices [88], from which cell motion naturally follows. Arguably, therefore, vertex models have dynamics and motion defined in a more natural way than the CPM, which requires Monte Carlo sampling of possible motions to implement dynamics. However, neighbour changes between cells do

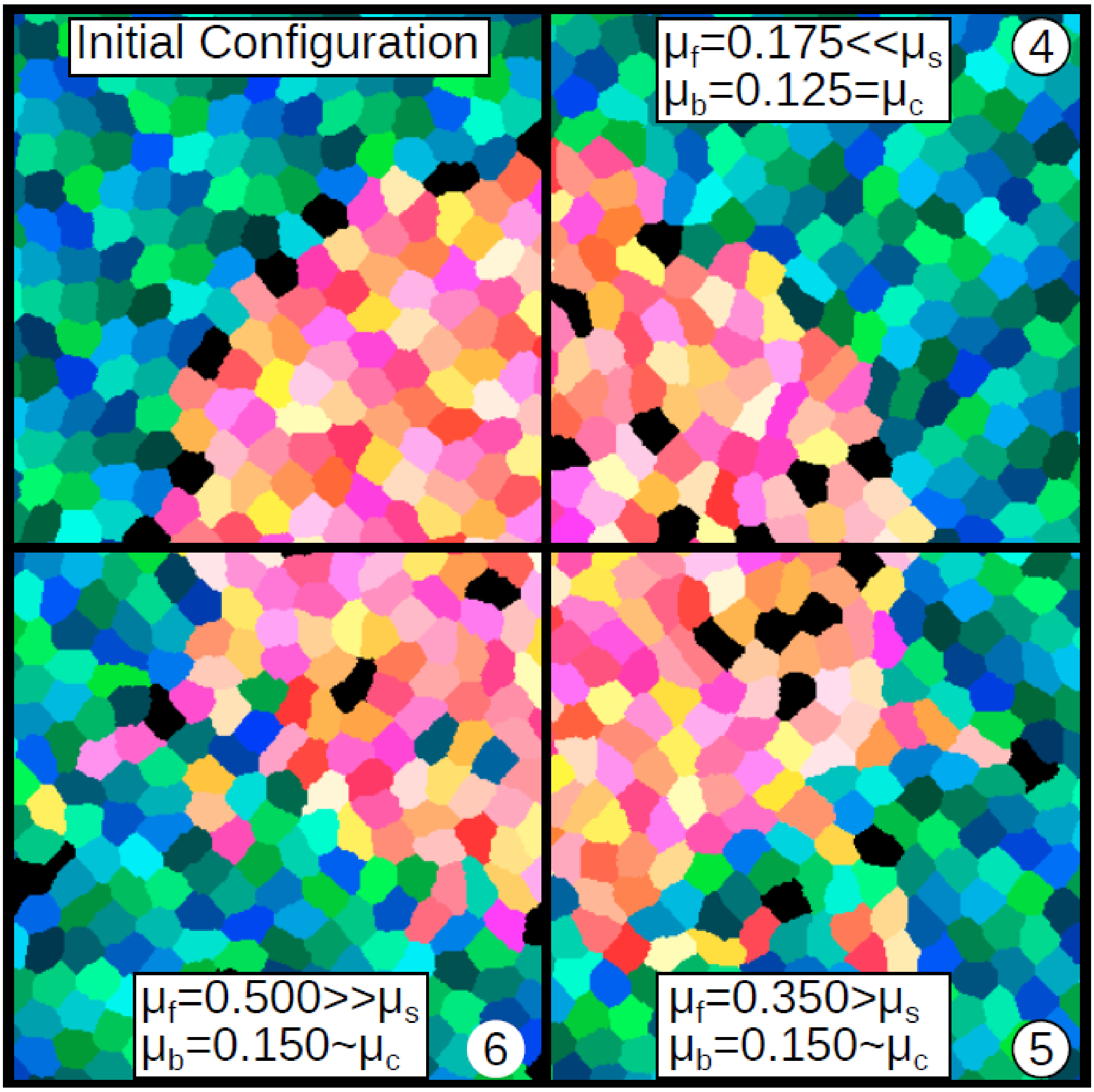

Fig. 2.2 Application of the CPM to simulate cancer cell invasion from a heterogenous tumour (warm-coloured and black cells) into a neighbouring tissue (blue and green cells). Each uni-colored domain is a single cell, made of multiple CPM lattice sites. The upper left quadrant represents the initial configuration, while the remaining quadrants show the result of 4500 Monte Carlo steps for various values of model parameters. The tumour cells are self-propelled, exerting an active "motile" force on a substrate with magnitude μ_b for bulk tumour cells (warm-colored) and μ_f for leader cells. μ_s is a critical magnitude of the force necessary for a cell to migrate between non-motile neighbors, while μ_c is a lower critical value necessary to induce collective motion in a homogenous population of motile cells. Reprinted from [82].

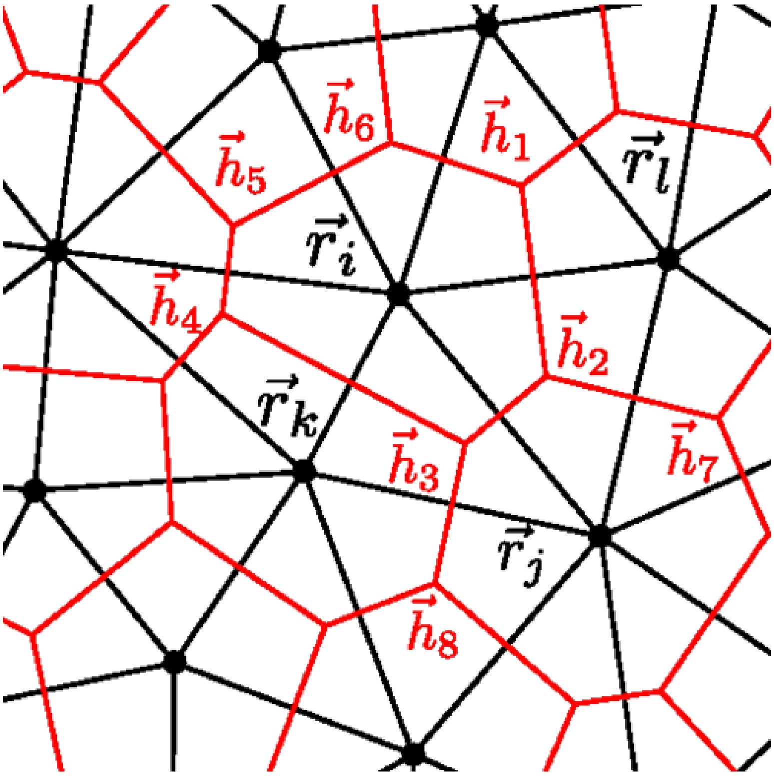

Fig. 2.3 Example of constructing a confluent model: illustration of a Voronoi tesselation algorithm. A set of points $\mathbf{r}_i$ (black dots, interpreted as cell centers in the Self-Propelled Voronoi model [87]) is selected. Each element in space is apportioned to the nearest point in the set, forming cells (separated by red boundaries). Reprinted from [87].

not occur naturally within vertex models. An explicit, somewhat artificial algorithm needs to be implemented to enable a switching of neighbors [88].

Hybrid models

Several hybrid models, being a mix between SPP and vertex models, have been developed to benefit from advantages of both approaches.

One of them, the so-called Self-Propelled Voronoi model defines the cells by the points constituting their centers, like SPP models, and proscribes dynamics at these points. However, it implements confluence of cells by attributing each point in space to the nearest cell center. A partition of space according to this algorithm is called Voronoi tessallation (see Fig. (2.3)). This in particular sets the area and perimeter of every cell, which later serve to define the cell's energy (the cell has a lowest-energy, unstretched state). The energy function then determines a part of the force on the cell, in addition to persistent Brownian terms [87]. This model has its advantages compared to traditional vertex models. For example, it does not require *ad hoc* algorithms for neighbour switching. Like all the aforementioned models, the Self-Propelled Voronoi model can also account for activity. A jamming phase transition in active matter was observed in this model [87]. Within a certain parameter range the model displays glass-like behavior [87], which was measured experimentally in collective cell migration [3].

A hybrid model reported in [88], aims to reproduce natural cell shapes more faithfully by defining an "abdomen" of the cell as an ellipsoid, but also carrying out a partition of the remaining space between cells [88]. It has been used to simulate developmental processes, such as the growth of the forebrain neural plate in zebrafish [88].

2.1.2 Partially continuous models

Some computational models use a hybrid, discrete-continuum approach or take the continuum limit of discrete models. In some of these, cells are not represented explicitly, with their density (possibly averaged over short time or space scales [10]) treated as a hydrodynamic variable [10, 89]. One of such models, equivalent to a continuous limit of CPM, has been used to simulate spongy bone formation [89]. A hybrid discrete-continuum model was used to simulate the growth of epithelial colonies, implementing explicitly cell division [10].

2.1.3 Conclusion

Simulations based on discrete and semi-discrete models previously described have reproduced collective motion in tissues. They have also shown which types of interactions and properties of tissues enable the occurrence of such phenomena. Notably, they have successfully explored the significance of activity.

They do, however, have their problems. A separate simulation has to be carried out for each combination of parameters to explore the effect on tissue behaviour. Predicting *a priori* the model behaviour for a given parameter set is usually impossible, and only *a posteriori* interpretations of obtained results are available. Also, discrete models are defined in terms of interactions of individual cells and are not always easily related to bulk mechanical properties of the tissue. For these reasons it is also beneficial to construct a continuum theory whenever plausible. We next turn to instances when this has been done.

2.2 Continuum theories of tissue dynamics

Several theoretical frameworks have been recently developed to understand collective cell motion within a continuum mechanics paradigm. They have several advantages over computational models: dynamics is given by continuous differential equations, which can be exactly solved analytically or numerically; by finding these solutions, one can immediately uncover the system's behaviour across a large parameter range, without running separate simulations for each value of each parameter. They provide access to the rich toolbox of methods of traditional continuum mechanics. They also elucidate a direct link between dynamics and values of bulk mechanical parameters, such as viscosity, which are not easy to include or even computationally define in discrete models. While they are often quite crude approximations, they are very useful for understanding the systems at hand.

Of course, the continuum dynamics theories do have their disadvantages, too. Analytic solutions are often available only for very simplified dynamical laws and boundary conditions with many symmetries. The scale at which the continuum approximation becomes roughly correct is also disputable-one can be confident only for systems very large compared to the characteristic size of a single cell. However, they are very useful for understanding the systems at hand. Below we shall discuss some of the developed frameworks, their accomplishments and relevance to our task at hand.

2.2.1 Total deformation tensor framework

The fundamental dilemma when modelling tissues with continuum mechanics is the following: elastic or viscous? In general, tissues are known to display very complex viscoelastic behaviour [90], meaning they feature aspects of both viscous and elastic mechanics. Solving the dynamics of tissue growth, however, would be impractical when accounting for it fully. In practice, most models start out with the assumption that at least locally and instantaneously, a given tissue is fundamentally viscous or elastic. We first discuss two frameworks working under the latter assumption.

Assuming the tissue is fundamentally elastic leads to a serious problem almost instantaneously: what is the reference no-strain, no-stress state, a key concept in the theory of elasticity, if the tissue is growing continuously? One framework to deal with this problem was developed in [91]. A total deformation of a growing tissue is decomposed into two parts: one comes from transforming the zero-stress state due to growth, and the other from accompanying deformations of the tissue, necessary to maintain its material consistency. It is this second part that causes internal mechanical stress within the tissue, which in turn influences growth. This way, a closed system of equations for the tissue's growth is obtained. The relationship between internal stresses and deformations has been usually postulated in the literature as elastic [92, 93].

This framework has been especially useful in studying growth of tissues in the presence of frustrations. Among other systems, it was used to model growth of thin elastic tissues [94, 95], concluding, among other things, that anisotropic growth in itself is sufficient to spontaneously destabilize a spherical shell [95]. Anisotropic growth was also argued, using this approach, to lead to residual stresses in the growth of cancer, approximated as a spheroid [93]. The approach is also the basis for Ciarletta's model, explaining buckling of the edge of a large and growing brain tumour [62] due to internal frustrations, because of a difference in the rate of growths of the entire tumour and of a sub-domain of dead cells within it [62]. Growth of a swelling gel clamped on one side to a stiff substrate was also investigated in this model, with possible applications to biological systems which feature growth in a restricted geometry. This research found wavy instabilities, controlled by the rate of growth [96].

Recent work has expanded this framework to replace a growth tensor with a generalized active tensor, which accounts not only for growth-related deformations, but also for deformations caused by active forces generated by cells. Such active forces might include, for example, active contractility. This extension of the model was used to study the morphogenesis of a fruit fly's wing and to argue that inhomogenous stress might "convey locally the global information of organ size" (paraphrasing [97]). Another strategy of including active cell forces in this framework was proposed in [98], where a model of a growing, solid epithelial tissue was constructed. In this work, the active forces exerted by cells are not included in the active tensor, but are introduced as non-equilibrium additional terms to equations of motion. This work predicted fingering at the edge of an epithelial tissue [98].

In general, if the tissue is solid-like, this framework seems quite successful in describing instabilities, including fingering, resulting from growth and internal frustrations. However, we later postulate in this thesis a slightly different mechanism behind fingering, which requires a slightly different approach. Before we move on to it, we review another theoretical framework for elastic tissues.

2.2.2 Incremental elasticity model

J. Prost and collaborators have proposed a different formulation of mechanics of locally solid, growing tissues. It is based on explicitly incorporating forces on existing tissue resulting from cell apoptosis and division into the total expression for stress [99]. The reasoning behind the model argues that while cell division and apoptosis are impossible to reconcile with the existence of a unique no-stress, no-strain state of the body, which defines traditional elastic materials, the rate of change of strain between subsequent moments in time is still well defined. The total stress tensor[1] σ_{ij} can be decomposed into a part related to cell flow (the rate-of-strain tensor: $v_{ij} = \frac{1}{2}\left(\partial_i v_j + \partial_j v_i\right)$, where v_i is the cell velocity) and a part directly caused by cell division and apoptosis σ^s_{ij}, and the equation for its rate of change can be written as:

$$\frac{D}{Dt}\sigma_{ij} = C_{ijlm}v_{lm} + \frac{D}{Dt}\sigma^s_{ij}. \tag{2.1}$$

Here $\frac{D}{Dt}\sigma_{ij} = \partial_t\sigma_{ij} + v_l\partial_l\sigma_{ij} + \omega_{il}\sigma_{lj} + \sigma_{il}$ is a convected corotational time derivative, $\omega_{ij} = \frac{1}{2}\left(\partial_i v_j - \partial_j v_i\right)$ is the flow vorticity, and C_{ijlm} is the tensor of elastic constants. The authors postulate the form of the cell division and apoptosis contribution to stress σ^s_{ij} [99, 100]. This, when combined with postulating an inverse relationship between the net rate of cell division and stress within the tissue, allows for deriving constitutive equations.

The conclusion is that the tissue effectively behaves as a viscoelastic Maxwell material. It is elastic on short time scales, viscous on long time scales, compared to cell division and death rates [99, 100]. Intuitively, this can be understood as follows: while the tissue immediately deforms as a linear solid, on the long run a portion of the tissue under increased stress responds with an increased cell death rate, so that area retracts like in a liquid.

The authors also coined the term "homeostatic pressure", which is the pressure in which equal numbers of cells undergo division and apoptosis, so that the tissue remains in a steady state. If the external pressure on the tissue is different, processes of global growth or death are predicted [99].

This model has been used to study the growth of tissue spheroids and cancer [100, 101] and fluctuations on an interface of a tissue in equilibrium [102].

---

[1] Note in the following the subscript $_i$ represents a component in the x_i direction and we use Einstein's convention for the summation of indices.

2.2.3 Modelling active tissues as fluids

The previously described models of tissue dynamics assumed that, in the absence of growth, tissues behave like an elastic solid [91, 99]. Many theories of tissue continuum mechanics, however, assume viscous constitutive equations. There are, depending on the system, additional force terms such as: drag against a substrate, active force on a substrate, active production of momentum due to cell-cell interactions. Many of these models account in one way or another for activity.

One of such models studied analytically the epithelium as an overdamped Stokes fluid with cell division and growth in contact with an elastic and viscous stroma [56]. It predicted an emergence of fingers at the boundary of the epithelium, resulting from the interplay between spatially non-uniform cell division/death rates and shear [56]. Several other models treat the tumour as a porous environment. Therefore, the cells in such models are assumed to obey Darcy's Law (meaning that velocity is proportional to the pressure gradient) [103–106].

The Toner-Tu is an important model, incorporating activity. It was developed originally for motion of flocks [107–109] and adapted to deal with active fluids, including bacterial suspensions [48, 110, 16] and tissues [16, 111]. The dynamical equations of Toner-Tu theory in most general terms have the following form [108] (note the time-dependent fields: $\mathbf{v}$ is velocity, ρ is density, p is pressure):

$$\begin{aligned}\rho(\partial_t\mathbf{v}+\lambda_1(\mathbf{v}\cdot\nabla)\mathbf{v}+\lambda_2(\nabla\cdot\mathbf{v})\mathbf{v}+\lambda_3\nabla(|\mathbf{v}|^2))\\=\alpha_T\mathbf{v}-\beta_T|\mathbf{v}|^2\mathbf{v}+\eta_1\nabla^2\mathbf{v}+\eta_2\nabla(\nabla\cdot\mathbf{v})+\eta_3(\mathbf{v}\cdot\nabla)^2\mathbf{v}-\nabla p.\end{aligned}\tag{2.2}$$

The origin of the terms is as follows: the ones on the left hand side represent the equivalent of the convective derivative in the Navier-Stokes equation (lack of momentum conservation and Galilean invariance means these terms can have the general form as presented, as no symmetry restricts it). The extra terms, absent in the Navier-Stokes system, correspond to possible non-traditional interactions within the fluid. The first two terms on the right-hand side correspond to the fact that there exists a preferred non-zero magnitude of velocity $|\mathbf{v}_s|$ of the system ($|\mathbf{v}_s|=\sqrt{\frac{\alpha_T}{\beta_T}}$- note α_T and β_T have to be positive) and an effective quartic Landau-type velocity potential, which selects it $V(\mathbf{v})=-\alpha_T|\mathbf{v}|^2+\beta_T|\mathbf{v}|^4$. This was motivated originally by the fact that birds in flocks seem to have such a preferred velocity magnitude [107]. In tissues, these terms have a very natural physical interpretation: the α_T term corresponds to the active force exerted by the cells on the substrate and β_T corresponds to the drag from the substrate [111, 16]. δp is a classical Navier-Stokes pressure term. The four gradient terms on the right-hand side correspond to momentum dissipation within the tissue; note the first of these corresponds to the classical Navier-Stokes viscosity.

In practice, usually when Toner-Tu equations are adapted for specific active systems, some of the terms are omitted (by setting their respective constants to 0). Only the terms which are motivated by the physics of the problem are retained. Less frequently, additional ingredients are added to account for additional, relevant hydrodynamical fields (such as nematic polarisation) [16, 110].

The model has been used for various active fluids, including, in several examples, in modelling of cell motion. We are aware of its application to wound healing models by Zimmermann, Basan, and Levine [111] and by Nesbitt, Pruessner, and Lee [112]. However, the analyses in the two latter works are limited to a non-dividing, rectangular tissue, either in a static state, or somehow pushed on one side by a rigid barrier. The first of these papers argues that fingering is possible in such a system, but the second refutes that claim. Others use the model to explain formation of small vortices after cell division [16].

The Toner-Tu model implicitly assumes a coupling of the direction of the active force to the direction of the fluid's velocity. Other models have abandoned that restriction by treating the direction of the active force as an independent internal variable (named "polarity"), coupled to stress, velocity or chemical fields [113, 53, 114]. One of these models has been used to reproduce the stress profile in an expanding epithelial monolayer [53] and, more recently, to argue that fingering at the edge of a spreading epithelia might stem from acceleration of that edge, due to a velocity gradient caused by the active tractions [114].

2.3 Conclusion

As we have seen, an impressive body of work on continuum mechanics of tissues has been accumulated in the previous years. Some of the models used have investigated interfacial fingering, some have investigated activity and some have investigated growth. However, bringing the three phenomena together has proved much more challenging.

Apart from a small handful of works [111, 112, 114], continuum theories have also not studied analytically the effect of activity in the bulk of the tissue on fingering instabilities of its edge–only effects of activity at the edge itself have been tackled [115, 116]. This is because interfacial instabilities are very difficult to study analytically unless both the hydrodynamics of the participating fluids and the shape of the boundary itself are very simple. Previous formulations of activity have often rendered hydrodynamics of the active fluids too complicated for realistic set-ups of tissue growth.

In the next chapters, we contribute to filling this gap. We construct a continuum mechanical model of an active and growing tissue, motivated by experimental observations. It proves to be analytically solvable for a set-up mimicking a growing tumour and enables a successful analytic investigation of its interfacial instabilities.

Chapter 3

Presentation of a new model

3.1 Proposed governing equations

In this chapter, we present our model of an active and growing tissue, which was first published in [1]. In the model, the evolution of the pressure $p(\mathbf{r},t)$ and velocity $\mathbf{v}(\mathbf{r},t)$ fields at a position $\mathbf{r}$ and time t are governed by the following force balance and mass conservation equations,

$$\nabla p = -\beta \mathbf{v} + \alpha \frac{\mathbf{v}}{|\mathbf{v}|}, \tag{3.1a}$$

$$\nabla \cdot \mathbf{v} = k, \tag{3.1b}$$

respectively. Here ∇ is the nabla operator, α and β are positive parameters, specifying the strength of the interaction between the tissue and a substrate. α describes the magnitude of the active traction, and β the magnitude of the effective passive friction (the latter being proportional to the tissue viscosity). In Eq. (3.1b), k is the net rate of growth (we are interested in regimes in which it is positive), representing a growing tumour mass of an incompressible tissue, undergoing cell division (or individual cell growth). The α-term in Eq. (3.1a) accounts for the active force of the tissue against the substrate and is discussed in detail in Sec. 3.2. The evaluation of the various parameters is examined in Sec. 3.3.

3.2 Justification of governing equations

Eq. (3.1a) assumes an *inertialess* dynamics for the deformations of a tissue layer. This is appropriate for our purposes, since a broad scientific consensus considers biological tissues a strongly overdamped, inertialess environment. For example, [16] estimates the Reynolds number in endothelial monolayers as circa 10^{-9}.

Ignoring the α-term, Eq. (3.1a) reduces to Darcy's law ($\nabla p = -\beta \mathbf{v}$), originally used to describe pressure-driven viscous flows in porous materials and Hele-Shaw apparatus [117]).

Darcy's law also assumes a *viscous* dynamics. This point is worthy of some discussion, since, as discussed previously, both elastic and viscous rheologies have been assumed in continuum theories of tissue dynamics.

The mechanical properties of live tissues at short time scales, up to the order of minutes, are generally dominated by an elastic constitutive behaviour. At longer timescales, however, a viscous description is better suited [53]. The crossover between the two regimes is likely related to the turnover rates of inter-cellular adherens junctions [118, 88]; the presence of cell division and apoptosis can also lead to fluid behaviour [99]. Also, when becoming malignant, epithelial tissues become fluidized by a reduction in the number of adherens junctions, and a concomitant increase in the magnitude of active traction. This well-known “melting” process is a feature of the previously described “epithelial to mesenchymal transition” [119, 120, 4]. Since here we model the behaviour of the tissue at timescales on which it experiences substantial growth (that is, on the order of several hours at least [63]), the viscous constitutive behaviour implied by Darcy's law is justified. Many existing continuum models of epithelial tissues also assume viscous rheology [105, 56, 53, 121].

We also implicitly assume that the effects of friction against a substrate are much stronger than those of viscous shear within the plane of the layer. This is in general true if the Darcy law term $-\beta \mathbf{v}$ is much larger than the classical dissipative term of the Navier-Stokes equations of the form $\mu \nabla^2 \mathbf{v}$, where μ is the viscosity of the tissue. Via dimensional analysis of the inequality $|\beta \mathbf{v}| >> |\mu \nabla^2 \mathbf{v}|$, this is true on lengthscales λ satisfying $\lambda >> \sqrt{\frac{\mu}{\beta}}$. We argue in subsection 3.3 that $10^{15} - 10^{16}\,\mathrm{Pa\,s\,m^{-2}}$ is a plausible estimation for β. Viscosity μ of epithelial tissues has been estimated based on measurements involving cell aggregate compression in [122] as circa $10^6\,\mathrm{Pa\,s}$ and in [123] as circa $4.4 * 10^5\,\mathrm{Pa\,s}$. A wider range of estimates for effective viscosity of a spreading monolayer was obtained from fitting a dynamical model to data in [53] as $10^5 - 10^7\,\mathrm{Pa\,s}$, depending on the exact cell type. In [88] a cell-cell sliding viscosity of $10^5\,\mathrm{Pa\,s}$ was assumed as a basis for computational modelling, based on a review of available literature. It is worth noting that microscopic viscosity within tumour cells *in vivo* and *in vitro* was recently measured as much lower, on the order of

$1\,\mathrm{Pa\,s}$ [124]; however we presume the former, higher ranges of values are more realistic as estimates of bulk, whole tissue viscosity, which is presumably largely generated by friction between cells. Based on these ranges of numbers, we can estimate $\lambda \sim 10^{-6} - 10^{-4}\,\mathrm{m}$, with the lower part of the range more typical. Based on comparing this to the typical diameter of a single epithelial cell being over $10^{-5}\,\mathrm{m}$, we conclude that our assumption is likely plausible in many circumstances. It is worth noting, however, that, depending on the specific modelling study, either of the dissipative terms or both have been accounted for [114]. Darcy's law, in particular has been already widely employed to model the passive behaviour of tissues [104–106, 103].

As in classical Hele-Shaw systems for which Darcy's law has been formulated first [117], its application is especially well justified in quasi-2D systems, in which the surface area directly susceptible to external friction is very large compared to the volume of the system. Our adoption of Darcy's law goes in par with our adoption of the model to quasi two-dimensional systems. Using two-dimensional models is experimentally justified by the large prevalence of *in vitro* two-dimensional tissue culture monolayers, but also because many *in vivo* soft tissues, including epithelium in which carcinomas develop, tend to spontaneously form quasi-2D monolayers [52, 13, 5]. For these reasons, as well as for easier solution and interpretation of results, two-dimensional descriptions are usually employed in models of tissue mechanics [82, 56, 96]. In consistency with this discussion, in subsequent sections we apply our model to 2D systems.

The second term on the right-hand side of Eq. (3.1a) accounts for cells actively propelling themselves by exerting traction against the substrate. It is subsequently referred to as the active term, and α specifies its strength.

We assume here that the direction of the net local active force acting on the tissue layer from the substrate is aligned with the direction of the local flow velocity. This assumption was made in previous studies modelling active tissues [81, 83]. It is a consequence of cells attempting to maintain their direction of motility, as illustrated in Fig. (3.1a), and also manifested by the persistent Brownian motion of individual cells in vitro [126]. On a subcellular level, it likely results from the friction destabilising lamellipodia (protrusions at the leading edge of the cell, used to propel it forward) [127, 128] that are not aligned with the cell's velocity [81].

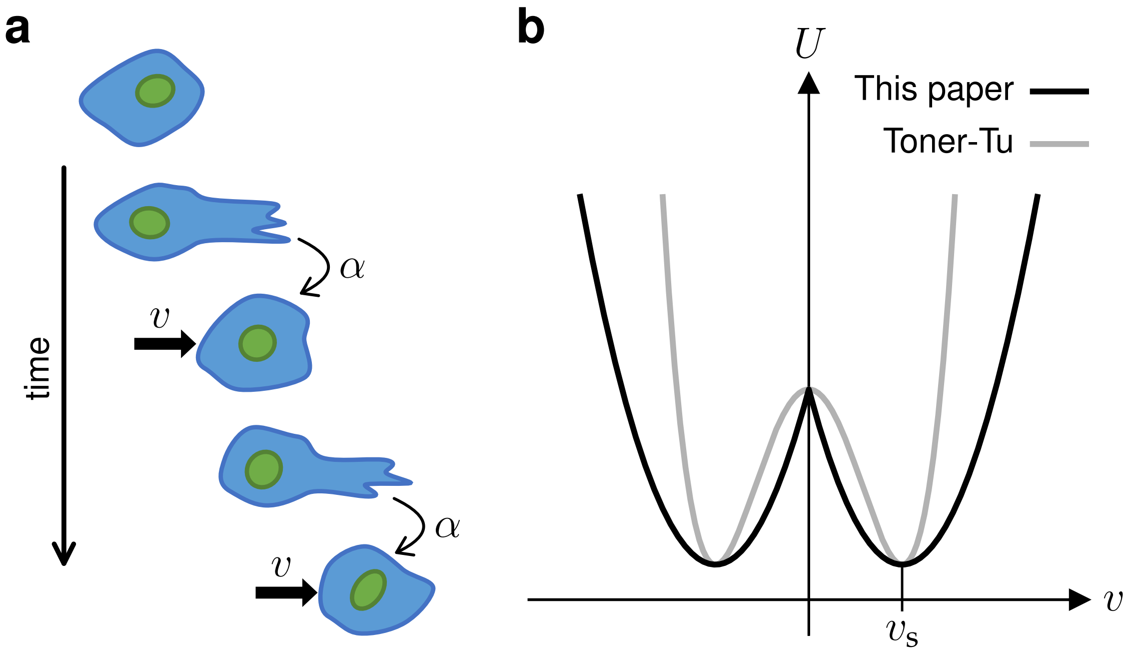

Fig. 3.1 Assumptions of the active traction model. Panel (a) schematically illustrates how the active traction of a mesenchymal or epithelial tumour cell acts in the direction of its migration velocity; filopodia and/or lamellipodia are protruding at the leading edge of the cell, which translocates in the same direction. Panel (b) compares (in 1D) the effective "velocity potential" [125], $U(\mathbf{v})$ defined by the volumic traction force being $\mathbf{F} = -\partial_{\mathbf{v}} U$, of our model with the Toner-Tu model; both potentials select an intrinsic velocity v_s (see text), but our model introduces a discontinuity at $\mathbf{v} = \mathbf{0}$ which has no effect on our results.

Eq. (3.1a) also assumes that the active traction does not depend on the magnitude of the velocity. This assumption has been made in several numerical models of motile cells [81, 17, 87], and enables a distinct analysis of the role played by activity.

3.3 Estimation of parameters

Based on *in vivo* microscopy observations [63] of the time necessary for doubling a carcinoma's size, which is on the order of a few hours, we estimate that the growth rate k is about $10^{-4}\,\mathrm{s}^{-1}$.

The passive friction β can be estimated based on *in vitro* force measurements of epithelial tissues against substrates [129, 52, 53] (admittedly, inference about *in vivo* systems from these *in vitro* experiments is arguable). Following Pompe *et al.* [129], we assume that friction with the substrate is primarily the consequence of cell-substrate ligands, numbering

Parameter	Symbol	Unit	Value
Growth rate	k	s^{-1}	10^{-4}
Passive friction	β	$\mathrm{Pa\,s\,m}^{-2}$	$10^{15}-10^{16}$
Active traction	α	$\mathrm{Pa\,m}^{-1}$	$0-10^{10}$
Surface tension	γ	$\mathrm{Pa\,m}$	$10^{-3}-10^{-2}$

Table 3.1 Estimates of the physical parameters

$200-300$ per cell, each of which exerts a force of about $10^{-12}\,\mathrm{N}$. We thus estimate the total friction force per cellular volume to be about $10^{6}\,\mathrm{N\,m}^{-3}$ for a $10^{-5}\,\mathrm{m}$ cell size. From *in vivo* microscopy of micrometastasis growth [63], the typical velocity v of the cells falls within $10^{-10}-10^{-9}\,\mathrm{m\,s}^{-1}$. Hence, dividing the volumic friction force by this velocity provides an estimate $\beta \sim 10^{15}-10^{16}\,\mathrm{Pa\,s\,m}^{-2}$.

There is no lower limit on α, as epithelial cells may not exert any or exert very weak active force against the substrate. The upper limit can be estimated on the basis of force tracking microscopy applied to spreading epithelial monolayers *in vitro* [52, 53]. It is observed that traction forces are actively exerted through the monolayers and peak at their edges, giving rise to a gradient of the stress tensor's diagonal terms, which is up to $10^{7}\,\mathrm{Pa\,m}^{-1}$ in the study by Trepat *et al.* [52], and $10^{8}\,\mathrm{Pa\,m}^{-1}$ in the work of Blanch-Mercader *et al.* [53]. Balancing α with this typical stress gradient, one can place an upper estimate on α at $\sim 10^{8}\,\mathrm{Pa\,m}^{-1}$. Concurring, the traction exerted by single fibroblasts has been reported as up to $10^{-7}-10^{-5}\,\mathrm{N}$ per cell [130], which would correspond to $\alpha \sim 10^{8}-10^{10}\,\mathrm{Pa\,m}^{-1}$ when dividing by the cell's volume.

The effective surface tension of the tissue γ also plays a role in our further considerations, as we proceed to discussing concrete systems of fluids described by Eq. (3.1a). Its magnitude depends on the strength of intercellular adhesion and behaviour of cortical actin networks [131, 132]. The surface tension was evaluated indirectly in Foty *et al.* [133] by measuring the energetic penalty of compression of embryonic multicellular spheroids, revealing values on the order of $3-9\,\mathrm{mPa\,m}$. We thus presume that $\gamma \sim 10^{-3}-10^{-2}\,\mathrm{Pa\,m}$ is a realistic range for our system.

A summary of the estimates for the physical parameters is presented in Tab. 3.1.

As is shown later on specific examples of systems, one of the important practical advantages of Eqs. (3.1) is that interfacial fingering in this model can be solved analytically in several realistic, finite systems of growing tissues. This is because, under some natural assumptions, the equations for spatial dependency of pressure perturbations reduce to analytically solvable second-order differential equations (see Chapter 4 and Appendix B). This is unlike any other model of an active, viscous, growing tissue we encountered and considered.

The coupling between direction of activity and velocity our model assumes, as mentioned previously, is consistent with experimental data [81, 134, 135], though not true in all systems [58].

The classic, previously discussed theory derived by Toner and Tu [107, 108] and often used to model active fluids [112, 111, 136], uses only slightly different terms for the volumetric active and passive force against the substrate $\mathbf{F}_{\mathrm{T}}(\mathbf{v}) = \alpha_{\mathrm{T}}\mathbf{v} - \beta_{\mathrm{T}}|\mathbf{v}|^2\mathbf{v}$ (with α_{T} and β_{T} positive parameters). In comparison, our model, Eq. (3.1a), gives this force the expression $\mathbf{F}(\mathbf{v}) = \alpha\mathbf{v}/|\mathbf{v}| - \beta\mathbf{v}$. The two models are similar, therefore, further discussing their relative similarities and differences, strengths and weaknesses is necessary.

In both cases, the fluid has a "preferred" spontaneous magnitude of velocity; $|\mathbf{v}_{\mathrm{S}}| = \alpha/\beta$ in our model and $|\mathbf{v}_{\mathrm{S,T}}| = (\alpha_{\mathrm{T}}/\beta_{\mathrm{T}})^{1/2}$ in the Toner-Tu model, which it would select when moving in unbounded space without being driven by an external pressure gradient or growth. For magnitudes of velocity lower than $|\mathbf{v}_{\mathrm{S}}|$, the fluid would be driven to move faster by the α-term, while above it, it would be slowed down by the friction (the β-term). This fluid's constitutive behaviour may be described in terms of an effective "velocity potential" [125], shown in Fig. 3.1b. This potential takes the form $U(\mathbf{v}) = \alpha|\mathbf{v}| - \frac{\beta}{2}|\mathbf{v}|^{\mathbf{2}}$ for our model and $U_{\mathrm{T}}(\mathbf{v}) = \frac{\alpha_{\mathrm{T}}}{2}|\mathbf{v}|^{\mathbf{2}} - \frac{\beta_{\mathrm{T}}}{4}|\mathbf{v}|^4$ for the Toner-Tu model. In both systems, the effective potentials can be approximated as quadratic wells around the spontaneous velocity, where, up to a constant, $U(\mathbf{v}) \approx \alpha_{\mathrm{T}}(\mathbf{v} - \sqrt{\frac{\alpha_{\mathrm{T}}}{\beta_{\mathrm{T}}}})^{\mathbf{2}}$ and $U_{\mathrm{T}}(\mathbf{v}) \approx \frac{\beta}{2}(\mathbf{v} - \frac{\alpha}{\beta})^{\mathbf{2}}$ respectively. Although our model has a discontinuity in the direction of $\mathbf{F}(\mathbf{v})$ at $\mathbf{v} = 0$ which does not exist in $\mathbf{F}_{\mathrm{T}}(\mathbf{v})$, this singularity does not affect our subsequent results, since we always investigate the linear stability of a growing, and, consequently, flowing tissue, with $|\mathbf{v}| > 0$. In general, we would expect many similarities between the behaviour of analogous system set-ups governed by one and the other model. This is demonstrated in Appendix A, in which fingering at the interface between an active and a passive fluid in a rectangular channel with constant flow velocity is investigated in the minimal version of the Toner-Tu model and in our model; the behaviour of the two fluids is qualitatively similar. Specifically, the dependence of the linear growth rate $\sigma(q)$ on the wavevector q of interfacial perturbations of the two fluids is almost identical, with the perturbations in the Toner-Tu fluid slightly more stable at shortest wavelengths.

The Toner-Tu model, however, assumes that the friction force grows as $|\mathbf{v}|^3$ and that the active force varies linearly with $|\mathbf{v}|$. While it is a very good effective model for active systems [125, 81], both assumptions are, strictly speaking, unrealistic when describing biological tissues. Our model, on the other hand, retains the, physically correct, approximation of friction linearly growing with $|\mathbf{v}|$. The physical interpretation of β as the friction coefficient of Darcy's Law is retained, as well as the interpretation of α as the magnitude of the active force of the tissue against the substrate (per unit volume). Our approach also enables a direct comparison with classical results for viscous fingering [60], readily obtained from our model by taking the limit $\alpha \to 0$. The difference in the scaling between the friction term and velocity would probably lead to larger differences in predictions between the two models for system set-ups in which velocity is not uniform through space, like the one formulated in Sec. 4.1.

Practical advantages of our model in comparison with the Toner-Tu model are important. To the best of our knowledge, fingering interfacial instabilities in the Toner-Tu model can only be solved analytically in systems without growth and, therefore, uniform velocity (like the ones described by [111, 112]). Appendix C shows that it is impossible in systems with growth. In contrast, our model enables solving interfacial fingering instabilities analytically in many realistic and physically plausible systems, incorporating growth, as discussed in chapter 4 and appendix B. We now proceed to discussing one of such systems, motivated by fingering observed at the edges of growing carcinomas.

Chapter 4

A uniform, circular droplet

4.1 Motivation and system set-up

4.1.1 Governing equations

After presenting and discussing the model's equations, we are now prepared to apply it a system representing a growing, active epithelial/mesenchymal tumour. Results and almost all of the discussions presented in this chapter and some related appendices were separately published by us in [1]. We choose to model the tumour as an initially circular, 2D droplet of a growing, active fluid described by Eqs. (3.1), with an unperturbed, time-dependent radius $r_0(t)$ (see Fig. 4.1). The surrounding healthy tissue is modelled as a passive, non-dividing fluid, whose pressure $p'(\mathbf{r},t)$ and velocity $\mathbf{v}'(\mathbf{r},t)$ fields follow:

$$\nabla p' = -\beta' \mathbf{v}' \,, \tag{4.1a}$$

$$\nabla \cdot \mathbf{v}' = 0 \,, \tag{4.1b}$$

where β' is the friction parameter (analogous to β in the active fluid). In writing Eq. (4.1b), we effectively assume that growth in the passive fluid can be neglected on the timescale of metastasis initiation.

We assume that the activity α and the growth rate k are constant (independent of $\mathbf{r}$ and t) through the active fluid. Constant magnitude of the active force has been assumed in models of active matter before [137, 138]. While not correct in all situations [53, 57], it is a convenient assumption to evaluate the influence of the magnitude of activity in fingering. Similarly, we assume that β and β' are uniform within their respective regions. Extensions to non-uniform and time-dependent behaviours of these parameters are readily possible, and we investigate a case of evolving growth rate in Sec. 4.3.1 (see also appendix E.2).

The choice of this geometrical set-up is also worthy of explanation, since flat interfaces have also been used in modelling of tissues [139]. We believe, however, that our choice is relatively well justified experimentally, since virtually circular tumour spheroids have been produced in *in vitro* experimental models [63] and also observed *in vivo* [62]. At the same time, symmetries of the circular system facilitate analytical modelling. For this reason, circular tumour interfaces have been frequently assumed in mechanical models of tumours [62, 100]. Such a shape of interface also has the additional advantage of naturally introducing a characteristic length corresponding to the system size (via the radius of the circle), so it enables an analysis of the dependence of fingering behaviour on the system size. A flat interface introduces no such natural characteristic lengthscale.

Analytically investigating fingering within our model is also possible in several other biologically and physically relevant set-ups. This includes a circular droplet with the fluid injected at its middle, as was the case for the traditional set-up of radial viscous fingering [60] and in a rectangular geometry, with and without growth. Solutions for these systems are described in Appendices A and B.

We study the present system in polar coordinates $\mathbf{r} = (\rho, \theta)$ and write vector fields' components in this system with appropriate subscripts, such as $\mathbf{v} = (v_\rho, v_\theta)$. The perturbed interface between the active and passive fluids, described by the line $r(t,\theta)$, must satisfy two boundary conditions. First, the continuity of the radial components of velocities is expressed as:

$$v_\rho|_{\rho=r} = v'_\rho|_{\rho=r} = \partial_t r \,. \tag{4.2}$$

Second, the pressure difference across the interface separating the two fluids must equal the Laplace pressure. In polar coordinates this condition has the form:

$$p|_{\rho=r} - p'|_{\rho=r} = -\gamma \frac{r^2 + 2(\partial_\theta r)^2 - r\partial^2_{\theta\theta} r}{[r^2 + (\partial_\theta r)^2]^{3/2}} \,, \tag{4.3}$$

where γ is the surface tension, and the fraction is the expression of the local interfacial curvature in polar coordinates [140].

Note that, unlike some previous studies dealing with fingering phenomena in tissues [116, 80], our boundary condition does not account for a possible bending modulus of the interface. This is in line with our strategy of modeling the behaviour of the system using liquid phenomena. In addition, the interface between malignant and neighbouring cells may not always constitute a single physical membrane on spatial scales larger than a single cell diameter, so there would be no energetic cost of bending it on such length scales, while we

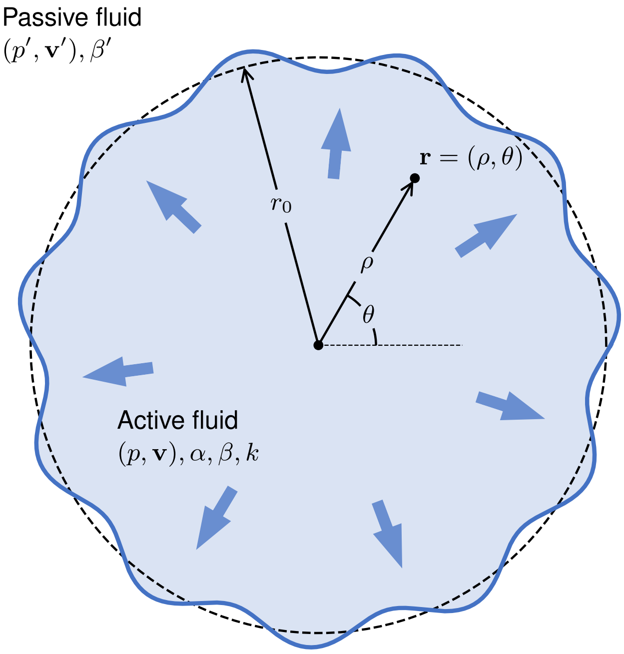

Fig. 4.1 Model system of a tumour growing in an external tissue: a 2D circular droplet with radius r_0 and made of an active fluid described by Eqs. (3.1), is expanding in a passive fluid modelled by Eqs. (4.1). The interface undergoes periodic perturbations whose linear stability is investigated in Sec. (4.2).

expect the surface tension would always be present, due to differential adhesion between malignant and healthy cell types [141].

4.1.2 Dimensionless system of variables

Unless explicitly stated otherwise, we study this system using the dimensionless variables defined as follows. Distances are rescaled by the characteristic length $\ell = \left(\frac{2\gamma}{\beta k}\right)^{1/3}$, which can be interpreted as a capillary length at which growth balances interfacial tension (on the order of $10\,\mu\mathrm{m}$, based on the estimates of Tab. 3.1). Times are rescaled by k^{-1}, and we further define $\phi = \beta'/\beta$ the relative viscosity of the displaced tissue compared to the active growing droplet. We introduce a reference activity $\alpha^* = \beta \ell k \sim 10^7\,\mathrm{Pa\,m^{-1}}$ to make the active traction α dimensionless, $\alpha/\alpha^* \to \alpha$. Pressures and velocities are made dimensionless by $p^* \equiv \beta \ell^2 k \sim 10^2\,\mathrm{Pa}$ and $v^* \equiv \ell k \sim 10^{-9}\,\mathrm{m\,s^{-1}}$, respectively. We use the same letters for the dimensionless versions of the variables as for their dimensional counterparts.

Governing Eqs. (3.1), (4.1) in this system of variables have the form:

$$\nabla p = -\mathbf{v} + \alpha \frac{\mathbf{v}}{|\mathbf{v}|}\,, \tag{4.4a}$$

$$\nabla \cdot \mathbf{v} = 1\,, \tag{4.4b}$$

for the active fluid and:

$$\nabla p' = -\phi \mathbf{v}'\,, \tag{4.5a}$$

$$\nabla \cdot \mathbf{v}' = 0\,, \tag{4.5b}$$

for the passive fluid.

The velocity interfacial boundary condition as given by Eq. (4.2) has the same form in this system of variables, but the pressure boundary condition as given by Eq. (4.2) is now written as:

$$p|_{\rho=r} - p'|_{\rho=r} = -\frac{1}{2}\frac{r^2 + 2(\partial_\theta r)^2 - r\partial^2_{\theta\theta} r}{[r^2 + (\partial_\theta r)^2]^{3/2}}\,, \tag{4.6}$$

that is, effectively the dimensionless surface tension $\gamma = \frac{1}{2}$ in this system of variables.

4.1.3 Unperturbed solution

The droplet of the active fluid grows due to a positive k, as required by Eq. (3.1b), and the passive fluid is displaced by it. As long as the interface between the two tissues remains circular (with the unperturbed radius r_0), hydrodynamic fields in both regions remain symmetric under rotations. The solutions to them are given by:

$$\mathbf{v}_0 = \left(\frac{\rho}{2}, 0\right), \qquad p_0 = \alpha(\rho - r_0) - \frac{1}{4}(\rho^2 - r_0^2) + p|_{\rho=r_0}\,, \tag{4.7a}$$

$$\mathbf{v}'_0 = \left(\frac{r_0^2}{2\rho}, 0\right), \qquad p'_0 = -\frac{\phi r_0^2}{2}\ln\left(\frac{\rho}{r_0}\right) - \frac{1}{2r_0} + p|_{\rho=r_0}\,, \tag{4.7b}$$

as obtained by solving Eqs. (4.4-4.6) and Eq. (4.2).

4.2 Linear stability analysis

We investigate under which conditions the active, circular droplet of radius r_0 would start to form finger-like protrusions at its edge, while undergoing uniform growth. To do this, we perform a linear stability analysis around the symmetric solution given by Eqs. (4.7), by

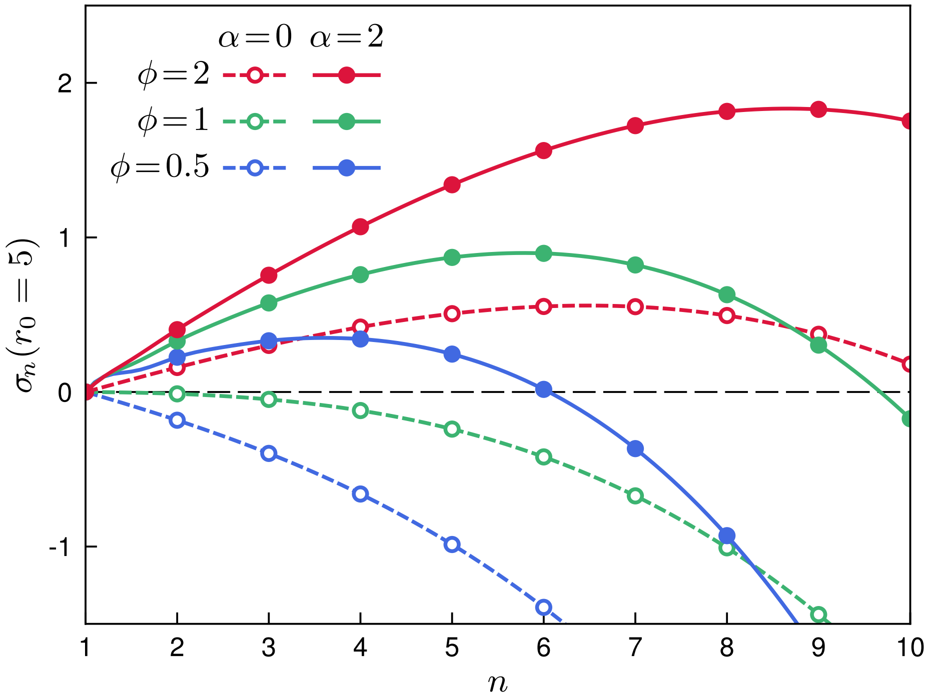

Fig. 4.2 Growth rate $\sigma_n(r_0=5)$ of periodic interfacial perturbations as a function of the number of fingers n, for a droplet of size $r_0=5$, made of a passive ($\alpha=0$; dashed lines) or an active ($\alpha=2$; solid lines) fluid, with varying ϕ.

investigating infinitesimal interfacial perturbations of the form $r=r_0+\delta r$, with

$$\delta r \propto f_n(t)e^{in\theta} \tag{4.8}$$

for an integer n corresponding to the mode of the periodic perturbations, and where $f_n(t)$ is a function describing its time evolution (with $\lim_{t\to 0} f_n(t)=1$ for all n). An analogous ansatz of periodicity in θ is made for the perturbations of hydrodynamic fields in both fluids, $(\delta p, \delta p', \delta \mathbf{v}, \delta \mathbf{v}') \propto f_n(t)e^{in\theta}$, around the solution given by Eqs. (4.7). Note that our stability analysis concerns small perturbations around solutions that are themselves time-dependent. Applying the evolution equations as in Eqs. (4.4- 4.5), and the boundary conditions as given by Eqs. (4.2, 4.6) to these perturbed fields provides an expression for the n-mode's rate of growth defined by

$$\sigma_n(r_0) = \lim_{t\to 0} \frac{\partial_t f_n(t)}{f_n(t)}\,. \tag{4.9}$$

Positive values of $\sigma_n(r_0)$ correspond to unstable, growing modes n, which may become the basis for the formation of fingers.

The strategy of our demonstration mirrors that given by Paterson [60]. We substitute the linearized perturbations to the hydrodynamic fields in both fluids, $(\delta p, \delta p', \delta \mathbf{v}, \delta \mathbf{v}')$, into Eqs. (4.4- 4.6) and Eq. (4.2) and obtain, to linear order:

$$\partial_\rho \delta p = -\delta v_\rho \,, \tag{4.10a}$$

$$v_\rho \partial_\theta \delta p = \alpha \rho \delta v_\theta - \rho v_\rho \delta v_\theta \,, \tag{4.10b}$$

$$\partial_\rho (\rho \delta v_\rho) = -\partial_\theta \delta v_\theta \,, \tag{4.10c}$$

in the active fluid, and

$$\partial_\rho \delta p' = -\phi \delta v'_\rho \,, \tag{4.11a}$$

$$\partial_\theta \delta p = -\rho \phi \delta v'_\theta \,, \tag{4.11b}$$

$$\partial_\rho (\rho \delta v'_\rho) = -\partial_\theta \delta v'_\theta \,, \tag{4.11c}$$

in the passive fluid. Here v_ρ, v'_ρ are the radial components of $\mathbf{v}_0$, $\mathbf{v}'_0$ respectively.

Introducing the ansatz of periodicity in θ, that is $(\delta p, \delta p', \delta \mathbf{v}, \delta \mathbf{v}') \propto e^{in\theta}$, in Eqs. (4.10-4.11) allows us to calculate the partial derivatives with respect to θ. Combining the resulting equations, and using the expression of $\mathbf{v}_0$ of Eq. (4.7a), leads to second-order differential equations for the pressure perturbations in both fluids:

$$n^2 \delta p = (\rho - 2\alpha) \partial_\rho (\rho \partial_\rho \delta p) \,, \tag{4.12a}$$

$$n^2 \delta p' = \rho \partial_\rho (\rho \partial_\rho \delta p') \,. \tag{4.12b}$$

The fact that these differential equations have analytic solutions is key to the solvability of our model. The equivalents of Eqs. (4.10, 4.12) for a wider group of circular and rectangular systems are presented in Appendix C (Eqs. (C.1-C.3)). We now assume $\alpha < r_0/2$ (see Sec. 4.2.3). Eqs. (4.12) are both solved by linear combinations of 2 functions. One function in each of these combinations has incorrect asymptotic behaviour (diverging, instead of decaying away from the interface) and is removed. The retained functions serve to formulate the allowed forms of pressure perturbations:

$$\delta p = q(t) \left[\sum_{j=0}^{n} \frac{(-1)^j}{n+j} \binom{n+j}{j} \binom{n}{j} \left(\frac{2\alpha}{\rho} \right)^{-j} \right] e^{in\theta} \,, \tag{4.13a}$$

$$\delta p' = q'(t) \left(\frac{\rho}{r_0} \right)^{-n} e^{in\theta} \,, \tag{4.13b}$$

with $\binom{n}{j}$ the binomial coefficient “n choose j”.

The functions $q(t)$ and $q'(t)$ are then obtained by finding δv_ρ (using Eq. (4.13a) in Eq. (4.10a)) and $\delta v'_\rho$ (using Eq. (4.13b) in Eq. (4.11a)), and substituting the resulting expressions into the kinematic boundary conditions, Eq. (4.2). Note that all intermediate steps are presented explicitly in an analogous derivation for a rectangular system in Appendix A. One gets:

$$\delta p = \frac{r_0}{n}\left[\partial_t \delta r - \frac{\delta r}{2}\right]\left[1 + \frac{2\alpha}{r_0} - \Lambda_n\left(\frac{2\alpha}{\rho}\right) - (n-1)\frac{2\alpha}{\rho}\right], \tag{4.14a}$$

$$\delta p' = \frac{\phi r_0}{n}\left[\partial_t \delta r + \frac{\delta r}{2}\right]\left(\frac{\rho}{r_0}\right)^{-n}, \tag{4.14b}$$

where Λ_n is the function defined by Eq. (4.16), and where the θ-dependency $e^{in\theta}$ has been incorporated into δr. Using both expressions in the pressure boundary condition, Eq. (4.3) linearised to first order in δr, and substituting $\delta r \propto f_n(t)e^{in\theta}$ leads to an expression for $\partial_t f_n / f_n$. Upon using the definition of $\sigma_n(r_0)$, Eq. (4.9), we finally obtain the following expression for $\sigma_n(r_0)$:

$$\sigma_n(r_0) = \frac{1}{2}\frac{(\phi-1)(n-1) - n(n^2-1)/r_0^3 + \Lambda_n\left(\frac{2\alpha}{r_0}\right)}{\phi + 1 + \Lambda_n\left(\frac{2\alpha}{r_0}\right) - n\frac{2\alpha}{r_0}}, \tag{4.15}$$

where $\Lambda_n(x)$ is the function

$$\Lambda_n(x) = nx - 1 + n\frac{\sum_{j=0}^{n} \frac{(-1)^j}{n+j}\binom{n+j}{j}\binom{n}{j}x^{-j}}{\sum_{j=0}^{n} j\frac{(-1)^j}{n+j}\binom{n+j}{j}\binom{n}{j}x^{-j}}. \tag{4.16}$$

Eq. (4.15) holds provided $\alpha < r_0/2$ (see Sec. 4.2.3 for a discussion). The first term in the numerator of Eq. (4.15) represents the effects of the viscosity mismatch, the second term embodies the effects of surface tension, while the final term shows the effects of activity.

4.2.1 Comparison to classical viscous fingering

Since $\Lambda_n(0) = 0$ for all n, we obtain the following expression of $\sigma_n(r_0)$ in the passive limit $\alpha \to 0$:

$$\sigma_n(r_0)|_{\alpha=0} = \frac{1}{2}\left[\frac{n(\phi-1)}{\phi+1} - 1 - \frac{n(n^2-1)}{r_0^3(\phi+1)}\right] + \frac{1}{\phi+1}. \tag{4.17}$$

The first term (square brackets) of Eq. (4.17) is equivalent to the landmark result obtained by Paterson [60] for viscous fingering in a radial geometry (Eq. (10) in Ref. 60), upon imposing the injection rate Q in Paterson's formula equal to the total amount of the droplet's growth per unit time in our setting (that is, $Q = \pi r_0^2$ in dimensionless variables). The last term $1/(\phi+1)$, however, distinguishes our result from Paterson's, and stems directly from the fact that, here, the invading fluid also grows within the fingers at the boundary.

The fact that, apart from this term, the dispersion relations for the two passive set-ups converge is worthy of a brief aside discussion, to which this paragraph is devoted, as it provides some insights into how the fingering instability depends on growth, flow profiles and activity. It implies that, for fingering in a passive fluid, it does not matter if the growth is concentrated in the middle due to an injection, or distributed within the bulk of the fluid. The reasons for this are as follows. The dispersion relation Eq. (4.15) is obtained from the interfacial pressure boundary condition in the presence of a perturbation of the boundary, taken to linear order. When $\alpha = 0$, the zero-order pressure close to the interface as given by Eq. (4.7a) and the pressure perturbation as derived from Eqs. (4.10) and given by Eq. (4.14a) is "blind" to the flow profile in the bulk of the droplet. This changes, however, in the presence of activity, as in this case Eq. (4.10b), co-determining the pressure perturbations, is dependent on the velocity profile in the bulk of the fluid. Therefore, in the presence of activity, the growth distribution within the growing droplet would matter for interfacial fingering.

4.2.2 Enhancement of fingering instabilities by activity

Figure 4.2 shows $\sigma_n(r_0)$ vs. n for various values of ϕ and α, and for an unperturbed droplet radius $r_0 = 5$. Only integer values of n (circles in Fig. 4.2) have a physical interpretation. The first mode $n = 1$ corresponds to a translation of the droplet, and since $\Lambda_1(x) = 0$ for all x, $\sigma_1(r_0) = 0$ for all values of r_0, α and ϕ. Higher modes $n \geq 2$ correspond to the formation of n fingers on the interface of the active droplet and, if unstable (that is, if $\sigma_n(r_0) > 0$), could potentially initiate the multicellular protrusions observed in tumours (see Figs. (1.5, 1.6b) or the original article [63]).

In passive fluids, $\phi > 1$ (that is, the invaded fluid being more viscous than the invading one) is a necessary condition for fingering to be initiated, since this type of instability can only grow when the pressure gradient near the interface is lower in the invading, than in the displaced fluid [142]. However, we observe that $\sigma_n(r_0)$ increases with α, so that modes that are stable when $\alpha = 0$ may become unstable in the presence of activity $\alpha > 0$ (compare the dashed and solid blue curves, obtained with $\phi = 0.5$, in Fig. 4.2). Therefore, activity can trigger fingering in systems that are stable otherwise, as well as enhance and/or change the dominant modes in droplets that are already unstable.

Activity lowers the pressure gradient of the invading fluid near the interface, hence promoting instabilities. Using the expression of p_0 and p_0' given in Eqs. (4.7), we find that the condition for fingering, $|\nabla p|_{\rho=r_0} < |\nabla p'|_{\rho=r_0}$, is equivalent to $\phi + \frac{2\alpha}{r_0} > 1$ when the effects of surface tension are negligible.

4.2.3 High-activity regime

As already mentioned, the dimensional $|\mathbf{v}_\mathrm{s}| = \alpha/\beta \sim 10^{-9}\,\mathrm{m\,s^{-1}}$ is a characteristic velocity at which the active fluid would move in an unbounded space, under uniform pressure and without growth. If $|\mathbf{v}_\mathrm{s}|$ exceeds the growth-generated velocity of the interface, the active fluid's motion is frustrated and further instabilities occur across its entire area. We call this regime, for which dimensionless $\alpha > r_0/2$, "high activity". Appendix D formally shows that when dimensional $|\mathbf{v}| < \alpha/\beta \sim 10^{-9}\,\mathrm{m\,s^{-1}}$, the bulk of the fluid is itself unstable. In this case, the derivation of Eq. (4.15), which assumes that perturbations are only arising at the interface and decaying away from it, is not valid. This regime is potentially relevant to the behaviour of real epithelial tissues, in which fingering at the boundaries is accompanied by swirls forming across the entire area of the tissue [143].

Hence, Eq. (4.15) is only valid for the "low activity" regime ($\alpha < r_0/2$). Yet, even in this regime, the active droplet may feature a region of instabilities near its centre $\rho < 2\alpha$, where the velocity magnitude $|\mathbf{v}_0|$ (given by Eq. (4.7a)) is less than $|\mathbf{v}_\mathrm{s}|$. In particular, this situation would have also occurred in the system considered in Fig. 4.2. In practice, a separate simulation-based study would be most appropriate to obtain the velocity field throughout the whole active region, and to understand the behaviour of the active fluid in the high activity regime. In further sections of this thesis, we only examine the system's behaviour in the low activity regime.

4.3 Critical radius for the onset of fingering

For small enough radii, surface tension stabilizes the active droplet, but its strength decreases as that droplet grows. Therefore, there exists a critical radius for the onset of fingering, below which the active droplet grows circular and unperturbed. Since $n = 2$ is always the first mode to become unstable, $r_\mathrm{c}(\alpha, \phi)$ is defined by the conditions $\sigma_2(r_0 = r_\mathrm{c}) = 0$ and $\partial_{r_0}\sigma_2(r_0)|_{r_0=r_\mathrm{c}} > 0$ provides an estimate of that critical radius. Using Eq. (4.15) with $\Lambda_2(x) = x(3x-4)/(2x-3)$, these conditions are equivalent to finding a polynomial root (first condition) within a subdomain (second condition), and have a unique positive solution.

We plot $r_\mathrm{c}(\alpha, \phi)$ vs. α in Fig. 4.3, which shows that increasing activity decreases the minimum radius for fingering. When $\phi < 1$ (purple curve in Fig. 4.3), there exists a minimum

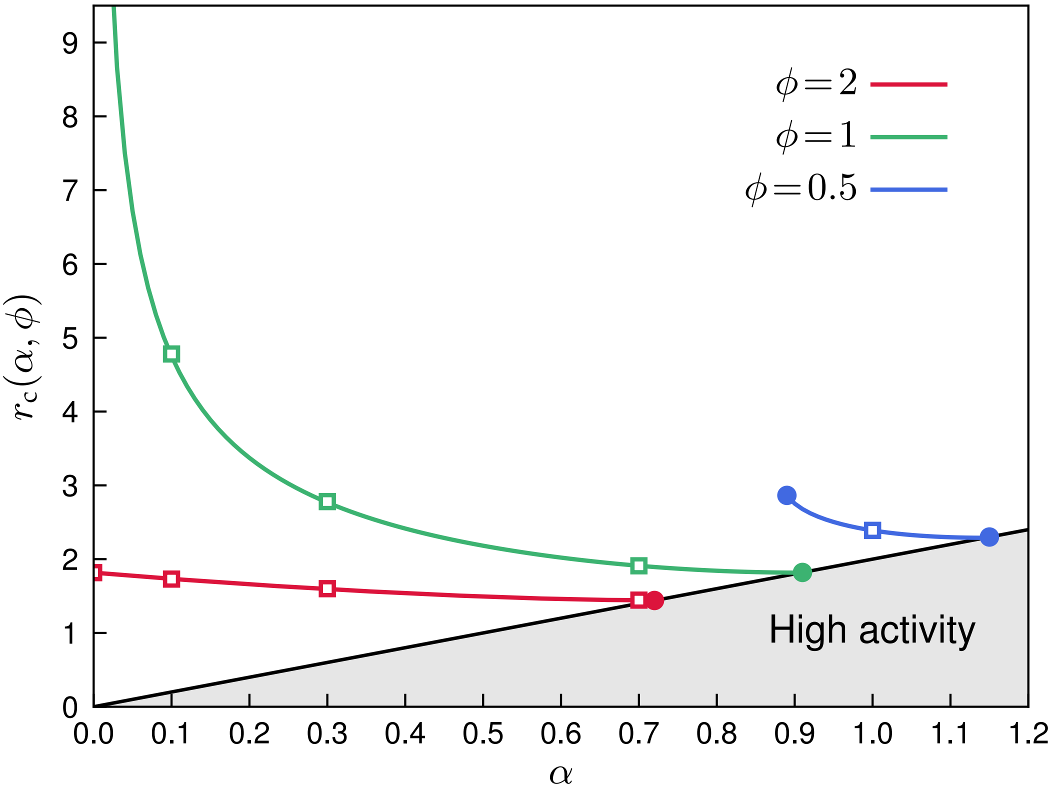

Fig. 4.3 Minimum radius $r_c(\alpha,\phi)$ for the initiation of fingering. The gray area on the graph signifies the high-activity regime, in which the linear stability analysis does not apply (see Sec. 4.2.3). The squares indicate the values of α used in Fig. 4.4 for each viscosity ratio ϕ.

value of α, below which fingering cannot occur, because the higher viscosity of the invading droplet has a stabilising effect. When $\phi = 1$ (green curve in Fig. 4.3), a moderate increase of α may decrease r_c multiple times. The impact of α in fingering is, however, reduced when $\phi > 1$ (the red curve in Fig. 4.3), since in that case the interface would be unstable even without activity.

The range of dimensionless r_c presented in Fig. 4.3 would correspond to a radius of $10 - 100\,\mu\text{m}$; however, it can be much higher for lower values of α. This range of r_c is nevertheless in qualitative agreement with the tumour size at which the onset of fingering occurred in experimentally studied carcinomas [63].

4.3.1 Dominant mode

We now address the question of how many fingers are visible in practice, or, technically speaking, the question of which perturbation mode dominates during growth. Viscous fingering studies suggest the dominant mode is the one satisfying the so-called maximum-amplitude criterion [144]. The criterion is satisfied by the mode n_d experiencing the largest total aggregated growth in amplitude ζ_n over the entire history of the system [144]. Following Ref. 144, we obtain ζ_n by integrating the rate of the perturbation's growth, as predicted by our linear stability analysis, over that history:

$$\zeta_n(r_0) = \exp\left[\int_{R_n}^{r_0} \sigma_n(r)\frac{\mathrm{d}t}{\mathrm{d}r}\mathrm{d}r\right], \tag{4.18}$$

where R_n is the radius at which mode n is first destabilised (i.e., the minimum radius at which $\sigma_n(R_n)$ becomes positive). The dominant mode n_d is then obtained for each r_0 from the conditions,

$$\partial_n \zeta_n(r_0)|_{n=n_\mathrm{d}} = 0\,, \tag{4.19a}$$

$$\partial^2_{nn} \zeta_n(r_0)|_{n=n_\mathrm{d}} < 0\,, \tag{4.19b}$$

used to locate the maximum aggregated growth.

As we shall see, the selection of the dominant mode depends on the particular kinetics of the droplet's growth. The kinetics of tumour growth is known to vary between tumours and their stages of development. Some experimental studies have shown that an initially exponential growth [145] (corresponding to a constant k) subsequently slows down with time (implying a decrease in average k) as the tumour enlarges and its resource supply becomes a limiting factor [146–148]. Other kinetics have been measured for various tumours and

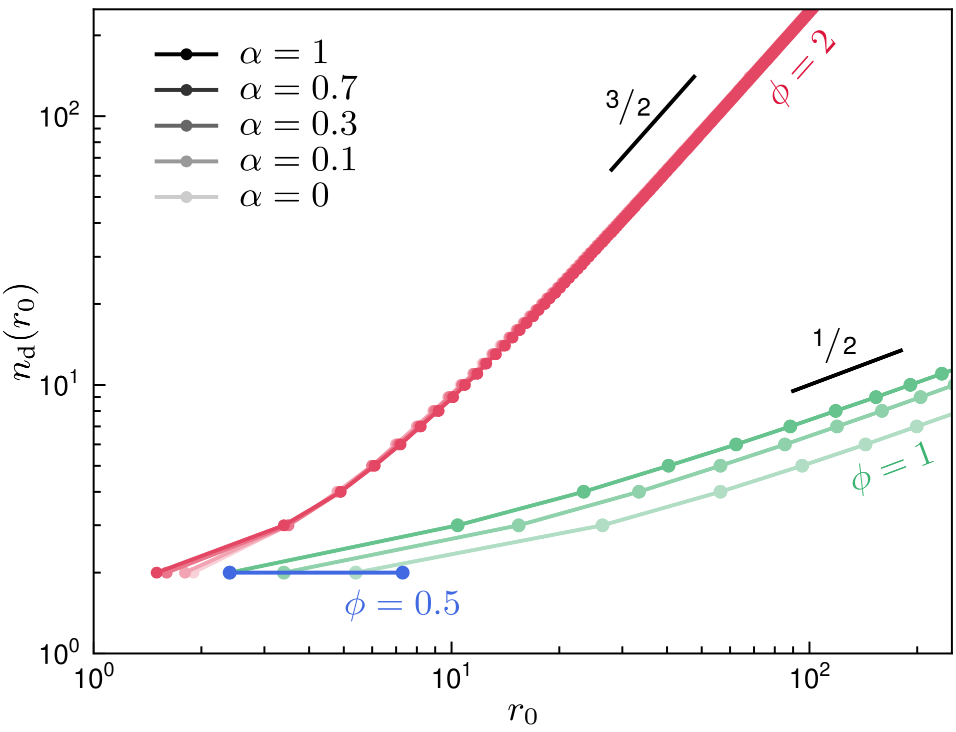

Fig. 4.4 Numerical estimation of the dominant mode $n_\mathrm{d}(r_0)$ observed in an active droplet of radius r_0, undergoing exponential growth, for various values of α and ϕ.

phases of growth, including sigmoidal regimes in which the growth stalls [146–148]. A kinetics where the tumour's radius grows linearly with time also naturally emerges when the tumour proliferates only within an outer rim [148]. Such growth can also effectively occur as a temporary feature in a sigmoidal kinetics.

We thus proceed to discuss in detail the selection of dominant modes in two kinetic models of droplet growth: an exponentially growing droplet, where k is uniform and independent of time and $r_0(t) = r_\mathrm{i} e^{k(t-t_\mathrm{i})/2}$ (from Eq. (3.1b) at the interface, and with dimensional variables; r_i being the initial radius at time t_i); and a droplet with a radius growing linearly with time, $r_0(t) = r_\mathrm{i} + v_i(t - t_\mathrm{i})$, with v_i the constant and uniform velocity of the unperturbed interface. In the latter case, the growth rate k appearing in Eq. (3.1b) evolves with time.

Exponential growth

The integral given in Eq. (4.18) cannot be expressed analytically for all values of ϕ and α, and we plot in Fig. 4.4 the relationship $n_\mathrm{d}(r_0)$ obtained from numerical evaluation. When $\phi > 1$, and for low radii close to the onset of fingering, we observe that the activity has only a moderate influence on the selection of the dominant mode. For later growth, when r_0 becomes large, the viscosity mismatch is the governing cause of fingering and activity plays no role in the selection of the dominant mode. We numerically observe the power-law variations $n_\mathrm{d} \propto r_0^{3/2}$, independent of α. When $\phi = 1$, higher activities promote the selection of higher modes. We obtain numerically, and for large r_0, the scaling $n_\mathrm{d} \propto r_0^{1/2}$, where the $1/2$ power law is independent of α. When $\phi < 1$, certain low-n modes become destabilised, provided sufficient α. However, these perturbations restabilise and decay as r_0 increases further, because the stabilisation from viscosity mismatch dominates as the radius of the droplet grows: active terms of Eq. (4.15) vanish $r_0 \to \infty$, while terms involving ϕ remain constant in this limit.

We recover analytically the observed scalings for large n_d and r_0, and for $\phi \geq 1$. We derive in the appendix E.1 the following results when $r_0 \to \infty$: $n_\mathrm{d} \approx (\phi - 1)^{1/2} \times r_0^{3/2}$ for $\phi > 1$ and $n_\mathrm{d} \approx \left[(\alpha/2)^2 + (\alpha/2)^{1/2}\right]^{1/2} \times r_0^{1/2}$ for $\phi = 1$, which we give below in dimensional variables to highlight the influence of the various physical parameters:

$$n_\mathrm{d} \approx c^{1/2}\left[\frac{k(\beta' - \beta)}{2\gamma}\right]^{1/2} \times r_0^{3/2} \qquad \text{for } \beta' > \beta\,, \tag{4.20a}$$

$$n_\mathrm{d} \approx \left[\frac{2\gamma}{\beta k}\left(\frac{\alpha}{4\gamma}\right)^2 + \left(\frac{\alpha}{4\gamma}\right)^{1/2}\right]^{1/2} \times r_0^{1/2} \qquad \text{for } \beta' = \beta\,, \tag{4.20b}$$

when $r_0 \gg \left(\frac{2\gamma}{\beta k}\right)^{1/3}$, and with $c \approx 0.06$ defined as the smaller of the two solutions to $3c = 3 + \ln c$.

Linear growth

We also investigate pattern selection for a droplet with a radius growing linearly with time. The derivation of $\sigma_n(r_0)$ proceeds along identical lines, although in this case, the integral in Eq. (4.18) can be expressed analytically. Details of this calculation are given in the appendix E.2, and in this case we find that $n_\mathrm{d} \approx c(\alpha + \phi - 1)^{1/2} \times r_0$ is valid for all values of the physical parameters in the low activity regime when $r_0 \to \infty$, and where $c \approx 0.06$ is the constant defined previously. We thus write, in dimensional form,

$$n_\mathrm{d} \approx c\left[\frac{\alpha + v_i(\beta' - \beta)}{\gamma}\right]^{1/2} \times r_0\,, \tag{4.21}$$

when $r_0 \gg \left(\frac{\gamma}{\beta v_i}\right)^{1/2}$ (note that the dimensionless variables are defined differently in the linear growth, as explained in appendix E.2). The difference in the n_d vs. r_0 power-law dependency between Eqs. (4.20) and (4.21) highlights the role of the growth kinetics in the fingering pattern, and is discussed with more details in the following.

Comparison and discussion

We now examine the evolution of the droplet's shape in the two growth kinetics studied above. An initially circular droplet is allowed to evolve, with the n-mode perturbation starting when the radius r_0 reaches R_n, and with an initial amplitude of 0.2 (corresponding to $\sim 2\,\mu\mathrm{m}$). The perturbation is subsequently allowed to grow according to Eq. (4.18), such that $\zeta_n(r_0)$ represents the weight of the n-mode at the unperturbed droplet radius r_0. We further assigned a random phase difference between each n-mode perturbation.

We present in Fig. 4.5[1] examples of droplet patterns obtained with this procedure, where fingering is driven by either viscosity mismatch (left) or by activity (right), in both the exponential (top) and linear (bottom) growth regimes. In the linear growth, activity-driven fingers emerge more distinctively than in the passive droplet; the opposite is observed in the exponential growth. These results, as well as the analytical scalings presented above, demonstrate that the role of activity in fingering depends on the kinetics of the droplet's growth, and is indeed enhanced in the slower, linear growth kinetics. This assessment could potentially provide a basis for the mechanism behind the onset of metastasis, when the bulk growth of the primary tumour slows down or saturates.

The results presented in Figs. 4.4 and 4.5 relate direct observables of the tumour's geometry, and such measurements should indeed be envisaged by experimentalists. Note, however, from Fig. 4.5 that the number of fingers (~ 10) visible at $r_0 \sim 100\,\mu\mathrm{m}$ when $\phi = 1$ is in agreement with the experimental observations shown in [63].

---

[1] This figure is a replacement for Figure 6 of our publication [1] on which this thesis is based. The replacement was carried out due to a numerical error discovered in data used to generate the original figure. The current figure demonstrates the same effect and conclusions and interpretations drawn from it do not change qualitatively.

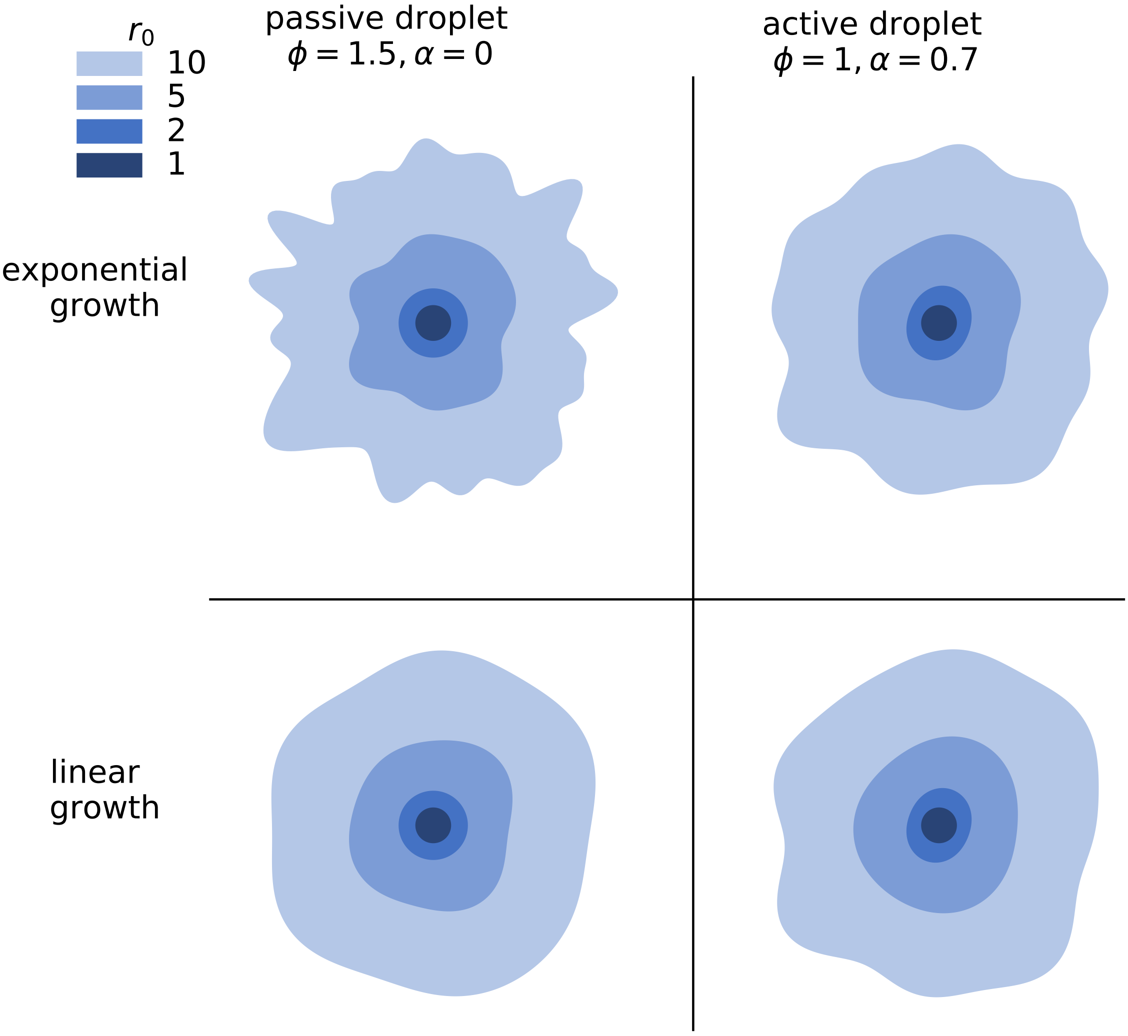

Fig. 4.5 Evolution of a droplet, undergoing exponential (upper row) or linear (lower row) growth, made of a passive (left column) or active (right column) fluid. For comparison, the patterns are shown at the indicated values of the unperturbed radii r_0 (see the scale of shades), even though these are reached at different times in each growth regime. We used the initial amplitude 0.2 for all modes and, to facilitate the morphological comparison, equate the characteristic lengths introduced for each growth kinetics (see ℓ defined in Sec. 4.1 for the exponential growth, and in appendix E.2 for the linear growth): $\left(\frac{2\gamma}{\beta k}\right)^{1/3} = \left(\frac{\gamma}{\beta v_i}\right)^{1/2} \Leftrightarrow 4\beta v_i^3 = \gamma k^2$.

Chapter 5

Conclusions

5.1 Our model so far

The study described in this part of the thesis was originally motivated by observable patterns of fingering in spreading epithelial tumours [63], though we also foresee applications beyond the original motivation. We investigated via modelling the hypothesis that self-propelling forces of the bulk tumour itself can lead to those patterns via a mechanism resembling classical viscous fingering instability. We constructed an active fluid model of a growing and self-propelled tissue that isolates the role of four mechanical parameters (summarised in Tab. 3.1) on its dynamics. The theory is motivated by experimental observations but it is also analytically solvable. We used it to describe the evolution of an embedded 2D circular droplet that could model a carcinoma in an epithelial layer.

Within our model, we have demonstrated how activity increases the propensity for fingering and how this effect is especially important when viscosities of invading and invaded fluid are similar. We also showed how it leads to a reduction in the critical radius, at which fingering of the droplet may begin. We were able to highlight the basic mechanical conditioning required to form interfacial instabilities, which could initiate the tumour protrusions observed at the onset of metastasis. We notably argue that the decrease of the pressure gradient within the droplet by active forces, correlated in direction with the velocity, could be the mechanism which leads to the formation of fingers. We find that the droplet's active traction and growth kinetics are central to shape the instabilities' pattern and further evolution.

All of the results reported were derived analytically, demonstrating strong practical advantages of the simplicity of our model. Our work shows the continued potential of minimal physical models to bring about deep insight and understanding of biological systems.

Our model, after further experimental validation and development, could help predict the minimum tumour size for metastasis, as well as the number of subsequent invasive fingers emerging from the initial mass.

Admittedly, at present our work remains speculative. Therefore, in the next section we list potential experimental validations of the approach. Subsequently, in the final section of this chapter, we describe recommended directions for further research into the model itself, which may result in additional criteria for experimental validation being formulated.

5.2 Further validation of the model

If our work is indeed a realistic description of growth of malignant tissues and the effect we demonstrated within our model is the basis for fingering observed in some tumours and other tissues, the following predictions, experimentally falsifiable at least in principle, would be implied:

1. In circular tumours, the radius necessary for the initiation of fingering should monotonically increase with increasing surface tension, while the number of observed fingers at any higher radius should decrease; this would in general correspond to invasiveness of the tumour decreasing with increasing surface tension. In consistency with predictions of our model, this effect was already experimentally demonstrated *in vitro* for brain tumour spheroids embedded in matrigel. The efficiency of a therapeutic agent dexamethasone was shown to be based on increasing cohesivity and surface tension of the tumour [149]. Negative correlation between surface tension and invasive potential *in vitro* was also demonstrated for lung and prostate cancers and fibrosarcoma [150]. Qualitatively, therefore, this prediction of our model is relatively well established. If more precise, quantitative measurements of this relationship become feasible, our model predicts that fingering starts at a (dimensional) radius $r_c \propto \gamma^{\frac{1}{2}}$, where γ is the surface tension in the case of linear growth and at a radius $r_c \propto \gamma^{\frac{1}{3}}$ in the case of exponential growth. These predictions follow directly from solving for dimensionless r_c the conditions $\sigma_n(r_0 = r_c) = 0$ in Eq. (4.15) and Eq. (E.2) for exponential and linear growth respectively, and then using scalings of the characteristic length scales in both systems, as specified in Sec. (4.1.2) and Sec. (E.2) respectively, to recover the relationship between dimensional r_c and γ for each system.

2. Increased viscosity of the surrounding tissue and lowered viscosity of the tumour should promote fingering directly via the mechanism of the classical viscous fingering

instability. Magnetic resonance elastography has been recently used to measure directly the dynamic modulus, and (indirectly and assuming the Kevin-Voigt viscoelastic model for the tissue) also the relative viscosities of brain cancer and surrounding healthy tissue [151]. Invasive glioblastomas were shown to have much lower viscosity than the surrounding tissue, as opposed to benign (non-invasive) meningiomas, qualitatively confirming our predictions. Measuring viscosity within live cells has become possible in recent years both *in vivo* and *in vitro* by using so-called "molecular rotors"-molecules, whose fluorescence lifetimes depend on local viscosity within the system. Labeling cancerous tissue using such molecules has recently provided quantitative information on microscopic viscosities within individual cells [152, 124]. If these techniques are developed to the point of being able to provide precise information on bulk viscosity of the tumour and its surroundings, our quantitative predictions for the linear rates of growth $\sigma(r_0)$ and the critical radius of growth r_c can be tested further, at least for passive systems.

3. We predict an enhancement of fingering by active forces. Specifically, we predict that the self-propelling force as in Eq. (3.1a) leads to fingering even in the case when viscosities of the tumour and surrounding tissue are similar and this occurs sooner when that force is larger. Measuring the relative viscosities of the tumour and surrounding tissue should be possible using methods referred to in the previous point, as described in [151] and perhaps also using the ones described in [152, 124]. This should enable in the foreseeable future identifying those cases, in which fingering occurs despite a viscosity ratio close to 1, for which our predictions on the role of activity could be better tested. This would likely be a qualitative study; we are not aware of experiments enabling direct quantitative measurements of active traction against the substrate (the α-term in Eq. (3.1a)) of an entire tumour in *in vivo* settings. Qualitatively, however, identifying which of two samples undergoing comparison has higher active forces should be possible; the magnitude of activity in tumours can be inferred using various tools, such as by measuring stochastic fluctuations of the cytoplasm with force spectrum microscopy [153] or by traction force microscopy of *in vitro* cancer cell lines taken from a given tumour [154]. In qualitative consistency with our predictions, both techniques indeed show that higher active stresses generated by breast, prostate and lung carcinoma cells correlate with higher metastatic potential of the tumour they were taken from [154, 153].

4. We predict that, for fingering to occur, the gradient of the pressure perpendicular to the interface of the tumour has to be lower within the tumour, than within the surrounding

tissue. Within our model's predictions, this is true regardless if the fingering is caused by activity or by the viscosity ratio. Any fingering occurring when this condition is violated must stem from different causes than we propose. In principle, measuring when this condition is satisfied should be possible, since reliable experimental tools for measuring pressures within tissues exist and have been applied for tumours [155, 156]. This test could verify if and when fingering occurs precisely via the mechanisms we propose, or if it results from other causes, even when superficial similarities are present.

We believe further predictions can be formulated upon further development of our model. In the next subsection, we describe which aspects of the model should be better understood for this purpose.

5.3 Directions for further modelling research

The relative analytical simplicity of our model allows the investigation of more complex settings, such as heterogeneous droplets in which active forces and/or growth are not uniform. In particular, solving analytically experimentally motivated systems in which activity and/or tissue growth are concentrated within an outer rim of the droplet should be possible. Perhaps this could contribute to understanding the ways in which tumour heterogeneity enhances metastasis (as reviewed in Chapter 1). It is also plausible to analytically compute what happens when these parameters are evolving over time (as was done for the case of time-dependent growth rate, leading to constant growth of the droplet radius, in Subsection 4.3.1). In particular, the patterns of fingering in other growth kinetics commonly encountered in tumours, such as sigmoidal, could be studied, leading to quantitative predictions on the relationship between growth kinetics of the bulk of the tumour and prominence of active and viscous fingering.

The constitutive equations of our model can also be implemented in fluid dynamics simulations. We envisage such studies for systems with high traction forces, where active motions are faster than the growth velocity, and which may indeed be relevant in aggressive forms of cancer and in epithelial spreading. Apart from the biological applications, such studies would also represent, in our opinion, considerable value for fundamental physics of instabilities. What behaviour of a fluid should we expect if it has a non-zero preferred velocity when flowing within an area restricted by boundaries? What happens when these boundaries themselves can deform due to forces acting from the fluid? And what happens when, in addition, there is a second fluid on the other side of that boundary, which also influences its stability or lack of thereof? We believe the active fluid investigated in this thesis constitutes a good model system to address these questions.

Part II

Errors in energy landscapes measured with particle tracking

Chapter 6

Introduction

6.1 Particle videotracking

Microscopy is used to observe motions in tissues, complex materials and nanofluidic devices, on the scale of individual micro- and nano-particles. Sophisticated techniques to extract useful results from microscopy on this lengthscale are required. One of the most important is particle videotracking. The technique serves multiple purposes. It has been used for decades to study biological and soft matter, and has indeed provided valuable information on the microscale dynamics and structure of these systems [157–159]. With this technique, one can for instance probe live-cell microenvironments [160, 161], study the dynamics of individual proteins in natural settings [162, 163], image the viral invasion of host cells [164, 165], etc. Extracting mechanical properties of individual biological molecules has also been shown to be possible by measuring the thermal fluctuations of cytoskeletal and membrane filaments [166–169], and of DNA [170, 171].

Apart from purely biological applications, particle tracking has also been used extensively in synthetic soft matter physics. Hence, central applications of this technique have been to determine the microrheology, diffusion rates or mechanical properties of complex fluids [172–175]. It has also been employed to measure colloidal interactions of electrostatic [176, 177] or entropic [178, 179] origins, and, more recently, to observe particle trapping in microchannels [180–183].

On these length- and timescales, simple inspection of the images is almost never sufficient to extract meaningful results, and statistical analysis of Brownian particle trajectories is usually a prerequisite to extracting observables that can be physically interpreted. The mean-squared displacement (MSD) is often calculated, as a measure of the time- or population-averaged dynamics of the tracked particles. For example, the MSD enables distinguishing between diffusive, driven, sub-diffusive, hopping or trapped motions [173].

Reconstructing the underlying energy landscape guiding the particles' dynamics is another insightful analysis of Brownian trajectories, which has been exploited in many of the aforementioned applications [184, 185, 176–183]. This landscape is an immensely important observable, governing the behaviour of many of these systems, and recovering it correctly is necessary to understand them. Hoze et al. [184] and Masson et al. [185] infer it around neuronal cell membranes from statistics of trajectories of fluorescently labelled proteins. In this case, it determines protein binding to cell membranes, governing both healthy biological functions, such as neurotransmission [185] and elements of disease progression, such as viral invasion of cells [184]. Others [176, 177, 179, 186] infer the interaction potential between colloidal particles held in optical traps to understand electrostatic [176] and entropic [177, 179, 186] forces in various colloidal suspensions, their phase behaviour and stabilization, as well as their adherence to and deviance from existing theories [177, 179]. Yet others have been attempting to assess it precisely in microfluidic devices, in which it is a tool for trapping particles [180–183]. If the landscape in a given device is known precisely, it can be used to infer charges and sizes of particles with previously unknown properties, by placing them within the system and observing their motion [180]. This could perhaps even lead to new methods for detecting individual molecular reactions [180].

All of the aforementioned important applications require efficiency and precision of the first experimental step: recovering the energetic landscape from Brownian particle statistics. However, as we shall see, this part of the process is prone to potentially consequential errors, which may subsequently propagate to all conclusions stemming from the research.

6.2 Errors in particle tracking

Video particle tracking suffers from various sources of errors. In particular, artifacts intrinsic to the imaging detectors can contaminate the trajectory measurements, well beyond the statistical uncertainties arising from finite sampling. Several studies have compared the resilience of tracking methods to these errors [187, 158], and new Bayesian techniques notably tend to improve the robustness of the extracted trajectories [188, 158]. Nevertheless, positioning and trajectory linking are irremediably suffering from errors, which have been recognized to propagate to the measured physical observables [172, 189–196, 181, 197–201].

Most detection errors may be classified into two categories: “static” and “dynamic” [202]. The “static error” typically comes from video signal noise (camera-specific noise, background autofluorescence, etc) and would even affect the localization of an immobile particle [202, 203]. The “dynamic error” is the result of motion blur, due to finite camera exposure time, and occurs when measuring the positions of a moving particle. The propagation of these errors to MSD calculations has been characterized in detail [190, 190, 196]. However, no such systematic description has previously existed for their effects on mapping energetic landscapes. Yet, the need for such studies has been emphasized by the recent experimental work of [181], which notably shows that trapping potentials, extracted from video particle tracking via the Boltzmann distribution, are strongly influenced by the camera exposure time [180].

In this part of the thesis, we show that these errors result in systematic and non-trivial biases in the measured energy landscapes. We derive analytically a relationship between the true and the measured potential that elucidates, among other aberrations, the presence of false double-well minima in the apparent potentials reported in recent studies. We further assess several canonical trapping and pair-interaction potentials, by using our analytically derived results and Brownian dynamics simulations. In particular, we show that the apparent spring stiffness of harmonic potentials (such as in optical traps) is increased by dynamic errors, but decreased by static errors.

Our model of static and dynamic errors allows for the development of efficient corrections schemes, which would allow experimentalists to revise their existing data. We also present a provisional method for reconstructing true potentials from the measured ones. Implications of our work are relevant for a wide class of trapping and interparticle potentials.

This part of the thesis is organized as follows. Chapter 7 describes the model quantifying how localization errors affect the measured potentials, and details the algorithm to verify these predictions. Chapter 8 presents the simulation data to confirm the validity of our formula for specific and pertinent potentials, and further explains a possible strategy to correct experimental results for static and dynamic errors, illustrating them with a step-by-step application of our work to reconstruct a true potential from data polluted by static and dynamic errors. Chapter 9 summarizes our findings and discusses directions for further research.

Chapter 7

Methods

7.1 Static and dynamic errors

In many of the aforementioned experimental studies using particle tracking to calculate the energetic landscape, the statistics of the Brownian particles' positions is measured at equilibrium and assumed to obey the Boltzmann distribution [177, 204, 181, 197], and this is the technique our work focuses on. Note that this analysis requires only localizing particles in each frame of the video, while calculating the MSD involves the additional, and often non-trivial, step of linking the particles' successive positions into trajectories [203].

The relationship between the potential V probed by the trapped particles and the probability density function (pdf) of their positions $\mathbf{r} = (\mathrm{x}_1, \mathrm{x}_2, \mathrm{x}_3)$ is given by $f_{\mathbf{r}}(r) \propto e^{-\beta V(r)}$, where $\beta = (k_{\mathrm{B}}T)^{-1}$ (k_{B}: Boltzmann constant; T: temperature). In our notation, $f_{\mathbf{r}}(r)$ is the joint pdf of $\mathbf{r}$ evaluated at $r = (x_1, x_2, x_3)$, the space coordinates. In principle, the Boltzmann distribution allows experimentalists to recover the energetic landscape by measuring the equilibrium distributions of positions of the trapped Brownian particles using video microscopy. In practice, however, cameras measure a moving average of positions over a shutter time σ, to which a zero-mean random vector ξ resulting from instrumental noise is added [166, 205, 190, 191]:

$$\bar{\mathbf{r}}(t) = \frac{1}{\sigma}\int_{t-\sigma}^{t} \mathbf{r}(s)\mathrm{d}s + \xi \tag{7.1}$$

at time t, with ξ independent of $\mathbf{r}$. The time average in Eq. (7.1) results in motion blur or "dynamic errors", while the added noise produces the "static errors" that would occur even when locating an immobile particle [190]. The validity of the various assumptions (properties of ξ, statistics of illumination and detection) leading to Eq. (7.1) has been discussed elsewhere [190, 206].

Most relevant to quantify the static error is the noise covariance matrix, $E = \langle \xi \xi^{\mathsf{T}} \rangle$, where ξ^{T} is the transpose of ξ, and $\langle \cdots \rangle$ is the average. The noise covariance matrix can often be written as $E = \varepsilon^2 I$ (with I the identity matrix) in 2D particle tracking where the static errors are isotropic in the observation plane [190]. In that case, ε is the spatial resolution of the tracking method, and together with the detector exposure time σ, they quantify the two common sources of errors in particle tracking.

We denote the observed pdf of the measured positions given by Eq. (7.1) as $f_{\overline{\mathbf{r}}}$. Applying $f_{\overline{\mathbf{r}}}(r) \propto e^{-\beta \overline{V}(r)}$ to this "apparent" pdf does not measure the correct potential V in which the particles move, but an apparent potential $\overline{V}$ via:

$$\beta \overline{V}(r) = -\ln f_{\overline{\mathbf{r}}}(r) + \text{constant}, \tag{7.2}$$

with an added, arbitrarily chosen constant that, unless stated otherwise, is ignored in the remaining.

We illustrate in Fig. (7.1) the effects of errors ε and σ on a representative 1D potential: the exact potential is shown in black, and the measured potentials affected by motion blur or static positional uncertainty are given by the colored squares, which are obtained by Brownian Dynamics simulations (our algorithm is explained in subsection 7.3; for illustrative purposes, the errors used here are larger than in the actual experiments, where $\varepsilon \approx 4\,\text{nm}$ and $\sigma \approx 1\,\text{ms}$). While static errors tend to apparently widen the potential (blue squares in Fig. (7.1)), dynamic errors produce the opposite (red squares). These antagonistic effects were already revealed when studying the propagation of the tracking errors to the MSD [190]. Near the potential's minimum, static errors tend to slightly narrow it, while motion blur gives rise to secondary minima, similar to those observed in [181], whose experimental results are shown with the orange disk symbols in Fig. (7.1). The resemblance of these artifacts indicates that motion blur is likely their cause in the measurements. The latter are obtained from 3D tracking experiments, while the simulations are performed in 1D, and the observed discrepancy in amplitude between the red and orange curves may indeed come from this dimensional mismatch (see subsection 8.2).

7.2 Apparent potential

The apparent pdf $f_{\overline{\mathbf{r}}}$ of measured positions can be analytically related to its true counterpart $f_{\mathbf{r}}$ under two main assumptions. First, we assume that the tracked particle undergoes

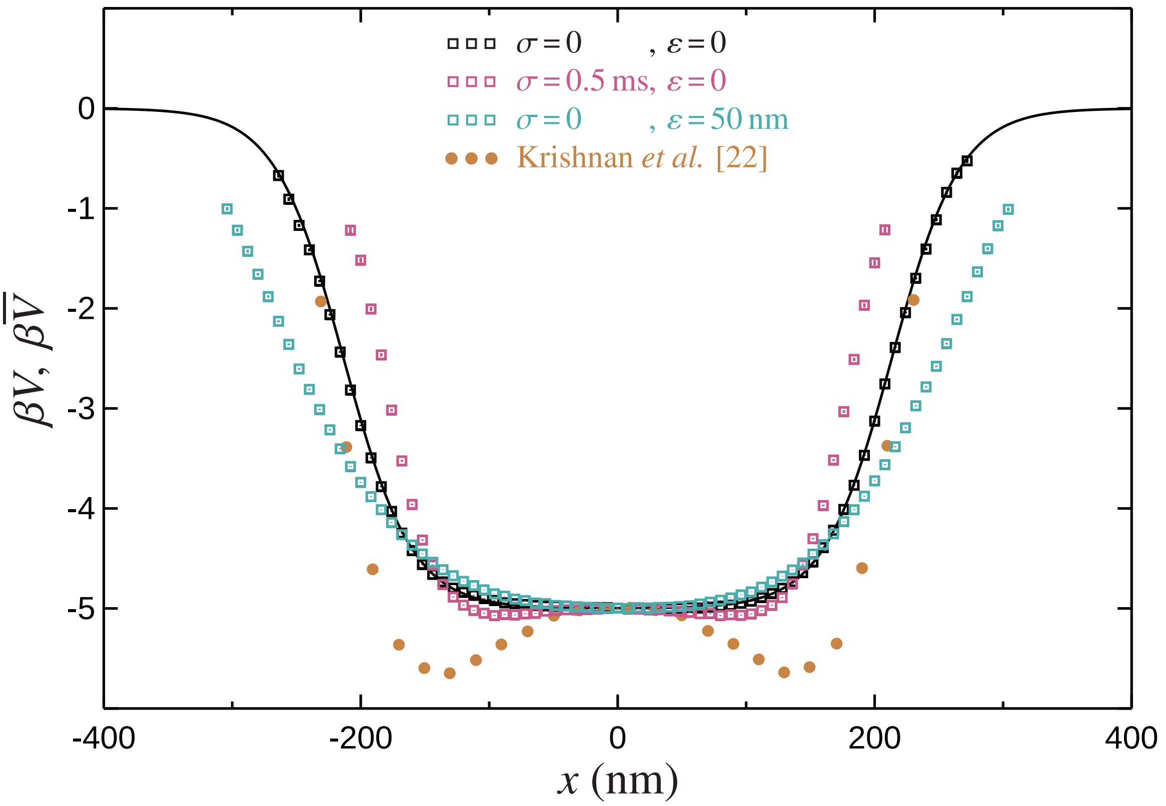

Fig. 7.1 Effect of static and dynamic errors on a 1D potential mapping. The trapping energetic landscape, $\beta V_{\mathrm{ES}}(x) = 2.5[\tanh(3x/a - 4) - \tanh(3x/a + 4)]$, with $a = 160\,\mathrm{nm}$, is shown with the solid line and is chosen to resemble the slice of the 3D electrostatic potential in a microfluidic trap, as measured in [181] using a 100 nm particle with diffusion coefficient $D = 1.8\,\mu\mathrm{m}^2\mathrm{s}^{-1}$ (fill circles are data reproduced from Fig. 3 of their paper). The open squares are results of our simulations (see Section 7.3). The effect of errors shown in their 3D experimental measurements is more pronounced than in our 1D simulations, as the dimension may indeed change the magnitude of the resulting artifacts (see Section 8.2).

overdamped Langevin dynamics. Second, the trapping potential in which the particle moves is considered smooth enough to be approximated, within the typical width of static and dynamics positioning errors, by its second order Taylor expansion. The approximation of an overdamped (i.e., inertialess) dynamics is valid for most video-tracked particles (micron sized colloids, or smaller globular objects like proteins). The condition of potential's smoothness imposes upper bounds for both σ and ε, as we shall see below. Under these assumptions, we can obtain an analytical relationship between $f_{\overline{\mathbf{r}}}$ and $f_{\mathbf{r}}$, the derivation of which is detailed in Appendix F for an arbitrary number of dimensions. The resulting expression for the apparent potential $\overline{V}$ in multiple dimensions (the particular 1D case is given later in this section), as obtained from $f_{\overline{\mathbf{r}}}$ using Eq. (7.2), is

$$\overline{V} = V - \frac{\ln\det(U_{E,\sigma})}{2\beta} + \frac{v^{\mathsf{T}}\Lambda^{-1}\big(U_{E,\sigma} - I\big)\,v}{2\beta D}\,. \tag{7.3}$$

Here $\det(\cdots)$ designates the determinant of a matrix, D is the diffusion coefficient (assumed to be constant) of the particle, and we have introduced the convective velocity and the local relaxation matrix,

$$v = -\beta D\nabla V\,, \tag{7.4a}$$

$$\Lambda = \beta D\nabla\nabla^{\mathsf{T}}V\,, \tag{7.4b}$$

respectively (with ∇ the nabla vector and $\nabla\nabla^{\mathsf{T}}$ the symmetric Hessian matrix operator; Λ has the dimension of an inverse time). We have also defined the following error propagation matrix:

$$U_{E,\sigma} = \big[2(\sigma\Lambda)^{-2}\big(\sigma\Lambda - I + e^{-\sigma\Lambda}\big) + \Lambda E/D\big]^{-1}\,. \tag{7.5}$$

Note from this expression that $U_{0,0} = I$, indeed leading to $\overline{V} = V$ in Eq. (7.3) when both E and σ vanish in the absence of tracking errors.

Eq. (7.3) is valid for both shutter times σ and static errors small enough so that, within the localization errors they induce via Eq. (7.1), third and higher order variations in $V(r)$ may be neglected. We write these conditions, conservatively, as

$$D\sigma\,||\beta\,\nabla V|| + \sqrt{D\sigma} \ll ||\beta\,\nabla^3 V||^{-1/3}\,, \tag{7.6a}$$

$$||E||^{1/2} \ll ||\beta\,\nabla^3 V||^{-1/3}\,. \tag{7.6b}$$

Here the elements $(\nabla^3 V)_{ijk} = \frac{\partial^3 V}{\partial x_i \partial x_j \partial x_k}$, and $||\cdots||$ designates the maximum norm, that is, for a position-dependent matrix $A(r)$ with elements $A_{ij\ldots}(r)$,

$$||A(r)|| = \max_{ij\ldots;\, r\in\Omega} |A_{ij\ldots}(r)| \tag{7.7}$$

is the maximum absolute value of any elements of the matrix over the observable space domain Ω. The left-hand side of the inequality (7.6a) represents the typical displacement of the particle during the time σ, which can be caused by the drift imposed by the trap (first term) and diffusion (second term). Hence, the conditions (7.6) express the requirement for the potential to be “resolvable” to its second order within the localization errors corrupting the particle tracking. We verify in appendix G that these nontrivial conditions indeed provide correct limiting values for σ and ε below which Eq. (7.3) is valid.

Another requirement for Eq. (7.3) to be applicable is $U_{E,\sigma} \geqslant 0$ (positive definite), which ensures that the logarithmic term is well defined. The error matrix E is positive-definite, and we indeed verify that the same holds for the σ-term in Eq. (7.5). However, Λ does not have this property around local maxima or saddle points. In these cases, and under the *additional* condition of a static error larger than a typical Brownian displacement during the time σ (i.e., $\varepsilon > \sqrt{D\sigma}$), we find that $U_{E,\sigma}$ may not be positive definite at these particular points (see an example in 8.1, Fig. (7.2h), in the next section).

In 1D, we rename $x_1 = x$ and Eq. (7.3) is written:

$$\overline{V} = V - \frac{\ln u_{\varepsilon,\sigma}}{2\beta} + \frac{v^2\left(u_{\varepsilon,\sigma} - 1\right)}{2\lambda\beta D}, \tag{7.8}$$

with the convective velocity and the local relaxation rate, Eqs. (7.4), defined in 1D using the first and second derivatives of $V(x)$:

$$v = -\beta D V', \tag{7.9a}$$

$$\lambda = \beta D V'', \tag{7.9b}$$

respectively. The error propagator, Eq. (7.5), now reads

$$u_{\varepsilon,\sigma} = [2(\sigma\lambda - 1 + e^{-\sigma\lambda})/(\sigma\lambda)^2 + \lambda\varepsilon^2/D]^{-1}. \tag{7.10}$$

Finally, in the 1D case, the conditions of validity become

$$D\sigma||\beta V'|| + \sqrt{D\sigma} \ll ||\beta V'''||^{-1/3}, \tag{7.11a}$$

$$\varepsilon \ll ||\beta V'''||^{-1/3}, \tag{7.11b}$$

with $||f(x)|| = \max_{x\in\Omega}|f(x)|$, and are supplemented by the requirement that $u_{\varepsilon,\sigma} > 0$.

One can linearize Eq. (7.3) under the more constraining conditions $||\sigma\Lambda||, ||\Lambda E/D|| \ll 1$, to obtain:

$$\overline{V} = V + \frac{\mathrm{tr}(\sigma\Lambda S_{E,\sigma})}{2\beta} - \frac{\sigma v^{\intercal} S_{E,\sigma} v}{2\beta D}, \tag{7.12}$$

with $S_{E,\sigma} = E/(D\sigma) - I/3$ and $\mathrm{tr}(\cdots)$ designating the trace. In particular, Eq. (7.12) shows the opposite effects of static and dynamic errors on the apparent potentials, and that these errors can negate each other when $\varepsilon^2 = D\sigma/3$, as also observed for the MSD of a diffusing particle [190].

Typical values of the errors are around $\varepsilon \sim 10\,\mathrm{nm}$ and exposure times σ in the range of $0.1 - 1000\,\mathrm{ms}$ for modern CMOS and CCD cameras; the characteristic width a of measurable potentials range from $100\,\mathrm{nm}$ to several microns; usual diffusion coefficients of trackable microspheres in a liquid at room temperature are in the range of $0.1 - 1\,\mu\mathrm{m}^2\,\mathrm{s}^{-1}$ [180, 181, 178, 177, 207]. Hence, in many instances $\varepsilon \lesssim \sqrt{D\sigma} \lesssim 0.1a$, and Eq. (7.3) should indeed be effective for most experimental settings.

7.3 Simulations

In the following, we verify the validity of Eq. (7.3) by comparing it with Brownian Dynamics (BD) simulations for several examples of potentials. An explicit first-order time-stepping algorithm is used to advance the position $\mathbf{r}(t)$ of a particle at time t: $\mathbf{r}(t+\delta t) = \mathbf{r}(t) + \dot{\mathbf{r}}(t)\delta t$, where δt is the time step and $\dot{\mathbf{r}}(t)$ satisfies the following equation [208]:

$$\dot{\mathbf{r}}(t) = -\beta D \nabla V\big(\mathbf{r}(t)\big) + \sqrt{2D/\delta t}\,\mathbf{w}(t), \tag{7.13}$$

which assumes the drag on the particle to be Stokesian and neglects any other hydrodynamic interactions. Here, $\mathbf{w}(t)$ is a stationary Gaussian process that satisfies $\langle\mathbf{w}(t)\rangle = 0$ and $\langle\mathbf{w}(t)\mathbf{w}^{\intercal}(t')\rangle = I$ if $|t-t'| \le \delta t$, $\mathbf{0}$ otherwise.

Each trajectory is 10^9 time steps long, and is then transformed by calculating the average positions over non-overlapping sets of n time steps, $\overline{\mathbf{r}}(t) = \frac{1}{n+1}\sum_{k=0}^{n}\mathbf{r}(t-k\delta t) + \xi$, where

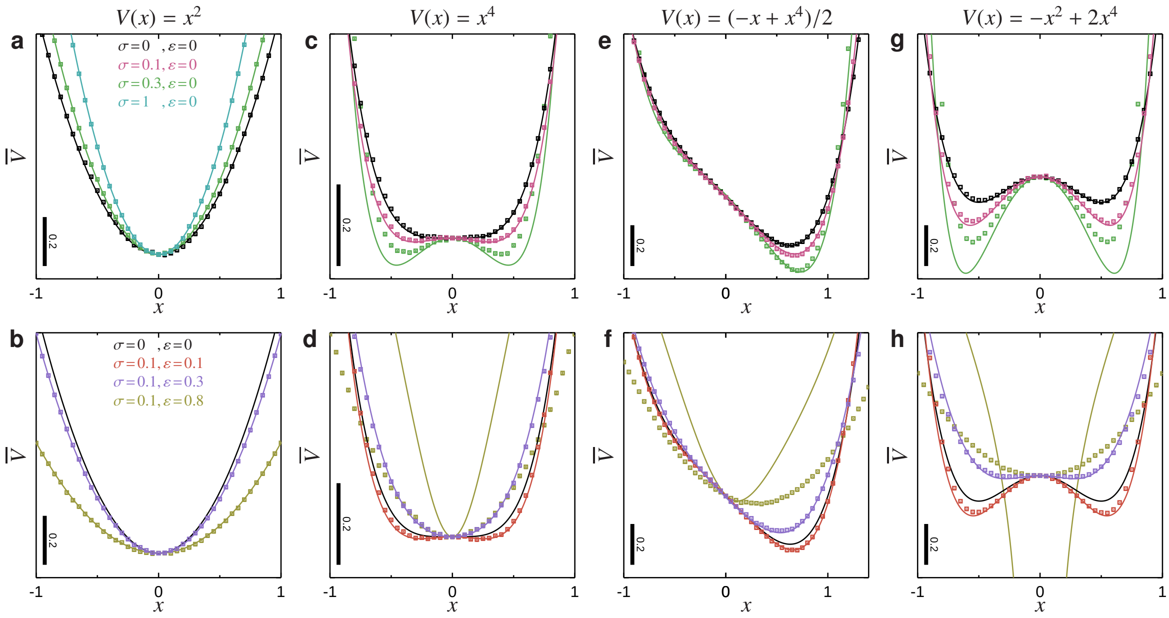

Fig. 7.2 Comparison of Eq. (7.8) (coloured lines on the plots) with BD simulations (symbols) for various σ and ε, and under different 1D trapping potentials (black lines): $V(x) = x^2$ (panels a and b), $V(x) = x^4$ (panels c and d), $V(x) = (-x + x^4)/2$ (panels e and f) and $V(x) = -x^2 + 2x^4$ (panels g and h). The top panels (a, c, e and g) investigate the motion blur with no static errors. The bottom panels (b, d, f and h) concern static errors under a fixed shutter time $\sigma = 0.1$. The conditions in Eq. (7.11) require $\sigma \ll 0.05$ and $\varepsilon \ll 0.3$ for panels c and d, $\sigma \ll 0.07$ and $\varepsilon \ll 0.4$ for panels e and f, $\sigma \ll 0.03$ and $\varepsilon \ll 0.3$ for panels g and h.

$\sigma = n\delta t$ defines the shutter time, and where the added static error ξ is a random, normally distributed vector with $\langle \xi \xi^{\mathsf{T}} \rangle = \varepsilon^2 I$.

In the remaining, we work with dimensionless quantities, where the unit distance a is the characteristic width of the potential trap (meaning $V(|r| = a) - V(0) = \beta^{-1}$), the unit energy is β^{-1}, and the unit time a^2/D. The dimensionless spatial resolution and shutter time are therefore expressed ε/a and $D\sigma/a^2$, respectively. For example, with the values used in Fig. (7.1), one finds $\varepsilon/a = 0.3$ ($\varepsilon = 50\,\mathrm{nm}$ and $a = 160\,\mathrm{nm}$) and $D\sigma/a^2 = 0.3$ ($\sigma = 4\,\mathrm{ms}$ and $D = 1.8\,\mu\mathrm{m}^2\mathrm{s}^{-1}$), as reported by the dashed lines in Fig. (8.3d) for the same simulation data. In these units, δt is chosen to be 5×10^{-3} or less, and n to be 100 or greater. We further verify, for each simulation, that decreasing δt and/or increasing n (while keeping the value σ of interest conserved) does not significantly affect the results shown.

A histogram of the positions with a bin size ≤ 0.05 is then calculated, and we verified that the observed pdf is independent of the bin size when it is chosen in this range. The apparent potential is then extracted from the pdf via Eq. (7.2). For all examples investigated next, we also perform BD simulations without dynamic and static errors and verify that the correct potential is returned by our algorithm (see Fig. (8.1a) and the black symbols in Figs. (7.1), (7.2), and (8.2)).

Chapter 8

Results and Discussion

8.1 1D potentials

We now use Eq. (7.8) to predict the shape of the apparent potential for a few 1D examples presented in Fig. (7.2), and compare the results with the BD simulations described in the previous section. In this figure, the lines are obtained from Eq. (7.8), while the symbols are obtained from the simulations.

The first potential we consider is $V(x) = x^2$ (Figs. (7.2a) and (7.2b)), for which Eq. (7.8) is exact and indeed matches the simulations for any values of ε and σ. This canonical harmonic potential, indicating a linear elastic interaction, is ubiquitous in soft biological systems [209] and in the optical tweezer technique commonly used to probe them [210, 211]. For a general harmonic trap with constant k, $V(x) = kx^2/2$, the apparent potential can be calculated, using Eq. (7.8), as $\overline{V}(x) = \overline{k}x^2/2$ with $\overline{k} = k/u_{\varepsilon,\sigma}$ and for the relaxation rate $\lambda = \beta Dk$. Consequently, the apparent MSD of a particle trapped in such potential reaches, at long time, a plateau $2/(\beta\overline{k}) = 2g_\sigma/(\beta k) + 2\varepsilon^2$ with $g_\sigma = 2(\sigma\lambda - 1 + e^{-\sigma\lambda})/(\sigma\lambda)^2$, as already shown in [190, 190]. Our formula in that case also justifies the corrective approach employed in [180] to evaluate the stiffness of their trapping potentials via the dependency of the MSD plateau with the camera exposure time.

The second potential we examine is $V(x) = x^4$, shown in Figs. (7.2c) and (7.2d), and which has been investigated as a possible confinement landscape for membrane proteins [168]. This trapping potential also resembles the interaction restricting the motion of a particle attached to a substrate by a polymer tether [212, 213]. The tethered particle motion (TPM) technique has been used in recent years to probe the mechanical properties and interaction of various biological macromolecules [214]. Unlike the previous case of a harmonic potential, Eq. (7.8) is an approximation that fails for large values of σ or ε, when the conditions expressed by Eqs. (7.11) are not satisfied. Accordingly, we observe discrepancies between the predicted apparent potential and the simulations (see the green and yellow curves in panels c and d, respectively). However, our formula correctly returns the existence of two symmetric minima in the apparent potential, as observed in the simulation results (and similar to the data presented in Fig. (7.1)), and is accurate for lower (and typically, more experimentally realistic) values of σ and ε. We also note that near the potential's minimum, the dynamic errors tend to apparently widen the trap, with the static errors producing the reverse. This behavior is indeed the converse of what is seen on the higher parts of the trapping branches of the potential (about β^{-1} above its minimum; see Fig. (7.1)).

We also investigate an asymmetric potential, $V(x) = (-x + x^4)/2$ in Figs. (7.2e) and (7.2f), for which Eq. (7.8) also returns an effective approximation of the simulation results when σ and ε verify the conditions Eqs. (7.11). We study, in Figs. (7.2g) and (7.2h), the potential $V(x) = -x^2 + 2x^4$, which is a double-well trap similar to ones observed in several biological systems [214, 215]. It is symmetric and displays a local maximum at $x = 0$ which can be apparently hidden by the static errors (see the purple data, correctly predicted by our formula, in Fig. (7.2h)). Also in Fig. (7.2h), we show an instance where higher values of ε lead to $u_{\varepsilon,\sigma} < 0$ and Eq. (7.8) is undefined around the local maximum of $V(x)$ (yellow curves), as explained in Section 7.2.

We note that overall, Eq. (7.8) is returning an effective approximation of the apparent potential $\overline{V}$ unless the static and dynamic errors originate from particularly large values of ε and $\sqrt{D\sigma}$, respectively, that is, greater than $\sim a/3$.

8.2 2D potentials

We further extend our analysis to 2D potentials and confirm the applicability of Eq. (7.3) in that case. Such potential maps obtained in 2D (or 3D) can be used to characterize, for example, the pore geometries in protein gels [216] or receptors' trapping in cell membranes [207, 217–219]. In Fig. (8.1), we rename $(x_1, x_2) = (x, y)$ and study the potential $V(r) = (x^2 + y^2)^{3/2} + 3(3x^2y - y^3)/4$ (that is, $V(r) = r^3\left(1 + \frac{3}{4}\sin 3\theta\right)$ in polar coordinates), which traps the particle in a 3-branches star.

We show that BD simulations (symbols) are indeed effectively described by Eq. (7.3) (lines), even for values of σ and ε close to the limits set by Eqs. (7.6). We further observe that the effects of the dynamic errors share features of the 1D case. Hence, it also produces apparent local minima (see red contours in Figs. (8.1b) and (8.1c)), but the magnitude of these 2D dents in the potential map tends to be larger than in their 1D counterparts under similar σ (compare Fig. (8.1b) with the red curve in Fig. (7.2c)). This amplification of motion blur artifacts at higher dimension, which we have not assessed in details here, may indeed explain the difference between the experiments and simulations presented in Fig. (7.1). Motion blur also modifies the overall shape by sharpening and extending the corners while narrowing the side edges (compare Figs. (8.1a), (8.1b) and (8.1c) with increasing σ and no static errors). This observation, in particular, does not qualitatively align with the results reported in [192] for particles trapped in a square well (region of free diffusion bounded by impenetrable walls; our model, derived for smooth potentials, cannot be applied for this situation), in which case the apparent potential is harmonic-like. These dissimilarities indeed highlight the non-trivial effects of motion blur.

The static errors have the opposite effect in the observed range of potential near its minimum, where the corners appear flushed (compare Figs. (8.1b) and (8.1d)) and the trap narrower. At higher values of the potential, this effect reverses and the potential indeed appears to be widened by the static errors (while, overall, narrowed by the dynamic errors).

Interaction potential

Eq. (7.3) is written for a Brownian particle diffusing in a trapping potential V. However, it is also correct for a system of 2 Brownian particles with trajectories $\mathbf{r}_1(t)$ and $\mathbf{r}_2(t)$ in a mutual interaction potential $V(|r_1 - r_2|)$. One only needs to replace in Eq. (7.3) the diffusion constant D with the sum of the diffusion constants of the two particles $D_1 + D_2$, and noise covariance matrix with the sum of the individual noises $E_1 + E_2$. If the particles are identical and tracked in 1D or 2D, the substitutions are $D \to 2D$ and $\varepsilon^2 \to 2\varepsilon^2$.

This reasoning is valid because Eq. (7.1) can also be written identically for the two-particle system, with $\mathbf{r} = \mathbf{r}_1 - \mathbf{r}_2$ now representing the separation between the interacting particles, and with the added individual noise vectors ξ_1 and ξ_2 assumed to be mutually independent. The system's dynamics are now also governed by Eq. (7.13) for the particle separation $\mathbf{r}(t)$, with D replaced by $D_1 + D_2$, as obtained by subtracting each Brownian dynamics equation describing $\mathbf{r}_1(t)$ and $\mathbf{r}_2(t)$. From there, the derivation of Eq. (7.3), as described in appendix F, proceeds in an identical manner.

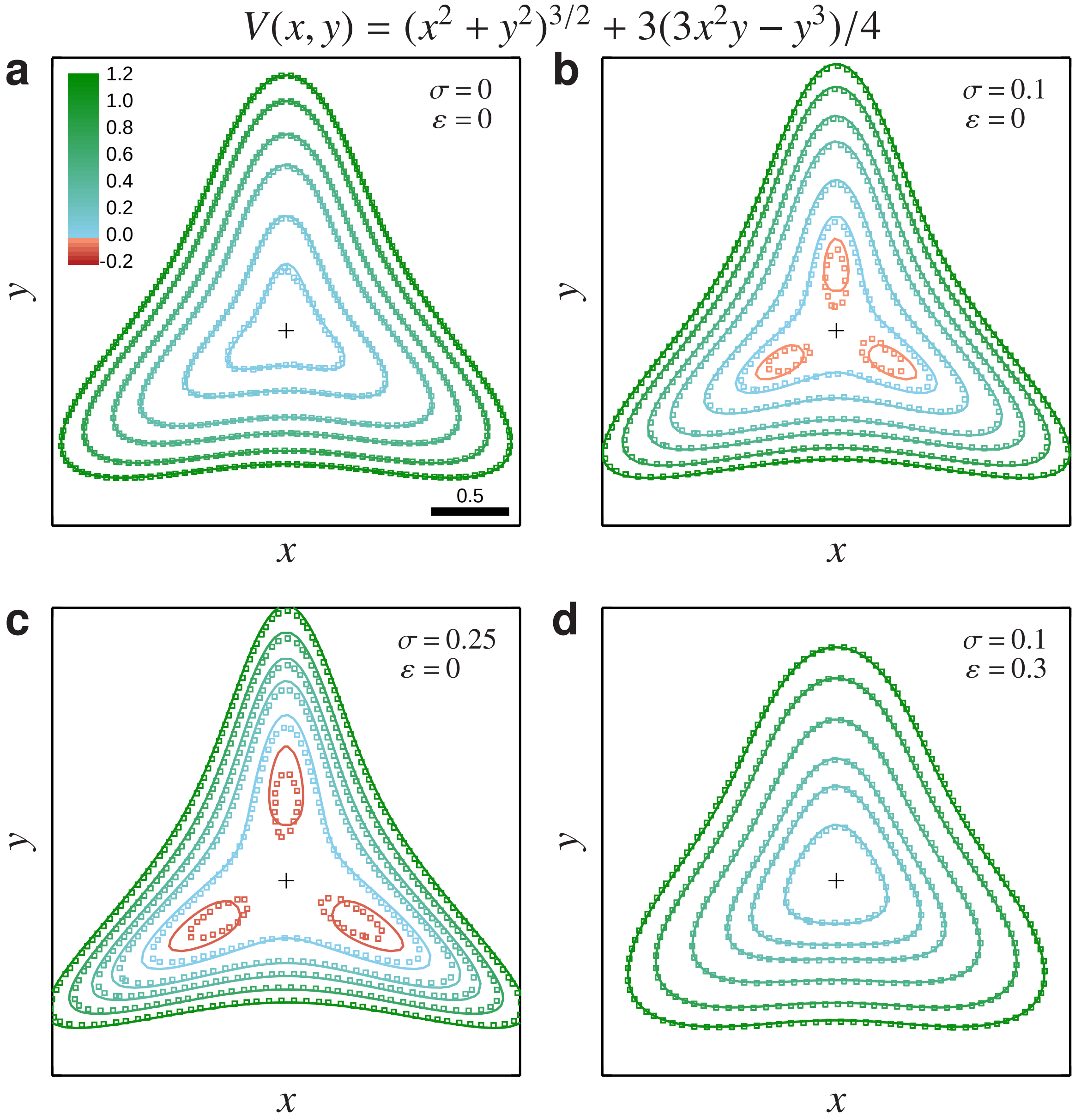

Fig. 8.1 Comparison of Eq. (7.3) with BD simulations for various σ and ε, in the 2D trapping potential $V(x,y) = (x^2+y^2)^{3/2} + 3(3x^2y - y^3)/4$. The symbols are contours extracted from the simulations, while the lines are their counterparts obtained using Eq. (7.3). Panels a-c are for increasing dynamic errors but no static errors, while panel d includes both effects. The cross indicates the point $(0,0)$ and the outermost contour is at $V = 1.1$ in all 4 panels. The conditions of Eqs. (7.6) require $\sigma \ll 0.1$ and $\varepsilon \ll 0.5$ over the observed domain.

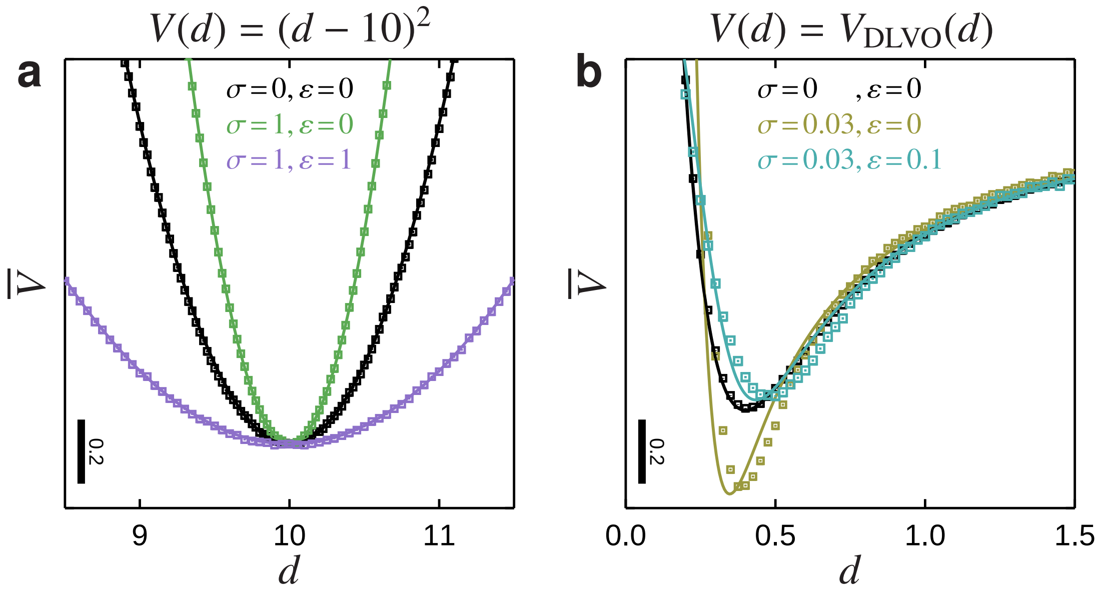

Fig. 8.2 Comparison of Eq. (7.8) with the simulations of two identical Brownian particles interacting via the potential $V(d) = (d-10)^2$ (panel a) and via $V(d) = V_{\mathrm{DLVO}}(d) = \frac{250e^{-10d}}{d+10} - \frac{50/3}{(d+10)^2} - \frac{50/3}{d(d+20)} - \frac{1}{3}\ln\frac{d(d+20)}{(d+10)^2}$ (panel b). In both panels, the symbols are BD results, and the lines are calculated using Eq. (7.8) with the substitutions $D \to 2D$ and $\varepsilon^2 \to 2\varepsilon^2$. The conditions in Eqs. (7.11) require $\sigma \ll 0.01$ and $\varepsilon \ll 0.2$ for panel b.

We numerically verify Eq. (7.8) for two interaction potentials between identical particles in 1D motion, and the results are presented in Fig. (8.2). The first potential models two particles connected by a linear spring with rest length 10, $V(d) = (d-10)^2$ where d is the distance between the particles' surface. For this harmonic potential, Eq. (7.8) is exact (see Fig. (8.2a)) for all values of σ and ε. We perform this simulation to verify that the substitutions $D \to 2D$ and $\varepsilon^2 \to 2\varepsilon^2$ are indeed correct.

A relevant interaction in colloidal science is modeled by the Derjaguin-Landau-Verwey-Overbeekthe (DLVO) theory. For a typical system of trackable particles, the potential may be written as [176]:

$$\begin{aligned} V_{\mathrm{DLVO}}(d) = & A_{\mathrm{y}}\frac{\rho e^{-d/\lambda}}{d+2\rho} - \frac{A_{\mathrm{c}}}{6}\left[\frac{2\rho^2}{(d+2\rho)^2}\right. \\ & \left. + \frac{2\rho^2}{d(d+4\rho)} + \ln\frac{d(d+4\rho)}{(d+2\rho)^2}\right], \end{aligned} \tag{8.1}$$

where ρ is the particles' radius, $d+2\rho$ is the distance separating the two particles' centers, λ is the Debye length, A_{y} is a constant of the screened Coulomb repulsion and A_{c} is the Hamaker constant. For a realistic example, with $\rho = 500\,\text{nm}$ latex particles, having $10^{-4}\,\text{C}\,\text{m}^{-2}$ charge density, and immersed in a 1:1 electrolyte with $10^{-3}\,\text{M}$ ionic strength, then $\lambda = 10\,\text{nm}$, $A_\text{y} = 50\beta^{-1}$ and $A_\text{c} = 2\beta^{-1}$ [176, 220]. To perform simulations of two Brownian particles interacting with this potential, we set the unit of length to $a = 10\lambda$ (see the resulting dimensionless expression of $V_\text{DLVO}(d)$ in the caption of Fig. (8.2)). The particles are further trapped by a parabolic branch for $d \geq 5a$, which mimics the effect of the line-scanned optical tweezer used to perform experimental measurements of this kind [178].

The results of our simulations for the DLVO potential are shown in Fig. (8.2b), and Eq. (7.8) is in reasonable agreement with these data. The effect of dynamic errors is to apparently deepen the interaction potential, shorten its range and steepen its variations around the minimum (see yellow curves in Fig. (8.2b)). Such qualitative differences between true and observed potentials would also occur with interactions of similar profiles in the attractive range (e.g. depletion interaction). These discrepancies indeed resemble previously reported mismatches between the experiments and theory [179, 221], which may be also the result of dynamic errors in the measurements.

8.3 Recovering the true potential from the apparent potential

We have shown, analytically and numerically, how motion blur and static errors distort the true potential. However, while predicting the shape of the apparent potential $\overline{V}$ from the true potential V is possible exactly using Eq. (7.3), in practice in any experimental system we would be interested in inverting this relationship and inferring V from $\overline{V}$, since only the latter is directly experimentally accessible. Unfortunately, this step is less trivial and the optimal strategy remains an open question. We now go over some of the provisional procedures we develop.

Eq. (7.3) is a second-order differential equation that could be solved numerically for V after measuring $\overline{V}$. However, solving it even in principle requires at least some background knowledge of V. This is because this type of second-order differential equation can only be solved if two boundary conditions on V are specified. One of them can be determined by arbitrarily setting the value of V at a particular location, which is always consistent with the underlying physics. However, the second boundary condition does carry physical information and has to be provided by some background information on the potential in question or assumed. Even then, however, solving numerically non-linear second-order differential equations is not trivial. We could not implement a systematic and general solution using common solver packages.

Instead, we have developed two provisional procedures, which allow for obtaining an estimation of the true potential from the apparent potential, which we will go through and illustrate with examples. First, however, we will briefly discuss an algorithm which allows for preliminary assessing if positioning errors are significant in the first place.

8.3.1 Assessing if positioning errors are significant

The measured potential must be first approximated to a functional, mathematical form, for example fitted to a power series, using any build-in package for polynomial fitting in the data analysis software. To assess if motion blur and positioning uncertainty can be neglected, one can apply the transformation $V \xrightarrow{(7.3)} \overline{V}$ described by Eq. (7.3) to the fitted apparent potential, that is calculating the "transformed apparent" potential $\overline{\overline{V}}$ via $\overline{V} \xrightarrow{(7.3)} \overline{\overline{V}}$. If differences between $\overline{V}$ and $\overline{\overline{V}}$ are within experimental error bars, no correction needs to be applied. This reasoning is justified by the fact that the transformation described in Eq. (7.3) affects the function it is applied to by a comparable magnitude when applied for the second time, compared to when it is applied for the first time, as we have numerically verified. Hence, if the differences between $\overline{V}$ and $\overline{\overline{V}}$ are negligible, so are the changes between V and $\overline{V}$ and positioning errors are inconsequential for the system studied. In the opposite case, in which the difference between $\overline{\overline{V}}$ and $\overline{V}$ exceeds experimental error bars, one must correct for motion blur and position uncertainty. We now discuss in turn two potential strategies of doing so.

8.3.2 Correcting for positioning errors

Strategy 1: Polynomial fitting of potentials

If applying Eq. (7.3) to the apparent potential recovered from data shows changes exceeding experimental error bars, one can estimate the true potential by applying a polynomial coefficient fitting of Eq. (7.3). For example, if in 1D $||\sigma\lambda|| < 1$ and $\varepsilon^2 < D\sigma$, one can

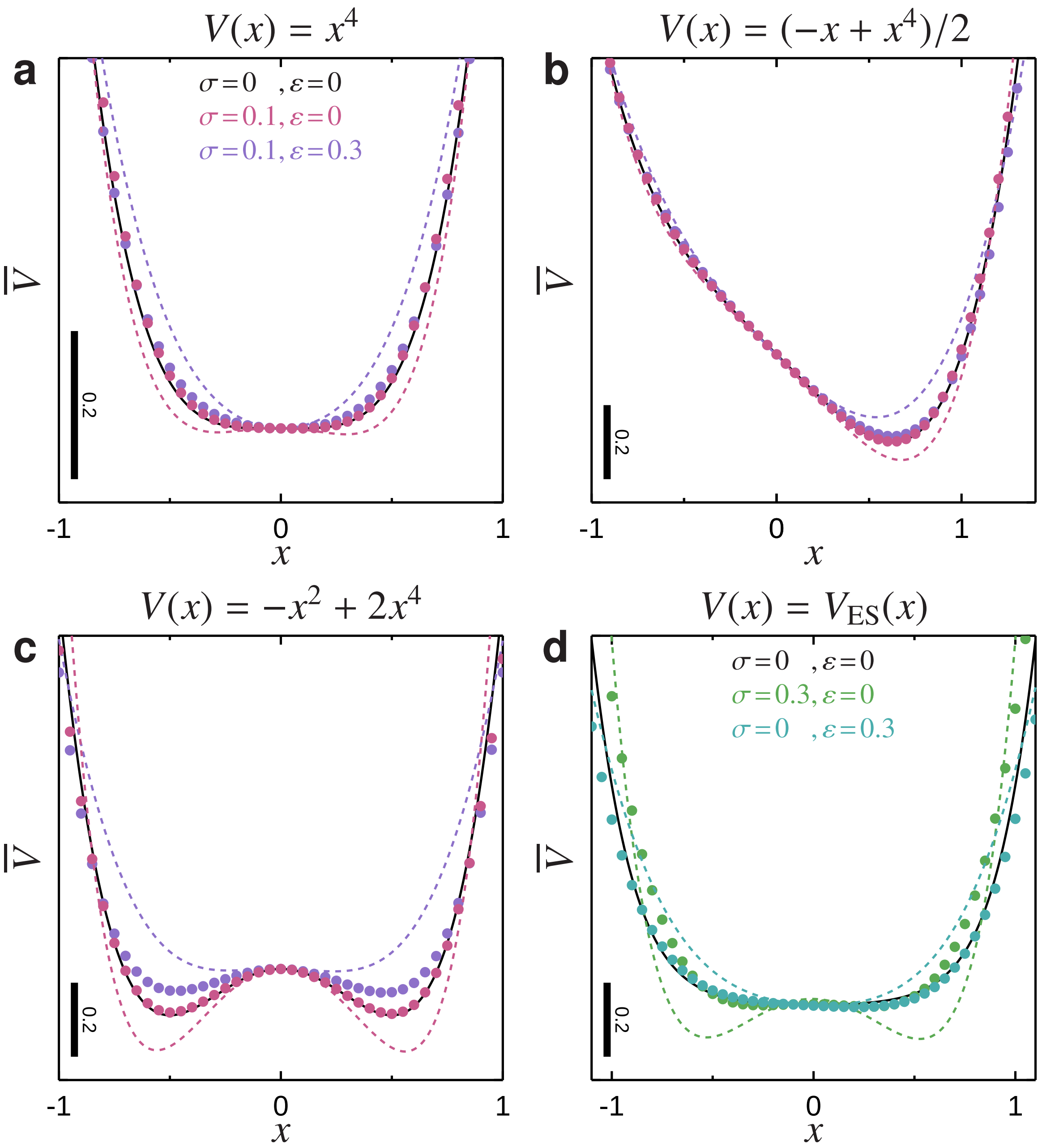

Fig. 8.3 Corrections of the errors using polynomial fitting. In all panels, the solid lines show the original potentials, while the dashed lines are polynomial fits of the apparent potentials as measured from simulation data affected by the indicated dynamic and static errors. For each set of errors, the symbols show the corrected potentials using polynomial coefficient fitting following Eqs. (8.2) and (8.3). Panel a uses data for $V(x) = x^4$ (see Figs. (7.2c) and (7.2d)), panel b is for $V(x) = (-x+x^4)/2$ (see Figs. (7.2e) and (7.2f)), panel c for $V(x) = -x^2+2x^4$ (from Figs. (7.2g) and (7.2h)), and panel d for $V(x) = V_{\mathrm{ES}}(x)$ as defined in the caption of Fig. (7.1) with $a = 1$.

efficiently approximate Eq. (7.8) by:

$$\begin{aligned}\beta\overline{V} = \beta V + s_{\varepsilon,\sigma}\frac{\sigma\lambda - \sigma v^2/D}{2} \\ + (1-6s_{\varepsilon,\sigma}^2)\frac{\sigma^2\lambda^2}{24} - (1-12s_{\varepsilon,\sigma}^2)\frac{\sigma^2\lambda v^2/D}{24} \\ + (1+10s_{\varepsilon,\sigma} - 60s_{\varepsilon,\sigma}^3)\frac{\sigma^3\lambda^2 v^2/D}{120} + c\,,\end{aligned} \tag{8.2}$$

with $s_{\varepsilon,\sigma} = \frac{\varepsilon^2}{(D\sigma)} - \frac{1}{3}$, as obtained by a second order expansion of $\ln u_{\varepsilon,\sigma}$ and $(u_{\varepsilon,\sigma} - 1)/(\sigma\lambda)$ in $\sigma\lambda$ (one order beyond Eq. (7.12)). In the above equation, c is the constant found in Eq. (7.2). We next write $\beta\overline{V}(x) = \sum_{k=0}^{p} \overline{c}_k (x/a)^k$ and $\beta V(x) = \sum_{k=0}^{p} c_k (x/a)^k$ as two polynomial expansions of degree p, and where $\{\overline{c}_k\}_{k=0\ldots p}$ are the fitting parameters for the measured potential. Upon substituting these expressions into Eq. (8.2), and comparing the polynomial coefficients, we obtain a system of equations:

$$\begin{aligned} f_0(c, c_0, c_1, c_2) &= \overline{c}_0 \\ f_1(c_1, c_2, c_3) &= \overline{c}_1 \\ &\ldots \\ f_{p-3}(c_1, \ldots, c_{p-1}) &= \overline{c}_{p-3} \\ f_{p-2}(c_1, \ldots, c_p) &= \overline{c}_{p-2} \\ f_{p-1}(c_1, \ldots, c_p) &= \overline{c}_{p-1} \\ f_p(c_1, \ldots, c_p) &= \overline{c}_p \end{aligned} \tag{8.3}$$

where the functions $\{f_k\}_{k=0\ldots p}$ can be obtained using a symbolic mathematical software. These are $p+1$ equations for the $p+2$ unknowns $c, c_0, c_1, \ldots, c_p$, the missing equation being the one that sets c_0, which can be assigned arbitrarily by choosing, for example, $V(0) = \overline{V}(0)$ (that is, $c_0 = \overline{c}_0$). This system is therefore well-posed, at the cost of artificially truncating the polynomial expansion for both $V(x)$ and $\overline{V}(x)$ to the same degree and it can be numerically solved to obtain the coefficients $\{c_k\}_{k=0\ldots p}$ of the original potential from the fitting parameters $\{\overline{c}_k\}_{k=0\ldots p}$ and the known values of σ, ε and D.

We distribute through GitHub (https://github.com/savin-lab/potential-correction) an implementation of this method, which we apply in Fig. (8.3) to several of the canonical potentials investigated in this paper. We observe that we can indeed recover the appropriate profiles, notably eliminating the apparent double potential wells (see Fig. (8.3a) for $\sigma = 0.1$ and $\varepsilon = 0$, and Fig. (8.3d) for $\sigma = 0.3$ and $\varepsilon = 0$), and, on the contrary, restoring lacking features of the true potential that are flushed by the static errors (see Fig. (8.3c) for $\sigma = 0.1$ and $\varepsilon = 0.3$). The residual discrepancies observed in Figs. (8.3c) and (8.3d) may result from using the approximation given by Eq. (8.2), and/or the inaccuracy of the polynomial fits.

However, the polynomial fits, obtained for power series with degree p between 6 and 12, are chosen so as to obtain the best match with the original potential. It is worth noting that, for a given potential, as the degree of the polynomial fitting is increased, the obtained fitted function typically stabilizes around the optimal value, before deteriorating again and producing visibly unreliable results. However, a prior knowledge of the probed potential is normally not available and we do not yet know in general how to recognize which degree of polynomial fit p is most accurate for a given system.

In practice, we anticipate that the best choice of p reflects a compromise between fitting the experimental data as accurately as possible, without capturing features originating from statistical uncertainty over small length scales. A natural criterion for choosing the fitting length scale, and hence p, could be based on the terms of Eq. (7.11) that sets the validity of Eq. (7.8) and that is verified in appendix G. but needs future work to become a complete and reliable algorithm.

We believe this strategy has a great potential and is the one more systematic and universal of the two we propose, but requires further validation and exploration to offer a systematic and robust numerical method to recover V from $\overline{V}$. We therefore proceed to discussing an alternative provisional procedure, fit for this purpose.

Strategy 2: Assessment based on the difference between $\overline{V}$ and $\overline{\overline{V}}$

As argued in Sec. 8.3.1, one can define a "transformed apparent" potential $\overline{\overline{V}}$ via applying Eq. (7.3) to the measured apparent potential $\overline{V}$. For moderate positioning errors one expects the difference between $\overline{V}$ and $\overline{\overline{V}}$ to be close to the difference between V and $\overline{V}$, since the transformation described in Eq. (7.3) affects the function it is applied to by a comparable magnitude when applied for the second time, compared to when it is applied for the first time. Therefore, we postulate that $V \approx 2\overline{V} - \overline{\overline{V}}$. In the subsequent section, we show an example of applying this technique to a simulated energy landscape, motivated by experimental data.

8.4 A manual on correcting experimental data for positioning errors

Currently, in our opinion, the recommended strategy for correcting for motion blur and static errors affecting a measured, apparent potential $\overline{V}$ is the following, two step algorithm:

1. Verify if $\overline{\overline{V}} - \overline{V}$ exceeds experimental error bars (note the "transformed apparent" potential $\overline{\overline{V}}$ is the function obtained from applying the transformation defined by Eq. (7.3) to $\overline{V}$. If it does not, $V \approx \overline{V}$ and no further adjustments need to be made.
2. If $\overline{\overline{V}} - \overline{V}$ does exceed experimental error bars, V is best approximated by $V \approx 2\overline{V} - \overline{\overline{V}}$

The procedure is carried out and illustrated in Fig. (8.4) on data from a Brownian Dynamics simulation of a fragment of a cosinusoidal energy landscape, inspired[1] by ones observed in nanofluidic channels [222]. Note the figure presents only a small fragment of a wide energy well restricted on both sides by an energy barrier, guaranteeing the particle does not escape the well and that its position statistic indeed does satisfy a proper Boltzmann distribution. The simulation is carried out in a dimensionless system of units, as defined in Chapter 7. The figure demonstrates that, however provisional our current method of recovering the energy landscape may be, it’s application improves the accuracy of the results, removing most of the bias due to motion blur and static errors.

---

[1] Oral communication with Dr Yizhou Tan.

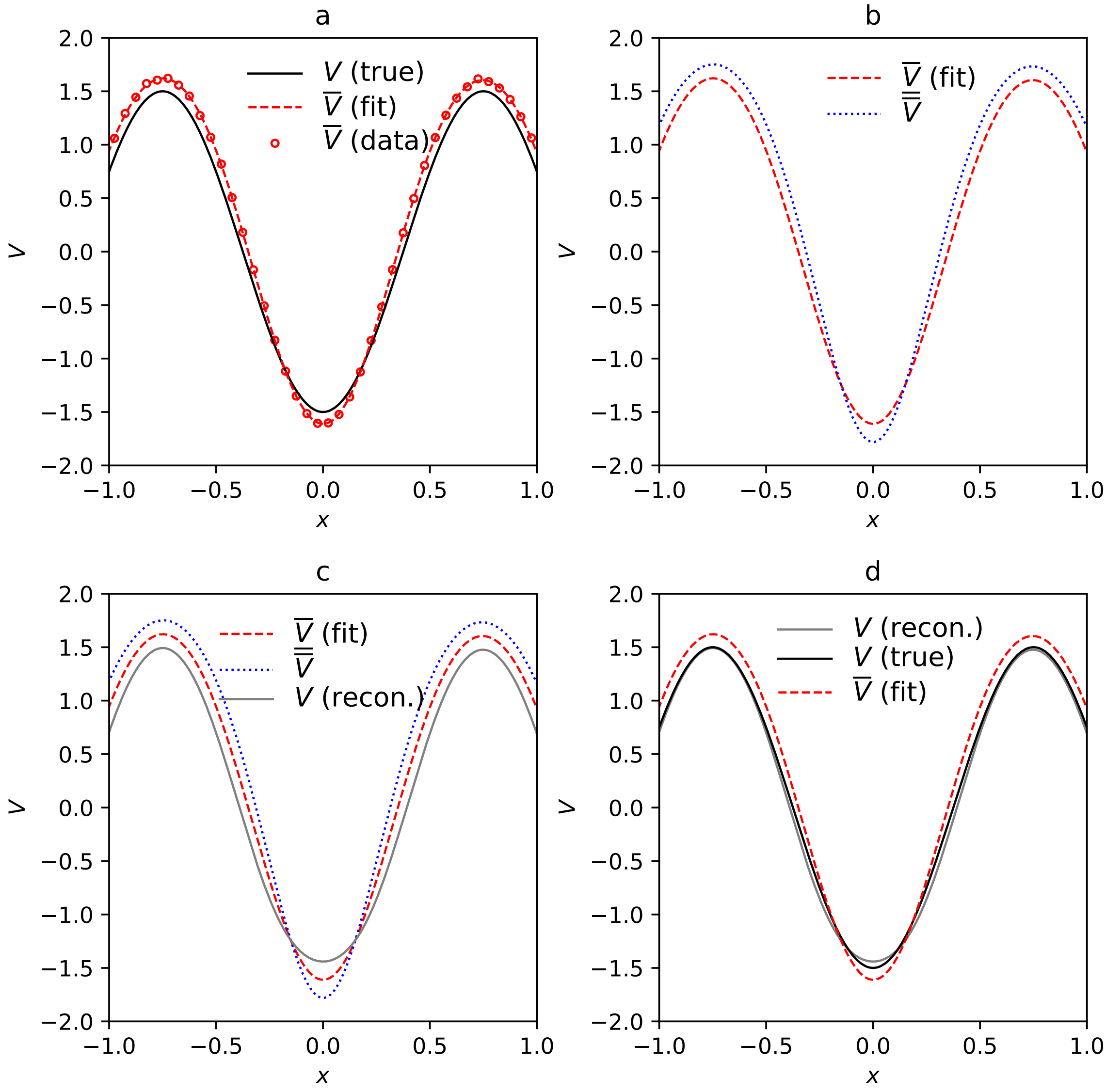

Fig. 8.4 Example of reconstructing an energy landscape. (a) The true energy landscape is given by $V(x) = -1.5\cos\left(\frac{4}{3}\pi x\right)$ (black, solid curve), but a Brownian Dynamics simulation of a measurement based on video tracking a particle with positioning errors $\sigma = 0.033$ and $\varepsilon = 0.005$ produces distorted data on the apparent potential $\overline{V}$ (red markers). (b) Applying the transformation given by Eq. (7.3) to a Taylor series fit of $\overline{V}$ (red curve) produces a "transformed apparent potential" $\overline{\overline{V}}$. Since $\overline{\overline{V}} - \overline{V}$ is substantial, correcting for positioning errors in desirable. (c) The correcting procedure exploits the approximation $V \approx 2\overline{V} - \overline{\overline{V}}$, producing a reconstruction of the true potential V (grey curve). (d) The reconstruction proves a much better estimate of the real energy landscape than the uncorrected apparent potential.

Chapter 9

Conclusions

In this part of the thesis, we explained how motion blur and position uncertainty can affect measuring energetic landscapes using particle tracking. We have determined the effects of dynamic (resulting from motion blur) and static (resulting from instrumental noise) errors on recovering energy landscapes from measured Brownian particle position distributions. We have shown that these two phenomena are the source of nontrivial, systematic biases in the measurements, potentially leading researchers to read out and interpret an incorrect apparent potential. In particular, we have described the phenomenology of these effects in more detail on some canonical trapping potentials: harmonic, double well, asymmetric, in 1D and 2D, as well as interaction potentials. For the harmonic case, the contaminated potential is also harmonic with an apparent stiffness constant that can be exactly calculated.

Using our results it is possible to predict if static and dynamic errors significantly distort measurements in a given system. Equation (7.3) for predicting the apparent potential is accurate in many setups, and can be easily implemented directly for a wide class of systems to determine if motion blur and position uncertainty pose a significant threat to the accuracy of results. Inverting Eq. (7.3) to obtain the true potential from the apparent potential poses a challenge for numerical mathematics. We also propose in this work practical strategies to perform this task. Although further work is needed, one of them seems to promise a stable and reliable reconstruction method. We need now to assess its performances under real-world, experimental conditions.

We conjecture that the effects of these measurement errors may have been overlooked in some existing experimental works [179, 221]. Hence, we recommend that the effects of these errors should be assumed one of the possible explanations for unexpected results obtained when using particle tracking methods. Including explicit information about the used shutter times, tracking parameters and noise characterization [202], should now become a standard practice in reporting research involving Brownian particle video tracking.

Further research needs to be carried out in this direction. Our study should be followed by a detailed review of existing experimental results. As already mentioned, it is also necessary to continue developing algorithms to invert Eq. (7.3) for calculating the true potential from the apparent potential, $\overline{V} \to V$. Furthermore, this type of error propagation analysis should also be made for other observables that are extracted from Brownian particle tracking data (e.g., pair or van Hove correlation functions [223], two-point microrheology [224], etc.). These problems should be pursued in a future study conducted in collaboration with experimental groups experienced in particle videotracking.

Our derivation of Eq. (7.3) in appendix F relies on the assumption that the spatial shape of the studied energetic landscape can be approximated as a parabola on the lengthscale of a typical particle displacement within a single shutter time. Improving this approximation to treat the landscape's shape more accurately might also be worthwhile. Also, our work so far only applies to particles undergoing classical Brownian motion and drift. Extending it to particles undergoing other types of random motion, such as hopping diffusion would be necessary to understand the effects of motion blur and position uncertainty on measuring such systems.

Appendix A

Comparing fingering in a rectangular channel in our model and the Toner-Tu model

In this Appendix, we discuss fingering on the boundary of an active fluid described by Eqs. (3.1) in a simpler set-up than that explored in Chapter 4. As seen in Fig. (A.1), 2 fluids, separated by an interface, move in a 2D rectangular channel. The invading fluid is injected far away from the interface. It displaces a second fluid residing in the other part of the channel. Like in Chapter 4, the displaced fluid is passive, while the invading fluid is active. There is no cell division in this set up ($k = 0$); the flow is entirely due to injection of the active fluid on one end of the channel.

The set-up we study here is the one used by Saffmann and Taylor in their landmark paper, which initiated the theory behind viscous fingering [117]. Therefore, we are able to assess the effects of activity on viscous fingering in this traditional set-up by comparing our result with theirs.

We then investigate fingering in the same geometry, but when the active fluid is described by the Toner-Tu model, instead of Eqs. (3.1). This Appendix then compares the effects of activity on fingering when using our model and the Toner-Tu model and finds strong qualitative similarity. This is the only set-up in which such a comparison is possible, since the Toner-Tu model is not analytically solvable in other systems explored in this thesis.

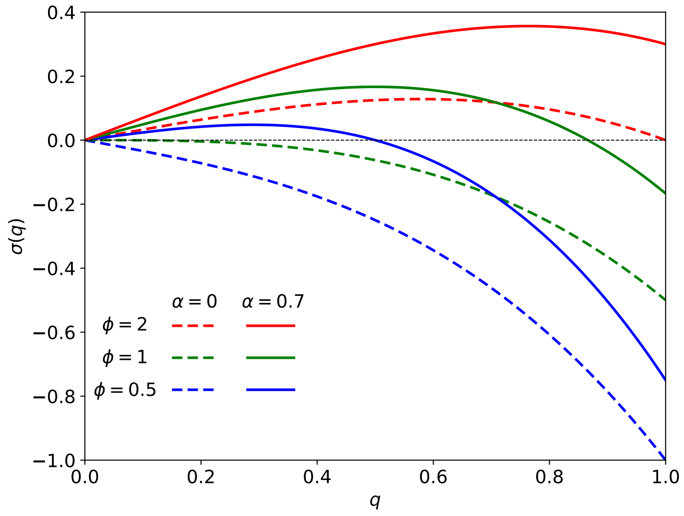

Fig. A.1 System described in this Appendix: a 2D rectangular channel with an active fluid described by Eqs. (A.1) or (A.21), is displacing a passive fluid modelled by Eqs. (A.2) or (A.22) respectively. The interface undergoes periodic perturbations whose linear stability is investigated in this Appendix.

A.1 Our model

This system is the simplest conceivable realisation of our model described in Chapter 3, and is also the most convenient in terms of illustrating the various aspects of the model's behaviour, so we go over the derivation in considerable detail.

We define the dimensionless variables as follows. Distances are re-scaled by a characteristic length $\ell = \sqrt{\frac{\gamma}{\beta v_i}}$, where v_i is the magnitude of the velocity of the moving unperturbed interface. Times are rescaled by the reference time $t_r = \frac{\ell}{v_i}$. Therefore the velocity of that interface is 1 in this dimensionless system of variables. The viscosity ratio of the active and displaced fluid is $\phi = \beta'/\beta$, as previously. Activity is made dimensionless using a reference activity, defined as $\alpha^* = \beta v_i$, while pressure using a reference pressure $p* = \beta \ell v_i$. As in Chapter 4, the dimensionless versions of the variables are described using the same letters as their dimensional counterparts.

The equations of motion in this system of variables in the active fluid have the form:

$$\nabla p = -\mathbf{v} + \alpha \frac{\mathbf{v}}{|\mathbf{v}|}\,, \tag{A.1a}$$

$$\nabla \cdot \mathbf{v} = 0\,, \tag{A.1b}$$

and in the passive fluid have the form:

$$\nabla p' = -\phi \mathbf{v}' , \tag{A.2a}$$

$$\nabla \cdot \mathbf{v}' = 0 , \tag{A.2b}$$

The boundary conditions at the interface $h(x,t)$ are:

$$v_y|_{y=h} = v'_y|_{y=h} = \partial_t h , \tag{A.3a}$$

$$p|_{y=h} + \partial^2_{xx} h = p'|_{y=h} . \tag{A.3b}$$

Note the variable of surface tension γ effectively dissapears from the equations, due to our choice of dimensionlesss variables.

Technically, the system also has other boundary conditions: the mass continuity boundary condition on the sides of the channel requires $v_x = 0$, which would in principle restrict the allowed periodic perturbation wavelengths to a set of discrete values. However, we further presume, like in the original Saffman-Taylor set-up [117], that the channel is very wide compared to the wavelength and size of the interfacial perturbations. In practice, therefore, these boundary conditions are inconsequential as we study the dynamics of the system.

Defining as i the y- coordinate of the unperturbed interface at a given time, the unperturbed hydrodynamic fields in the (x,y) coordinate system are:

$$\mathbf{v}_0 = (0,1) , \qquad p_0 = (\alpha - 1)(y - i) + p_0|_{y=i} , \tag{A.4a}$$

$$\mathbf{v}'_0 = (0,1) , \qquad p'_0 = -\phi(y - i) + p_0|_{y=i} . \tag{A.4b}$$

Analogously to the case of a circular droplet, we investigate infinitesimal interfacial perturbations of the form $h = h_0 + \delta h$, with

$$\delta h \propto f_q(t) e^{iqx} , \tag{A.5}$$

where q is the wavelength of the periodic perturbation, and where $f_q(t)$ describes its time evolution (with $\lim_{t\to 0} f_q(t) = 1$ for all q). Analogously, periodicity in q is assumed for perturbations of hydrodynamic fields: $(\delta p, \delta p', \delta \mathbf{v}, \delta \mathbf{v}') \propto f_q(t) e^{iqx}$, around the solution given by Eqs. (A.4). The q-mode's linear rate of growth is defined by

$$\sigma_q(h_0) = \lim_{t \to 0} \frac{\partial_t f_q(t)}{f_q(t)} . \tag{A.6}$$

Perturbations in Euclidean coordinates in the active fluid satisfy the following equations to linear order (see Eq. (C.1) in Appendix C for a general form of these perturbations and a discussion of its implications):

$$\partial_y \delta p = -\delta v_y \,, \tag{A.7a}$$

$$\partial_x \delta p = (\alpha - 1)\,\delta v_x \,, \tag{A.7b}$$

$$\partial_x v_x = -\partial_y \delta v_y \,, \tag{A.7c}$$

and in the passive fluid have the form:

$$\partial_y \delta p' = -\phi \delta v'_y \,, \tag{A.8a}$$

$$\partial_x \delta p' = -\phi \delta v'_x \,, \tag{A.8b}$$

$$\partial_x v'_x = -\partial_y \delta v'_y \,. \tag{A.8c}$$

Together with the ansatz of periodicity in x, this leads to analytically solvable, second-order differential equations for pressure in both fluids:

$$\frac{q^2}{1-\alpha}\delta p = \partial^2_{yy}\delta p \,, \tag{A.9a}$$

$$q^2 \delta p' = \partial^2_{yy}\delta p' \,. \tag{A.9b}$$

Like in the case of a growing circular droplet, pressure perturbation Eqs. (A.9a) are solved by linear combinations of 2 functions. Once again, only one of these functions in each case has a correct asymptotic behaviour (that is, it decays away from the interface, and does not diverge) and is retained. These retained functions are:

$$\delta p = c \exp\left(\frac{qy}{\sqrt{1-\alpha}}\right) \exp\left(iqx\right) , \tag{A.10a}$$

$$\delta p' = c' \exp\left(-qy\right) \exp\left(iqx\right) , \tag{A.10b}$$

implying (using Eq.(A.7a)) velocity perturbations of the form:

$$\delta v_y = -c \frac{q}{\sqrt{1-\alpha}} \exp\left(\frac{qy}{\sqrt{1-\alpha}}\right) \exp\left(iqx\right) , \tag{A.11a}$$

$$\delta v'_y = c' \frac{q}{\phi} \exp\left(-qy\right) \exp\left(iqx\right) . \tag{A.11b}$$

We use the velocity interfacial boundary conditions Eq. (A.3a):

$$-c\frac{q}{\sqrt{1-\alpha}}\exp\left(iqx\right) = c'\frac{q}{\phi}\exp\left(iqx\right) = \partial_t\delta h. \tag{A.12}$$

c and c' can now be presented explicitly:

$$c = -\frac{\partial_t\delta h\sqrt{1-\alpha}}{q\exp\left(iqx\right)}, \tag{A.13a}$$

$$c' = \frac{\phi\partial_t\delta h}{q\exp\left(iqx\right)}, \tag{A.13b}$$

and substituted to obtain a specific form of the pressure perturbation equations Eq. (A.10a):

$$\delta p = -\frac{\partial_t\delta h\sqrt{1-\alpha}}{q}\exp\left(\frac{qy}{\sqrt{1-\alpha}}\right), \tag{A.14a}$$

$$\delta p' = \frac{\phi\partial_t\delta h}{q}\exp\left(-qy\right). \tag{A.14b}$$

We now write the pressure interfacial boundary condition given by Eq. (A.3b):

$$p_0|_{y=h} + \delta p|_{y=h} + \frac{d^2h}{dy^2}|_{y=h} = p'_0|_{y=h} + \delta p'|_{y=h} \tag{A.15}$$

as (by substituting specific forms for p_0, p'_0, δp, $\delta p'$ to linear order in δh):

$$(\alpha-1)\delta h - \frac{\partial_t\delta h\sqrt{1-\alpha}}{q} - q^2\delta h = -\phi\delta h + \frac{\phi\partial_t\delta h}{q}. \tag{A.16}$$

Using the definition of σ_q from Eq. (A.6), we get:

$$\sigma_q = \frac{\alpha - 1 + \phi - q^2}{\phi + \sqrt{1-\alpha}}q. \tag{A.17}$$

In dimensional variables, this gives:

$$\sigma_q = \frac{\alpha - (\beta-\beta')\,v_i - \gamma q^2}{\beta' + \sqrt{\beta(\beta - \frac{\alpha}{v_i})}}q. \tag{A.18}$$

In the limit of a passive invading fluid $\alpha \to 0$, this reduces to the landmark result obtained by Saffman and Taylor [117]:

$$\sigma_q = \frac{-(\beta-\beta')\,v_i - \gamma q^2}{\beta' + \beta}q. \tag{A.19}$$

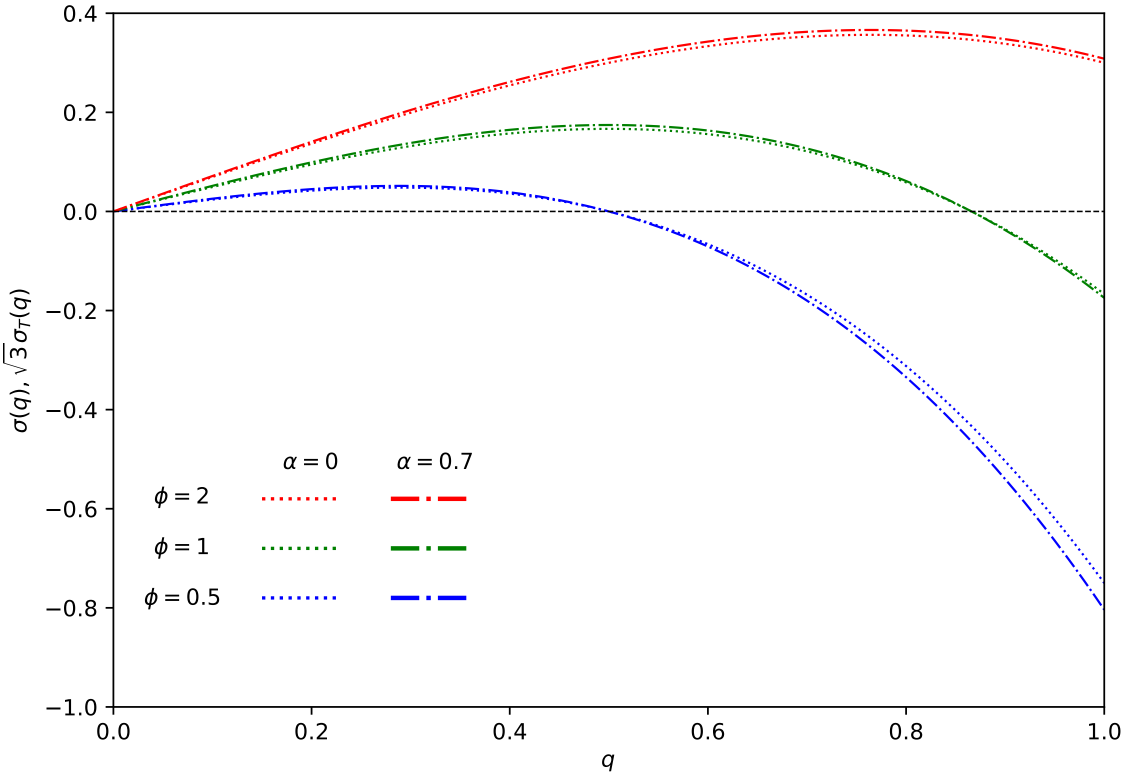

Fig. A.2 Growth rate $\sigma(q)$ of sinusoidal interfacial perturbations as a function of the wavenumber q, for a flat interface between an invading and displaced fluid in the system described in Sec. A.1 and Fig. (A.1). The invading fluid is passive ($\alpha = 0$; dashed lines) or active ($\alpha = 0.75$; solid lines), with varying ϕ. The active and passive fluids are described by Eqs. (A.1) and (A.2) respectively.

Fig. (A.2) presents $\sigma(q)$ vs. q for varying ϕ and α. $\sigma(q) > 0$ corresponds to unstable perturbations. Like in the case of a growing, circular droplet described in chapter 4, activity increases the tendency to form fingers for all values of σ. Unlike in the circular case, however, there is no characteristic size in the system which would influence the stability of the interface as the front progresses, unlike in the case of a circular droplet (see chapter 4 and Eq. (4.15) in particular).

A.2 Toner-Tu model

We now analyse the stability of the system presented in Fig. (A.2) when the invading fluid is described by the Toner-Tu model, instead of our fluid. First, let us remind the general form of the force balance equation according to Toner-Tu theory [108], already presented in

Chapter 2 (see Eq. (2.2) of that chapter for explanations of each of the terms):

$$\begin{aligned}\rho(\partial_t \mathbf{v} + \lambda_1(\mathbf{v}\cdot\nabla)\mathbf{v} + \lambda_2(\nabla\cdot\mathbf{v})\mathbf{v} + \lambda_3\nabla(|\mathbf{v}|^2)) = \\ = \alpha_T\mathbf{v} - \beta_T|\mathbf{v}|^2\mathbf{v} + \eta_1\nabla^2\mathbf{v} + \eta_2\nabla(\nabla\cdot\mathbf{v}) + \eta_3(\mathbf{v}\cdot\nabla)^2\mathbf{v} - \nabla p,\end{aligned} \tag{A.20}$$

where $\mathbf{v}$ is velocity, ρ is density, p is pressure.

There have been two studies investigating the stability of a free boundary of a Toner-Tu fluid flowing with no bulk pressure gradient [111, 112]. However, as far as we know, no study was performed so far which analyses viscous-like fingering between a Toner-Tu fluid and a passive fluid, flowing under an imposed pressure gradient. We perform this task here.

We neglect most of the terms of this equation. This is in analogy with the strategy of Saffman and Taylor in their landmark paper [117], and also of newer studies of viscous fingering, none of which implement full Navier-Stokes equations for the participating fluids [225, 60]. In all of these studies, the interfacial stability is studied while neglecting inertial terms and viscosity. Only Darcy Law terms ($\nabla p = -\beta\mathbf{v}$) are left in these studies, and they are sufficient to reproduce viscous fingering patterns. Their simplicity allows for an analytic solution to the problem.

In line with this approach, we leave out all terms with spatial derivatives of $\mathbf{v}$ on both the LHS and RHS of Eq. (A.20) and are left with:

$$\nabla p = \alpha_T\mathbf{v} - \beta_T|\mathbf{v}|^2\mathbf{v}, \tag{A.21a}$$

$$\nabla\cdot\mathbf{v} = 0, \tag{A.21b}$$

where we have supplemented Eq. (A.20) by the incompressibility condition. We now proceed to investigate the linear stability of an interface between such an active fluid and a passive fluid in the set-up described by Fig. (A.1). For consistency, we represent the friction term in the passive fluid as $-\beta_T'|\mathbf{v}'|^2\mathbf{v}'$ (if we chose to represent it as in the Darcy Law as $-\beta'\mathbf{v}'$, it would imply a difference in functional form of friction between the active and passive fluid). Equations of motion for the passive fluid are therefore:

$$\nabla p' = -\beta_T'|\mathbf{v}'|^2\mathbf{v}', \tag{A.22a}$$

$$\nabla\cdot\mathbf{v}' = 0. \tag{A.22b}$$

We solve the problem in a yet new system of dimensionless variables, in which they are re-scaled by a characteristic length $\ell = \sqrt{\frac{\gamma}{\beta_T v_i^3}}$, with v_i the velocity of the interface. Times are again rescaled by the reference time $t_r = \frac{\ell}{v_i}$, again implying the velocity of the moving interface equal to 1 in this system of variables. The viscosity ratio of the active and displaced fluid $\phi_T = \beta_T'/\beta_T$ is used again. Activity is made dimensionless using a reference activity, defined as $\alpha_T^* = \beta_T v_i^2$ and pressure using a reference pressure $p^* = l\beta_T v_i^3$. We ultimately obtain the current form of dimensionless equations of motion:

$$\nabla p = \alpha_T \mathbf{v} - |\mathbf{v}|^2 \mathbf{v}\,, \tag{A.23a}$$

$$\nabla \cdot \mathbf{v} = 0\,, \tag{A.23b}$$

for the active fluid and:

$$\nabla p' = -\phi_T |\mathbf{v}'|^2 \mathbf{v}'\,, \tag{A.24a}$$

$$\nabla \cdot \mathbf{v}' = 0\,, \tag{A.24b}$$

for the passive fluid.

The unperturbed solution to the hydrodynamic fields is identical as for our model in this set-up (Eqs. (A.4)):

$$\mathbf{v}_0 = (0,1)\,, \qquad p_0 = (\alpha_T - 1)y + p_0|_{y=0}\,, \tag{A.25a}$$

$$\mathbf{v}_0' = (0,1)\,, \qquad p_0' = -\phi_T y + p_0|_{y=0}\,. \tag{A.25b}$$

Perturbations in Euclidean coordinates in the active fluid now satisfy the following equations to linear order (see Eq. (C.4) in Appendix C for a general form of these perturbations and a discussion of its implications):

$$\partial_y \delta p = (\alpha_T - 3)\,\delta v_y\,, \tag{A.26a}$$

$$\partial_x \delta p = (\alpha_T - 1)\,\delta v_x\,, \tag{A.26b}$$

$$\partial_x \delta v_x = -\partial_y \delta v_y\,, \tag{A.26c}$$

and in the passive fluid have the form:

$$\partial_y \delta p' = -3\phi_T \delta v_y'\,, \tag{A.27a}$$

$$\partial_x \delta p' = -\phi_T \delta v_x'\,, \tag{A.27b}$$

$$\partial_x \delta v_x' = -\partial_y \delta v_y'\,. \tag{A.27c}$$

The ansatz of periodicity in x as given by Eq. (A.5) leads to:

$$q^2 \frac{\alpha_T - 3}{\alpha_T - 1} \delta p = \partial^2_{yy} \delta p \,, \tag{A.28a}$$

$$q^2 \delta p' = 3 \partial^2_{yy} \delta p' \,, \tag{A.28b}$$

and the functions with the correct asymptotic behaviour which solve these equations are respectively:

$$\delta p = c_T \exp\left(\sqrt{\frac{3-\alpha_T}{1-\alpha_T}} qy\right) \exp\left(iqx\right), \tag{A.29a}$$

$$\delta p' = c' \exp\left(-\sqrt{3} qy\right) \exp\left(iqx\right), \tag{A.29b}$$

which, using Eqs. (A.26a) and (A.27a), leads to velocity perturbations of the form:

$$\delta v_y = -c_T \frac{q}{\sqrt{(3-\alpha_T)(1-\alpha_T)}} \exp\left(\sqrt{\frac{3-\alpha_T}{1-\alpha_T}} qy\right) \exp\left(iqx\right), \tag{A.30a}$$

$$\delta v'_y = c'_T \frac{q}{\sqrt{3}\phi_T} \exp\left(-\sqrt{3} qy\right) \exp\left(iqx\right). \tag{A.30b}$$

We use the velocity interfacial boundary condition as in Eq. (A.3a) to linear order in δh:

$$-c_T \frac{q}{\sqrt{(3-\alpha_T)(1-\alpha_T)}} \exp\left(iqx\right) = c'_T \frac{q}{\sqrt{3}\phi_T} \exp\left(iqx\right) = \partial_t \delta h \,. \tag{A.31}$$

Therefore c_T and c'_T are:

$$c_T = -\frac{\partial_t \delta h \sqrt{(3-\alpha_T)(1-\alpha_T)}}{q \exp\left(iqx\right)} \,, \tag{A.32a}$$

$$c'_T = \frac{\sqrt{3}\phi_T \partial_t \delta h}{q \exp\left(iqx\right)} \,, \tag{A.32b}$$

and we obtain an exact form of pressure perturbation equations Eq. (A.33a):

$$\delta p = -\frac{\partial_t \delta h \sqrt{(3-\alpha_T)(1-\alpha_T)}}{q} \exp\left(\sqrt{\frac{3-\alpha_T}{1-\alpha_T}} qy\right), \tag{A.33a}$$

$$\delta p' = \frac{\sqrt{3}\phi_T \partial_t \delta h}{q} \exp\left(-\sqrt{3} qy\right). \tag{A.33b}$$

The pressure interfacial boundary condition given by Eq. (A.3b) is again split into zero-order components and perturbations:

$$p_0|_{y=h} + \delta p|_{y=h} + \frac{d^2h}{dy^2}|_{y=h} = p_0'|_{y=h} + \delta p'|_{y=h}, \tag{A.34}$$

to obtain the following up to linear order in δh:

$$(\alpha_T - 1)\delta h - \frac{\partial_t \delta h \sqrt{(3-\alpha_T)(1-\alpha_T)}}{q} - q^2 \delta h = -\phi_T \delta h + \frac{\sqrt{3}\phi_T \partial_t \delta h}{q}. \tag{A.35}$$

We obtain $\sigma(q)$ defined as in Eq. (A.6):

$$\sigma_T(q) = \frac{\alpha_T - 1 + \phi_T - q^2}{\sqrt{3}\phi_T + \sqrt{(3-\alpha_T)(1-\alpha_T)}} q. \tag{A.36}$$

The growth rates $\sigma(q)$, $\sigma_T(q)$ are very similar in both models. A quick inspection of Eqs. (A.17, A.36) shows that if $\alpha = 0$, $\alpha_T = 0$ and $\phi = \phi_T$, $\sqrt{3}\sigma_T(q) = \sigma(q)$. Positive levels of α, α_T modify this relationship, but Fig. (A.3) shows the modification is very slight even for relatively high α, α_T. For example, in Fig. (A.3) both activities are equal to 0.75 of the threshold for crossover into the high activity regime (defined and discussed in subsection 4.2.3), which is 1 in these systems of variables, and the relationship still approximately holds. The scaling factor of $\sqrt{3}$ results from the friction growing faster with velocity in the Toner-Tu fluid, which slows down the growth of perturbations.

Apart from the re-scaling of the growth rate by a factor $\sqrt{3}$, effects of activity on the emergence of interfacial instabilities are virtually identical in both examined fluids. In the rest of this PhD thesis, we focus on our own model because of advantages described in section 3.1. However, this appendix demonstrates that if the active tissue were to be described by the simplified Toner-Tu model (Eqs. A.21) in any of the systems studied in Chapter 4 or Appendix B, similar behaviour as reported in this thesis would be expected.

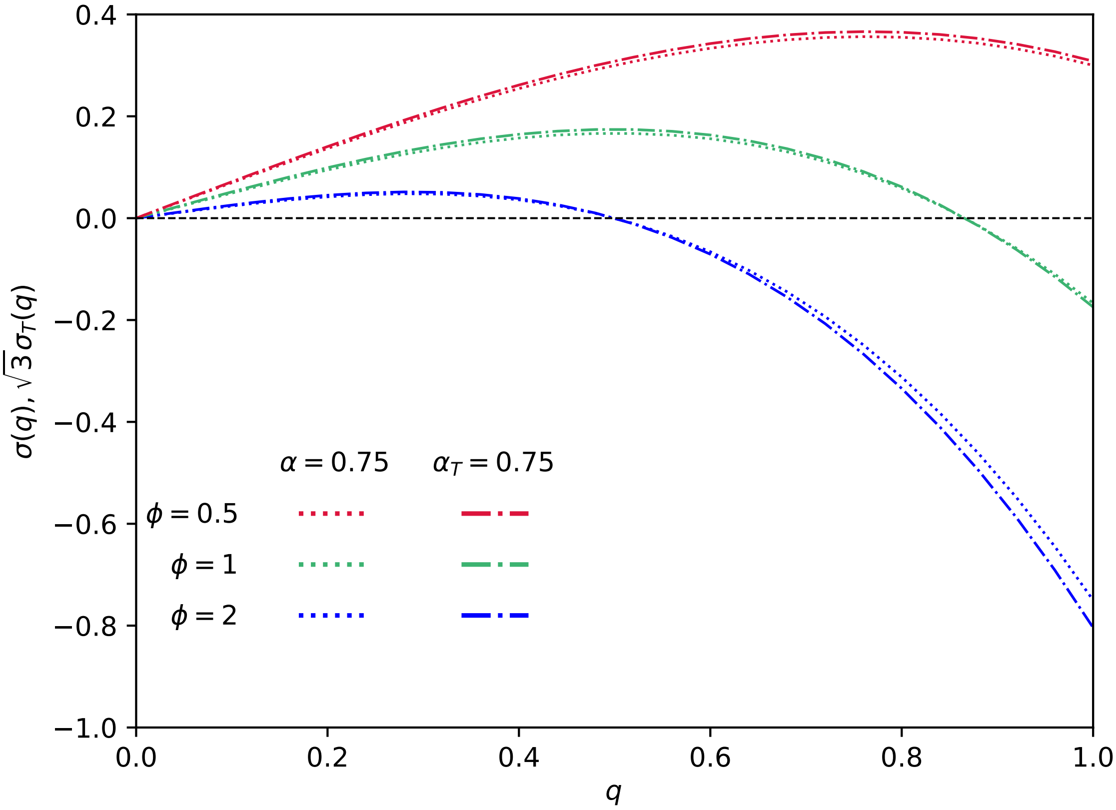

Fig. A.3 Comparison of linear growth rates $\sigma(q)$, $\sigma_T(q)$ as a function of the wavenumber q, as given by Eqs. (A.17, A.36) in a rectangular geometry in the set-up described in appendix A, obtained by solving our model and the simplified Toner-Tu model (Eqs. A.21). Results describe an active ($\alpha = 0.75$; solid lines) fluid, with varying ϕ. Note $\sigma_T(q)$ on the $y-$axis is re-scaled by a factor of $\sqrt{3}$.

Appendix B

Fingering in alternative set-ups

This appendix describes linear stability to interfacial perturbations of two physically or biologically justified 2-fluid systems, in which one of the fluids is active (as described by our model in Eqs. (3.1)) and the other is passive (as described by Eqs (4.1)). The fact that Eqs. (3.1)) can be exactly solved analytically for a large group of systems constitutes an important strength of our model of an active fluid. Appendix C reflects on why this is the case.

B.1 A rectangular stripe with growth

In this section, we deal with interfacial fingering in the set-up described in Fig. (B.1). As in section A.1, there is a droplet of a growing, active fluid governed by Eqs. (3.1), displacing a passive fluid, governed by Eqs. (4.1). However, this time, the droplet of the invading fluid is rectangular. It is constrained by non-moving, rigid barriers on three sides. The fourth side forms an interface with the passive fluid, whose linear stability we have investigated.

The interfacial boundary conditions used are as in section A.1. As also in section A.1, the channel is assumed as wide enough so that boundary conditions on the side walls can be effectively ignored. Similarly, the rear wall of the tissue is assumed sufficiently far from the interface compared to the wavelength of perturbations that it can be neglected in their dynamics (this approximation facilitates comparison with the landmark results on rectangular viscous fingering by Saffman and Taylor [117], as they assume an infinitely long channel in which the instability takes place).

We use the same system of variables as for the circular droplet in section 4. Instead of the radius r_0, as for the circular droplet, the result now depends on the unperturbed depth of the

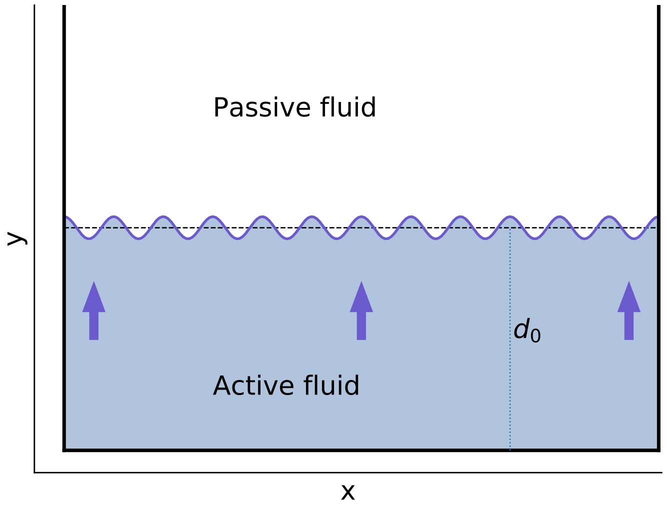

Fig. B.1 System described in this section: a 2D rectangular stripe of an active fluid, constrained by barriers on three sides, is described by Eqs. (3.1). It is growing and displacing a passive fluid modelled by Eqs. (4.1). The interface undergoes periodic perturbations whose linear stability analysis results are presented in the te.

rectangular stripe d_0 (see Fig. (B.1)). The linear growth rate is derived as in sections A.1 and 4.2 and equals:

$$\sigma_q(d_0) = \frac{[(\phi-1)\,d_0+\alpha]\,q-\frac{q^3}{2}+\Upsilon}{\phi+\Upsilon}, \tag{B.1}$$

where

$$1/\Upsilon = 1-q\alpha\frac{U\left[1-\frac{q\alpha}{2},1,2q\,(\alpha-d_0)\right]}{U\left[-\frac{q\alpha}{2},0,2q\,(\alpha-d_0)\right]},$$

and $U\,[a,b,z]$ is the Tricomi confluent hypergeometric function. Note $\Upsilon_{\alpha\to 0}=1$. Therefore, in the passive limit $\alpha=0$, $\sigma_q\,(d_0)$ becomes:

$$\sigma_q\,(d_0) = \frac{(\phi-1)d_0q-\frac{q^3}{2}}{\phi+1}+\frac{1}{\phi+1}. \tag{B.2}$$

Here the first term is equivalent to Saffman and Taylor's landmark result [117] (when noting the velocity of the interface $v_i = kd_0$), while the second term $1/(\phi+1)$, as in the case of a circular droplet, is responsible for the growth of the tissue within the fingers themselves. Since Υ has an inverse relationship with α, $\sigma_q\,(d_0)$ again monotonically grows and stability of the system decreases with increasing α and other parameters fixed.

B.2 A circular droplet with injection in the middle

In this section we provide results of linear stability analysis for an interface between a circular, active droplet surrounded by a passive fluid, as in chapter 4 and Fig. (4.1), **but** with the crucial difference that the active fluid is now injected in the middle of the droplet. There is no growth through the rest of the active fluid, unlike in chapter 4. The injection rate in the middle of the droplet (defined in terms of area covered per time) has magnitude m. This system is included here, as it is a direct implementation of activity in Paterson's original radial viscous fingering experiment set-up [60].

The dimensionless system of variables are build this time around the injection rate m.

The characteristic length is $\ell = \frac{2\pi\gamma}{\beta m}$, the characteristic time is $\tau = \frac{\rho^2\pi}{m}$, the reference activity is $\alpha^* = \frac{\beta\rho}{\tau}$. The meaning of $\phi = \frac{\beta'}{\beta}$ and r_0 is retained from chapter 4. The dispersion relation is now:

$$\sigma_n(r_0) = \frac{\left[\frac{\phi-1}{2r_0^2} + \frac{1-n^2}{2r_0^3}\right] n + \frac{\alpha}{r_0} n}{\phi + \Lambda_{2,n}(2\alpha r_0)} - \frac{1}{2r_0^2}, \tag{B.3}$$

where

$$\Lambda_{2,n}(x) = \frac{\sum_{j=0}^{\infty} \frac{\binom{n+j-1}{n-1}^2}{\binom{2n+j}{2n}} x^j}{\sum_{j=0}^{\infty} \frac{\binom{n+j}{n}^2}{\binom{2n+j+1}{2n+1}} x^j}. \tag{B.4}$$

In the passive limit $\alpha = 0$, $\Lambda_{2,n}(x) = 1$ and upon re-substitution of dimensional variables, one directly reproduces Paterson's landmark result (Eq. (10) of reference [60], mind the different notation and system of variables in his paper):

$$\sigma_n(r_0) = \frac{m(\beta' - \beta)}{2\pi r_0^2(\beta' + \beta)} n - \frac{\gamma n(n^2 - 1)}{r_0^3(\beta' + \beta)} - \frac{m}{2\pi r_0^2}, \tag{B.5}$$

since $\Lambda_{2,n}(x)$ monotonically decreases with increasing α, $\sigma_n(r_0)$ again increases with α and other variables fixed.

Appendix C

Analytical solvability of fingering in our and the Toner-Tu model

This appendix briefly discusses the basic reason for the fact that our model is analytically solvable in many biologically and physically relevant set-ups (see chapter 4 and appendix B). It then explains why replacing our expression for the force on the fluid from the substrate $\alpha \frac{\mathbf{v}}{|\mathbf{v}|} - \beta \mathbf{v}$ with the similar Toner-Tu expression $\alpha_T \mathbf{v} - \beta_T |\mathbf{v}|^2 \mathbf{v}$ would make these systems analytically unsolvable in most cases. Note that qualitatively the predictions of both models are very similar in the systems in which they can be both solved analytically (as appendix A demonstrates).

The evolutions of the pressure $p(\mathbf{r},t)$ and velocity $\mathbf{v}(\mathbf{r},t)$ fields in our model are governed by Eq. (3.1). When k is constant through space, linear perturbations $(\delta p, \delta \mathbf{v})$ around any unperturbed solution $\mathbf{v}_0$, p_0, apart from the cases when $|\mathbf{v}_0| = 0$ and $|\mathbf{v}_0| = \frac{\alpha}{\beta}$, satisfy the following equations:

$$\nabla \delta p = -\beta \delta \mathbf{v} + \alpha \frac{\delta v_\perp}{\mathbf{v}_0}, \tag{C.1a}$$

$$\nabla \cdot \delta \mathbf{v} = 0, \tag{C.1b}$$

where $\delta v_\perp$ is the component of $\delta \mathbf{v}$ locally perpendicular to $\mathbf{v}_0$. More specific forms of these equations (in dimensionless systems of variables) are provided in chapter 4 and appendix A for specific systems (Eqs. (4.10) and (A.7)). Writing these equations in terms of components and using ansatz of periodicity (see Eq. (4.8) for a circular system, and Eq. (A.5) for a rectangular one) one obtains second-order differential equations for δp.

These equations in general take the following form for rectangular systems (note we choose the system of variables so that the unperturbed fluid flows locally along the y direction with magnitude of velocity $|\mathbf{v}_0|$):

$$q^2 \delta p = \left(1 - \frac{\alpha}{\beta|\mathbf{v}_0|}\right) \partial^2_{yy} \delta p \,, \tag{C.2}$$

and for circular systems (in which unperturbed flow is purely radial):

$$n^2 \delta p = \left(1 - \frac{\alpha}{\beta|\mathbf{v}_0|}\right) \rho \partial_\rho (\rho \partial_\rho \delta p) \,. \tag{C.3}$$

Only if they are analytically solvable, can the linear stability analysis itself be conducted analytically, along the lines of reasoning presented in section 4.2.

Fortunately, these equations indeed are solvable analytically for several realistic cases. This includes the case of uniform growth across a circular droplet or rectangular stripe (see chapter 4 and appendix B respectively) since then $|\mathbf{v}_0| \propto \rho, y$ respectively. A circular system in which the active fluid is injected into the middle of the droplet (Appendix B) is also solvable, since in this case $|\mathbf{v}_0| \propto \frac{1}{\rho}$, as well as any system in which $|\mathbf{v}_0| = constant$.

If we use the Toner-Tu expression for the force from the substrate, instead of Eq. (C.1), we obtain the following equations for perturbations to linear order:

$$\nabla \delta p = \alpha_T \delta \mathbf{v} - \beta_T \left(|\mathbf{v}_0|^2 \delta \mathbf{v} + 2|\delta v_{||}||\mathbf{v}|\mathbf{v}\right) \,, \tag{C.4a}$$

$$\nabla \cdot \delta \mathbf{v} = 0 \,, \tag{C.4b}$$

where $\delta v_{||}$ is the component of $\delta \mathbf{v}$ parallel to the unperturbed flow. In general, under the periodicity ansatz (A.5), this leads to the following second-order equation for pressure in a rectangular system:

$$\partial^2_{yy} \delta p = \frac{\partial_y \left(\alpha_T - 3\beta_T |\mathbf{v}_0|^2\right)}{\alpha_T - \beta_T |\mathbf{v}_0|^2} \partial_y \delta p + q^2 \frac{\alpha_T - 3\beta_T |\mathbf{v}_0|^2}{\alpha_T - \beta_T |\mathbf{v}_0|^2} \delta p \,, \tag{C.5a}$$

and to an even more complicated equation for a circular system.

To the best of our knowledge, these equations are not solvable analytically for any of the set-ups which we deal with analytically in our own model, except if $\mathbf{v}_0$ is constant through the space (appendix A). Therefore, linear stability analysis of the interface, which relies on first determining the functional forms of δp and $\delta p'$, cannot be conducted analytically. Therefore, our model has an important practical advantage over applying the Toner-Tu expression for substrate-active fluid interaction.

Appendix D

Linear stability analysis in unbounded space

Linear stability analysis of the active fluid's interface, as outlined in chapter 4, assumes the fluid on its own has a stable division-induced flow profile, as described by Eqs. (4.7a). If that profile itself is unstable, the procedure of the linear stability analysis of interfacial fingering along the lines described in section 4.2 cannot be carried out. In this appendix, we formally show that the uniform flow of an active fluid cannot be stable when its magnitude of velocity is lower than $|\mathbf{v}| = \frac{\alpha}{\beta}$.

For this purpose, we analytically investigate the flow of the active fluid in infinite space, at a given constant velocity $\mathbf{v}_0 = (0, v_0)$ (and therefore zero cell division rate k) to see under what conditions this flow is stable. Our derivation follows here a procedure described for a Toner-Tu-like fluid in [48] and proceeds along the following steps:

1. We search for steady-state, uniform velocity solutions of the following EOMs:

$$\tau\left(\frac{d\mathbf{v}}{dt} + \mathbf{v}\cdot\nabla\mathbf{v}\right) = -\beta\mathbf{v} + \alpha\frac{\mathbf{v}}{|\mathbf{v}|} - \nabla p\,, \tag{D.1a}$$

$$\nabla\cdot\mathbf{v} = 0\,. \tag{D.1b}$$

   Note the RHS of Eq. (D.1a) consists of all forces acting on the active fluid as in Eq. (3.1a), while the LHS consists of effective inertial terms, allowing the system to move away from a given solution. τ, related to the effective decay time, has the dimension of density. In general, in active fluids, since Galilean invariance is not present, the $\mathbf{v}\cdot\nabla\mathbf{v}$ term can have a prefactor $\neq 1$, as in [48, 112]. However, this would correspond to additional, active hydrodynamic interactions between the fluid particles as present in puller- or pusher-type swimmers [48]. We do not intend to investigate such interactions here and limit ourselves to active interactions between the fluid and the substrate, captured on the RHS. In any case, manipulating this prefactor would not qualitatively change the results of the present analysis, as we separately verified.

The uniform, steady-state velocity solution to Eqs. (D.1) is the following system:

$$p_0 = p_i + (\alpha - \beta v_0)\, y\,, \tag{D.2a}$$

$$\mathbf{v}_0 = (0, v_0)\,, \tag{D.2b}$$

where p_i is the pressure at $y = 0$. Note that the y axis being along the direction of $\mathbf{v}_0$ is a choice made for convenience, which does not imply a loss of generality of the reasoning. Similarly, defining $v_0 > 0$ upholds this generality, as we can always set the numbers of the y axis growing along the uniform flow.

2. We substitute perturbations of p and $\mathbf{v}$ around the steady-state solution given by Eq. (D.2) and find Equations of Motion (EOMs) of the perturbations δp, $\delta\mathbf{v}$ to linear order (the result below is correct for $v_0 \neq 0$):

$$\tau\left[\frac{d\delta\mathbf{v}}{dt} + (\delta\mathbf{v}\cdot\nabla)\,\mathbf{v}_0 + (\mathbf{v}_0\cdot\nabla)\,\delta\mathbf{v}\right] = \frac{\alpha}{v_0}\delta\mathbf{v}_x - \beta\delta\mathbf{v} - \nabla\delta p\,, \tag{D.3a}$$

$$\nabla\delta\mathbf{v} = 0\,, \tag{D.3b}$$

where $\delta\mathbf{v}_x$ is the projection of the velocity perturbation on the direction perpendicular to the unperturbed velocity of the fluid $\mathbf{v}_0$.

3. We introduce the following ansatz for the form of pressure and velocity perturbations: $(\delta p, \delta\mathbf{v}) \propto e^{\sigma t + i\mathbf{q}\cdot\mathbf{x}}$, and we need to determine when $\sigma > 0$, implying a linearly unstable system.

4. We write EOMs for the perturbations in Fourier space to linear order:

$$\tau\left(\sigma\delta\mathbf{v}+iv_0q_y\delta\mathbf{v}\right)=\left(\frac{\alpha}{v_0}-\beta\right)\delta\mathbf{v}-\frac{\alpha}{v_0}\delta\mathbf{v}_y-i\delta p\mathbf{q}\,, \tag{D.4a}$$

$$\mathbf{q}\cdot\delta\mathbf{v}=0\,, \tag{D.4b}$$

where $\delta\mathbf{v}_y$ is the projection of the velocity perturbation on the direction parallel to the unperturbed velocity of the fluid $\mathbf{v}_0$, and q_y is the component of the wavevector in that direction.

5. We manipulate Eq. (D.4a) to obtain a linear matrix equation for σ of the form $\sigma\delta\mathbf{v}=A\delta\mathbf{v}+b$. Note that, since the space of perturbations has 2 independent dimensions, σ is a 2 by 2 matrix; its eigenvalues provide the actual growth rates:

$$\sigma\delta\mathbf{v}=-iv_0q_y\delta\mathbf{v}+\frac{1}{\tau}\left(\frac{\alpha}{v_0}-\beta\right)\delta\mathbf{v}-\frac{\alpha}{v_0\tau}\delta\mathbf{v}_y-i\frac{\delta p}{\tau}\mathbf{q}\,. \tag{D.5}$$

6. We define $\mathbf{P_y}$ as the projector on the normalised vector tangent to the y axis:

$$\mathbf{P_y}=\begin{pmatrix}0&0\\0&1\end{pmatrix}\,.$$

We also define $\mathbf{M}=c_1\mathbf{I}+c_2\mathbf{P_y}$, where $c_1=iv_0q_y-\frac{1}{\tau}\left(\frac{\alpha}{v_0}-\beta\right)$, $c_2=\frac{\alpha}{v_0\tau}$. This allows for a more concise presentation of Eq. (D.5):

$$\sigma\delta\mathbf{v}=-\mathbf{M}\delta\mathbf{v}-\frac{i\delta p}{\tau}\mathbf{q} \tag{D.6}$$

7. We present δp in terms of δv by multiplying Eq. (D.6) by $-\mathbf{q}$ and using Eq. (D.4b). This leads to:

$$0=\mathbf{q}\cdot\mathbf{M}\delta\mathbf{v}+\frac{i|\mathbf{q}|^2}{\tau}\delta p\,. \tag{D.7}$$

8. We substitute δp from Eq. (D.7) to Eq. (D.6) to obtain:

$$\sigma\delta\mathbf{v}=-\mathbf{M}\delta\mathbf{v}+\frac{\mathbf{q}\cdot(\mathbf{M}\delta\mathbf{v})}{|\mathbf{q}|^2}\mathbf{q}\,. \tag{D.8}$$

9. We note the projector on an orthogonal vector to $\mathbf{q}$ is defined by:

$$\mathbf{P}_{\perp\mathbf{q}}\mathbf{v} \equiv \mathbf{v} - \frac{\mathbf{q}\cdot\mathbf{v}}{|\mathbf{q}|^2}\mathbf{q}\,. \tag{D.9}$$

and use it to write:

$$\sigma\mathbf{v} = -\mathbf{P}_{\perp\mathbf{q}}\mathbf{M}\mathbf{v}. \tag{D.10}$$

10. We find the eigenvalues of $-\mathbf{P}_{\perp\mathbf{k}}\mathbf{M}$ and, therefore, the growth rates of perturbation eigenvectors σ:

$$\sigma(\mathbf{q}) \in \left\{0, -c_2\frac{q_y^2}{|\mathbf{q}|^2} - c_1\right\} = \left\{0, -\frac{\alpha}{v_0\tau}\frac{q_y^2}{|\mathbf{q}|^2} - iq_y v_0 + \frac{1}{\tau}\left(\frac{\alpha}{v_0} - \beta\right)\right\}. \tag{D.11}$$

In conclusion, the system can have two types of perturbations: (1) exponentially growing or decaying perturbations and (2) so-called massless Goldstone perturbations, corresponding to $\sigma(\mathbf{k}) = 0$.

Goldstone modes result from the angular degeneracy of the lowest energy state and are simply a manifestation of the fact that changing the direction of the velocity of the entire system can in principle occur at no energetic expense. This is said[1] to facilitate the formation of local vortices and swirls in the flowing fluid (it must be noted that such vortices, triggered by cell division, are observed in flowing and still epithelial layers [15, 16], as well as in bacterial suspensions and other flocks). To our knowledge, there are no quantitative studies on this effect.

Crucially, the real part of the second eigenvalue of σ is:

$$Re\left[\sigma_2(\mathbf{k})\right] = -\frac{\alpha}{v_0\tau}\frac{q_y^2}{|\mathbf{q}|^2} - \frac{1}{\tau}\left(\beta - \frac{\alpha}{v_0}\right). \tag{D.12}$$

We note that it is negative, implying a stable flow, if $\alpha \leq \beta v_0$. On the contrary, it is positive if $\alpha > \beta v_0$. This implies the main conclusion of this appendix: a stable, uniform flow in the high-activity regime is impossible.

As a sidenote, it might be worth noting that, theoretically, Eq. (D.12) implies all wavelengths (even infinitesimally short) in the x direction are unstable in the high-activity regime.

---

[1] Based on an exchange of e-mails with prof. Jorn Dunkel, MIT

This is not physical and stems from the fact that viscosity is neglected in our model. The presence of even very small viscosity stabilizes very short wavelengths.

Appendix E

Scaling laws for the dominant modes

E.1 Exponential growth

We obtain the scaling of Eq. (4.20a) for the viscosity-controlled fingering, $\phi > 1$, by only considering the passive case ($\alpha = 0$). The result is valid even when $\alpha > 0$, since effects of the viscosity mismatch dominate effects of activity when $r_0 \to \infty$, as also indicated by the numerical results shown in Fig. 4.4. We then use the expression $\sigma_n(r_0)|_{\alpha=0}$ given by Eq. (4.17) into Eq. (4.18), in which we substitute $\mathrm{d}t = 2\mathrm{d}r/r$ for exponential growth. We calculate

$$\zeta_n(r_0)|_{\alpha=0} = \left[A_n \exp(A_n^{-1} - 1)\right]^{B_n},$$

with $A_n = \frac{\phi-1}{n(n+1)} r_0^3$ and $B_n = \frac{(n-1)(\phi-1)}{3(\phi+1)}$, by using the expression of R_n obtained from solving $\sigma_n(R_n)|_{\alpha=0} = 0$. The dominant mode n_d is calculated for each r_0 from the conditions of Eqs. (4.19). Taking the limit $r_0 \to \infty$, and reintroducing dimensional variables, lead to Eq. (4.20a).

When $\phi = 1$, the selection of the dominant mode depends on the activity α. We first Taylor expand $\Lambda_n(x)$ to first order in x,

$$\Lambda_n(x) \approx \frac{2n(n-1)}{2n-1} x. \tag{E.1}$$

This term grows linearly with n for $n \to \infty$, while higher order coefficients in x plateau in this limit. Therefore, this expression of Λ_n is efficient even for $x \sim 1$, and we use it to approximate

$$R_n \approx \left[\frac{(n+1)(2n-1)}{4\alpha}\right]^{1/2}$$

and

$$\sigma_n(r_0) \approx \frac{n(n-1)}{4r_0^3}\Big[\frac{\alpha(n^2+n-4r_0^3)}{(2n-1)r_0} - n - 1\Big].$$

Upon substituting these approximations into Eq. (4.18), the dominant mode conditions Eqs. (4.19) lead to Eq. (4.20b) for $r_0 \to \infty$.

E.2 Linear growth

In this kinetics, the growth rate k is not a constant, as opposed to the velocity v_i of the unperturbed interface, which is now the adequate growth parameter. We thus use a different set of dimensionless variables, based on v_i. The characteristic length is now $\ell = \big(\frac{\gamma}{\beta v_i}\big)^{1/2}$, and times are rescaled by ℓ/v_i, activities by $\alpha^* = \beta v_i$, pressures by $p^* \equiv \beta \ell v_i$ and velocities by v_i. The derivation presented in section 4.2 proceeds similarly, and we find that the rate of perturbation's growth $\sigma_n(r_0)$ in this system of variables is:

$$\sigma_n(r_0) = \frac{1}{r_0}\frac{(\phi-1)(n-1) - n(n^2-1)/r_0^2 + \Lambda_n\big(\alpha\big)}{\phi + 1 + \Lambda_n\big(\alpha\big) - n\alpha}. \tag{E.2}$$

The integral of Eq. (4.18), with the change of variables now written $\mathrm{d}t = \mathrm{d}r$, may then be calculated analytically and we obtain:

$$\zeta_n(r_0) = \big[A_n \exp(A_n^{-1} - 1)\big]^{B_n}, \tag{E.3}$$

with

$$A_n = \frac{(\phi-1)(n-1) + \Lambda_n(\alpha)}{n(n^2-1)} r_0^2$$

and

$$B_n = \frac{1}{2}\frac{(\phi-1)(n-1) + \Lambda_n(\alpha)}{\phi + 1 + \Lambda_n(\alpha) - n\alpha}.$$

Upon using the approximation of $\Lambda_n(x)$ given by Eq. (E.1), the conditions Eqs. (4.19) now imply Eq. (4.21) in the limit $r_0 \to \infty$.

Appendix F

Derivation of Eq. (7.3)

For a single particle in an external potential, we start by writing the moving average of particle positions in Eq. (7.1), which represents data collected during a single shutter time, as the limit of a discrete series of $n+1$ successive positions taken by the particle every σ/n time units, added to a noise term:

$$\bar{\mathbf{r}}(t) = \lim_{n\to\infty} \frac{1}{n+1} \sum_{k=0}^{n} \mathbf{r}_k(t) + \xi \,. \tag{F.1}$$

Here $\mathbf{r}_k(t) = \mathbf{r}(t-\sigma+k\sigma/n)$, so that $\mathbf{r}_0(t) = \mathbf{r}(t-\sigma)$ and $\mathbf{r}_n(t) = \mathbf{r}(t)$. The particle is assumed to obey the inertialess (i.e., overdamped) limit of Langevin equation in an external potential. Consecutive positions in the series forming $\bar{\mathbf{r}}(t)$ are almost surely located infinitesimally close to each other when n is large. Therefore, the motion between them can be treated via the Brownian dynamics,

$$\mathbf{r}_k = \mathbf{r}_{k-1} - (\sigma/n)\,\beta D \nabla V\left(\mathbf{r}_{k-1}\right) + \sqrt{2D\sigma/n}\,\mathbf{w}\,, \tag{F.2}$$

where $\mathbf{w}$ is a vector realization of a delta-correlated, stationary Gaussian process with zero-mean. Hence, $f_{\mathbf{w}}(w) = \mathscr{N}(w;\mathbf{0},I)$ and the auto-correlation $\langle \mathbf{w}(t)\mathbf{w}^{\intercal}(t')\rangle = I$ if $|t-t'| \le \sigma/n$, $\mathbf{0}$ otherwise. We here employ the usual notation for the d-dimensional normal distribution with mean vector μ and covariance matrix Σ,

$$\mathscr{N}(r;\mu,\Sigma) = \frac{e^{-(r-\mu)^{\intercal}\Sigma^{-1}(r-\mu)/2}}{(2\pi)^{d/2}\det(\Sigma)^{1/2}}\,.$$

Each position $\mathbf{r}_k$ is now assumed to be in the vicinity of $\mathbf{r}_0$ so that we may linearize the force $\beta D\nabla V(r') = -v_0 + \Lambda_0(r' - r_0)$, where we have used the notations:

$$v_0 \equiv v|_{r=r_0},$$
$$\Lambda_0 \equiv \Lambda|_{r=r_0},$$

for v and Λ as defined by Eqs. (7.4) in subsection 7.2. The subscript "0" indicates that these are evaluated at r_0. The conditions for this second order expansion of V to be valid are given by Eqs. (7.6).

The conditional pdf $f_{\mathbf{r}|\mathbf{r}'}(r|r') = f_{\mathbf{r},\mathbf{r}'}(r,r')/f_{\mathbf{r}'}(r')$ is written in terms of the joint pdf $f_{\mathbf{r},\mathbf{r}'}$ and the marginal $f_{\mathbf{r}'}$. From Eq. (F.2) it follows that

$$f_{\mathbf{r}_k|\mathbf{r}_{k-1}}(r|r') = \mathcal{N}\left(r; A_n r' + b_n, 2D\sigma I/n\right),$$

with $A_n = I - \sigma\Lambda_0/n$ and $b_n = \sigma(v_0 + \Lambda_0 r_0)/n$. Recursively using

$$f_{\mathbf{r}_k|\mathbf{r}_{k-2}}(r|r') = \iiint f_{\mathbf{r}_k|\mathbf{r}_{k-1}}(r|\rho) f_{\mathbf{r}_{k-1}|\mathbf{r}_{k-2}}(\rho|r')\mathrm{d}^3\rho,$$

and exploiting properties of Gaussian integrals, we get, for any $k > j \geq 0$:

$$f_{\mathbf{r}_k|\mathbf{r}_j}(r|r') = \mathcal{N}\left(r; A_n^{k-j} r' + \sum_{i=0}^{k-j-1} A_n^i b_n, 2D\frac{\sigma}{n}\sum_{i=0}^{k-j-1} A_n^{2i}\right).$$

This equation allows us to calculate $f_{\mathbf{r}_k|\mathbf{r}_0}$ and $f_{\mathbf{r}_k,\mathbf{r}_j|\mathbf{r}_0} = f_{\mathbf{r}_k|\mathbf{r}_j} f_{\mathbf{r}_j|\mathbf{r}_0}$ for any $k > j \geq 1$. All are normal distributions, and so will be $f_{\bar{\mathbf{r}}|\mathbf{r}_0}$. Further using the matrix's geometric series $\sum_{j=0}^{k-1} A_n^j = (I - A_n)^{-1}(I - A_n^k)$, the matrix exponential limit, $\lim_{n\to\infty}(I - A/n)^n = e^{-A}$, and accounting for static errors by adding $E = \langle \xi\xi^\intercal \rangle$ to the covariance matrix of the measured position, we finally obtain

$$f_{\bar{\mathbf{r}}|\mathbf{r}_0}(r|r_0) = \mathcal{N}\left(r; r_0 + \frac{\sigma}{2} G_\sigma v_0, D\sigma H_\sigma + E\right),$$

where $G_\sigma = G(\sigma\Lambda_0)$ and $H_\sigma = H(\sigma\Lambda_0)$ with:

$$G(X) = 2X^{-2}\left(X - I + e^{-X}\right),$$
$$H(X) = 2X^{-2} - X^{-3}\left(3I - e^{-X}\right)\left(I - e^{-X}\right).$$

where

$$G^{\rho} = \left[\rho + \frac{\sigma}{2} G_{\sigma}\big(v - \Lambda\rho\big)\right].$$

The above Gaussian integral (with a linear term) can be calculated. After noting the relation $[I - XG(X)/2]^2 = G(X) - XH(X)$, we finally obtain:

$$f_{\bar{\mathbf{r}}} = \frac{f_0 e^{-\beta V}}{\det\big(G_{\sigma} + \frac{\Lambda E}{D}\big)^{1/2}} \exp\left\{ - \frac{v^{\mathsf{T}} \Lambda^{-1} \left[\big(G_{\sigma} + \frac{\Lambda E}{D}\big)^{-1} - I\right] v}{2D} \right\},$$

from which Eq. (7.3) can be readily deduced, upon defining $U_{E,\sigma} = (G_{\sigma} + \Lambda E/D)^{-1}$.

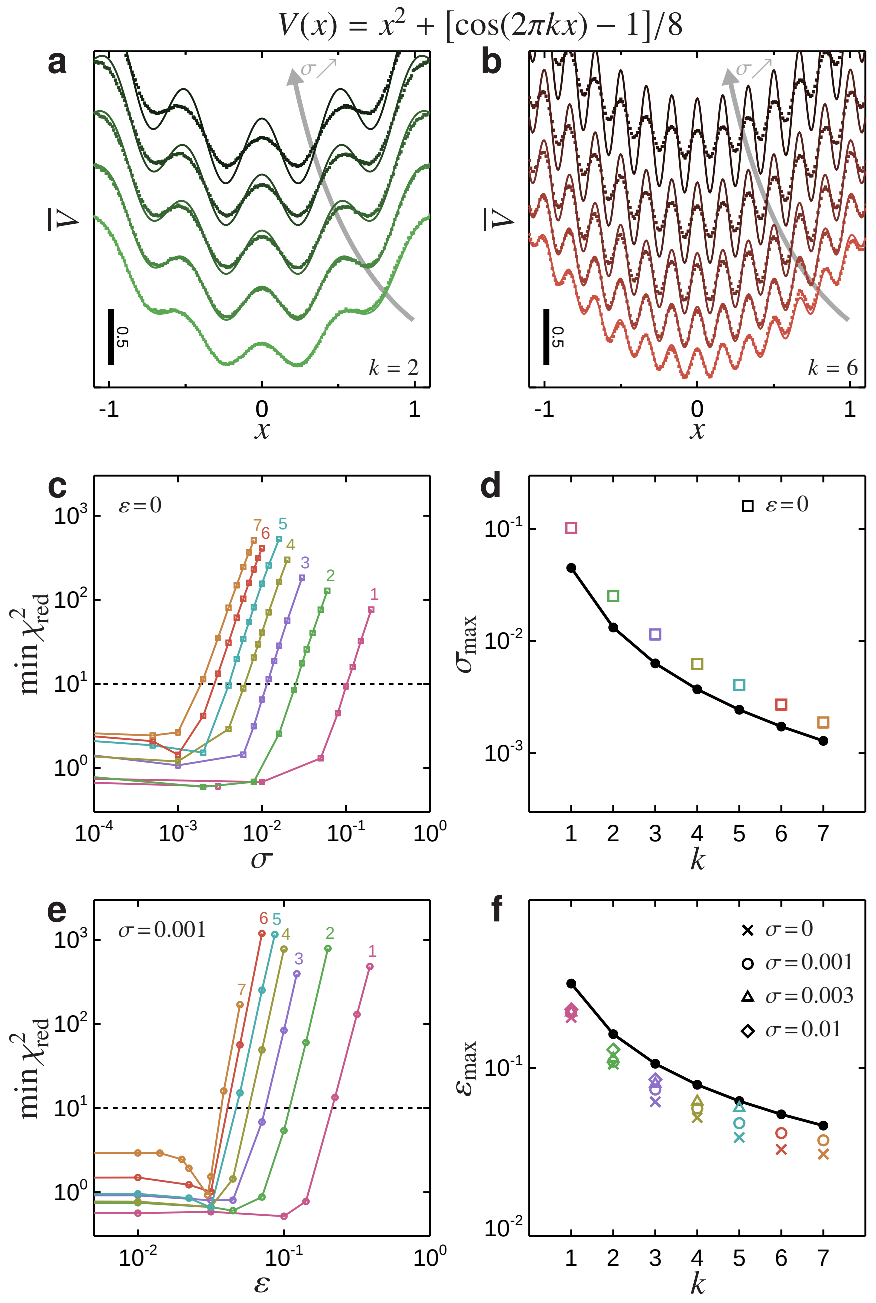

Fig. F.1 Assessing the conditions Eqs. (7.6) by quantitatively comparing Eq. (7.8) to BD simulations for the trapping potential $V(x) = x^2 + [\cos(2\pi kx) - 1]/8$, with $k = 1 \ldots 7$. Panels a and b show the simulated apparent potentials (symbols) and our approximated expression (lines) for increasing values of σ and with $\varepsilon = 0$ ($k = 2$ in panel a, $k = 6$ in b). The discrepancy is quantified by $\min \chi^2_{\text{red}}$, defined in Eq. (G.2), whose variations with σ and k are shown in panel c (values of k displayed on each corresponding line). Panel d shows the range $\sigma_{\max}$ (below which Eq. (7.8) is effective) as a function of k, as defined by the threshold $\min \chi^2_{\text{red}} = 10$ (symbols), and as obtained by Eq. (7.11a) (black line, see text). Panels e and f give the same quantities as panel c and d, respectively, to compare the range of static error $\varepsilon_{\max}$ evaluated from $\min \chi^2_{\text{red}} = 10$ and (7.11b), for the displayed values of $\sigma < \sigma_{\max}$.

Appendix G

Conditions of validity

We here assess the ranges of σ and ε for which Eq. (7.3) can be used. The examples investigated in the main text suggest that the conditions of validity Eqs. (7.6) provide appropriate estimates for the maximum values σ_{max} and ε_{max} below which Eq. (7.3) can indeed be used. To assess these limiting values in a systematic manner, we simulated a Brownian particle trapped in the potential $V(x) = x^2 + [\cos(2\pi kx) - 1]/8$, for $k = 1 \ldots 7$, with increasing values of σ and of ε. Increasing k for this potential increases the level of details that needs to be resolved by the particle tracking methods (compare Fig. 4.5a, where $k = 2$, with Fig. 4.5b where $k = 6$). For this potential, we test our predictions for σ_{max} and ε_{max} obtained by equating both sides in each Eq. (7.11a) and Eq. (7.11b),

$$(2 + \pi k/4)\sigma_{\text{max}} + \sigma_{\text{max}}^{1/2} = (\pi k)^{-1}\,, \tag{G.1a}$$

$$\varepsilon_{\text{max}} = (\pi k)^{-1}\,, \tag{G.1b}$$

respectively. The amplitude $1/8$ of the oscillations around the term x^2 in the potential is such that no term may be neglected in Eqs. (G.1).

The simulation results (symbols in Fig. 4.5a and 4.5b) are then compared to the apparent potential $\overline{V}$ predicted by Eq. (7.8) (lines in Fig. 4.5a and 4.5b). Specifically, the discrepancy between the simulations and Eq. (7.8) is quantified by the reduced chi-squared χ^2_{red}, defined as

$$\chi^2_{\text{red}} = \frac{1}{N}\sum_{j=1}^{N} \frac{\Delta\overline{V}_j^2}{\text{var}\overline{V}_j}\,. \tag{G.2}$$

Here, $\{\Delta\overline{V}_j\}_{j=1\ldots N}$ are the differences between the simulations and Eq. (7.8) at the N locations output by the simulations, and $\{\text{var}\overline{V}_j\}_{j=1\ldots N}$ are the variances of the simulated data at these locations. The arbitrary constant in Eq. (7.2) is chosen beforehand to minimize χ^2_{red}, so that we choose $\min\chi^2_{\text{red}}$ as our measure of deviation of Eq. (7.8) from the simulations.

As σ increases, the approximation fails above a value $\sigma_{\max}$ that is determined by $\min \chi^2_{\text{red}} = 10$, as indicated in Fig. 4.5c [226]. The results for $\sigma_{\max}$ are compared favorably to the solution of Eq. (G.1a), shown by the black line in Fig. 4.5c for various values of k. The same procedure is applied to evaluate a maximum static error $\varepsilon_{\max}$ for each $k = 1\ldots 7$ (Fig. 4.5e), and compare it with the result of Eq. (G.1b) shown by the black line (Fig. 4.5f). We further verified that the latter results do not depend on $\sigma < \sigma_{\max}$.

We have thus confirmed that Eqs. (7.6) provide effective estimates for the range of validity of Eq. (7.3).

References

[1] Michał J Bogdan and Thierry Savin. Fingering instabilities in tissue invasion: an active fluid model. *Royal Society Open Science*, 5(12):181579, 2018.

[2] Michał J. Bogdan and Thierry Savin. Errors in Energy Landscapes Measured with Particle Tracking. *Biophysical Journal*, 115(1):139–149, 2018.

[3] T. E. Angelini, E. Hannezo, X. Trepat, M. Marquez, J. J. Fredberg, and D. A. Weitz. Glass-like dynamics of collective cell migration. *Proceedings of the National Academy of Sciences*, 108(12):4714–4719, 2011.

[4] Peter Friedl and Katarina Wolf. Tumour-cell invasion and migration: diversity and escape mechanisms. *Nature reviews. Cancer*, 3(5):362–74, 2003.

[5] Peter Friedl and Katarina Wolf. Plasticity of cell migration: A multiscale tuning model. *Journal of Cell Biology*, 188(1):11–19, 2010.

[6] Jean Paul Thiery. Epithelial-Mesenchymal transitions in tumour progression. *Nature Reviews*, 2(6):442–454, 2002.

[7] Sandrine Etienne-Manneville. Neighborly relations during collective migration. *Current Opinion in Cell Biology*, 30(1):51–59, 2014.

[8] Anna Haeger, Katarina Wolf, Mirjam M Zegers, and Peter Friedl. Collective cell migration: guidance principles and hierarchies. *Trends in cell biology*, 25(9):556–66, 2015.

[9] Simon Garcia, Edouard Hannezo, Jens Elgeti, Jean-François Joanny, Pascal Silberzan, and Nir S Gov. Physics of active jamming during collective cellular motion in a monolayer. *Proceedings of the National Academy of Sciences of the United States of America*, 112(50):15314–15319, 2015.

[10] Sebastian Aland, Haralambos Hatzikirou, John Lowengrub, and Axel Voigt. A Mechanistic Collective Cell Model for Epithelial Colony Growth and Contact Inhibition. *Biophysical journal*, 109(7):1347–57, oct 2015.

[11] Djordje L. Nikolić, Alistair N Boettiger, Dafna Bar-sagi, Jeffrey D Carbeck, and Stanislav Y Shvartsman. Role of boundary conditions in an experimental model of epithelial wound healing. *American Journal of Physiology*, 08544:68–75, 2006.

[12] Agustí Brugués, Ester Anon, Vito Conte, Jim H Veldhuis, Mukund Gupta, Julien Colombelli, José J Muñoz, G Wayne Brodland, Benoit Ladoux, and Xavier Trepat. Forces driving epithelial wound healing. *Nature Physics*, 10(9):683–690, 2014.

[13] L Petitjean, M Reffay, E. Grasland-Mongrain, M Poujade, B Ladoux, A Buguin, and P Silberzan. Velocity Fields in a Collectively Migrating Epithelium. *Biophysical Journal*, 98(9):1790–1800, 2010.

[14] Romaric Vincent, Elsa Bazellières, Carlos Pérez-González, Marina Uroz, and Xavier Serra-Picamal. Active Tensile Modulus of an Epithelial Monolayer. *Physical Review Letters*, 248103:1–5, 2015.

[15] Anna Kristina Marel, Matthias Zorn, Christoph Klingner, Roland Wedlich-Söldner, Erwin Frey, and Joachim O. Rädler. Flow and diffusion in channel-guided cell migration. *Biophysical Journal*, 107(5):1054–1064, 2014.

[16] Ninna S Rossen, Jens M Tarp, Joachim Mathiesen, Mogens H Jensen, and Lene B Oddershede. Long-range ordered vorticity patterns in living tissue induced by cell division. *Nature Communications*, 5:5720, 2014.

[17] Előd Méhes and Tamás Vicsek. Collective motion of cells: from experiments to models. *Integrative Biology*, 6(9):831–854, 2014.

[18] Sri Ram Krishna Vedula, Man Chun Leong, Tan Lei Lai, Pascal Hersen, Alexandre J Kabla, Chwee Teck Lim, and Benoît Ladoux. Emerging modes of collective cell migration induced by geometrical constraints. *Proceedings of the National Academy of Sciences of the United States of America*, 109(32):12974–9, 2012.

[19] Kenechukwu David Nnetu, Melanie Knorr, Josef Käs, and Mareike Zink. The impact of jamming on boundaries of collectively moving weak-interacting cells. *New Journal of Physics*, 14(11), 2012.

[20] Kevin Doxzen, Sri Ram Krishna Vedula, Man Chun Leong, Hiroaki Hirata, Nir S. Gov, Alexandre J. Kabla, Benoit Ladoux, and Chwee Teck Lim. Guidance of collective cell migration by substrate geometry. *Integrative Biology*, 5:1026–1035, 2013.

[21] Paolo Maiuri, Jean Francois Rupprecht, Stefan Wieser, Verena Ruprecht, Olivier Benichou, Nicolas Carpi, Mathieu Coppey, Simon De Beco, Nir Gov, et al. Actin flows mediate a universal coupling between cell speed and cell persistence. *Cell*, 161(2):374–386, 2015.

[22] B. Szabó, G. J. Szöllösi, B. Gönci, Zs. Jurányi, D. Selmeczi, and Tamás Vicsek. Phase transition in the collective migration of tissue cells: Experiment and model. *Physical Review E*, 74(6):061908, 2006.

[23] Brian A. Camley, Yunsong Zhang, Yanxiang Zhao, Bo Li, Eshel Ben-Jacob, Herbert Levine, and Wouter-Jan Rappel. Polarity mechanisms such as contact inhibition of locomotion regulate persistent rotational motion of mammalian cells on micropatterns. *Proceedings of the National Academy of Sciences*, 111(41):14770–14775, 2014.

[24] H. Wang, M. Naghavi, C. Allen, R. M. Barber, A. Carter, D. C. Casey, F. J. Charlson, A. Z. Chen, M. M. Coates, and Et Al. Global, regional, and national life expectancy, all-cause mortality, and cause-specific mortality for 249 causes of death, 1980–2015: a systematic analysis for the Global Burden of Disease Study 2015. *The Lancet*, 388(10053):1459–1544, 2016.

[25] Arthur W. Lambert, Diwakar R. Pattabiraman, and Robert A. Weinberg. Emerging Biological Principles of Metastasis. *Cell*, 168(4):670–691, 2017.

[26] Andrew J. Ewald, Robert J. Huebner, Hildur Palsdottir, Jessie K. Lee, Melissa J. Perez, Danielle M. Jorgens, Andrew N. Tauscher, Kevin J. Cheung, Zena Werb, and Manfred Auer. Mammary collective cell migration involves transient loss of epithelial features and individual cell migration within the epithelium. *Journal of Cell Science*, 125(11):2638–2654, 2012.

[27] Evelyne Beerling, Daniëlle Seinstra, Elzo de Wit, Lennart Kester, Daphne van der Velden, Carrie Maynard, Ronny Schäfer, Paul van Diest, Emile Voest, Alexander van Oudenaarden, Nienke Vrisekoop, and Jacco van Rheenen. Plasticity between Epithelial and Mesenchymal States Unlinks EMT from Metastasis-Enhancing Stem Cell Capacity. *Cell Reports*, 14(10):2281–2288, 2016.

[28] Liling Wan, Klaus Pantel, and Yibin Kang. Tumor metastasis: moving new biological insights into the clinic. *Nature medicine*, 19(11):1450–64, 2013.

[29] Peter Friedl, Joseph Locker, Erik Sahai, and Jeffrey E. Segall. Classifying collective cancer cell invasion. *Nature Cell Biology*, 14(8):777–783, 2012.

[30] Bettina Weigelin, Gert-Jan Bakker, and Peter Friedl. Third harmonic generation microscopy of cells and tissue organization. *Journal of Cell Science*, 129(2):245–255, 2016.

[31] Anna Haeger, Marina Krause, Katarina Wolf, and Peter Friedl. Cell jamming: Collective invasion of mesenchymal tumor cells imposed by tissue confinement. *Biochimica et Biophysica Acta*, 1840(8):2386–2395, 2014.

[32] Stephanie Alexander and Peter Friedl. Cancer invasion and resistance: Interconnected processes of disease progression and therapy failure. *Trends in Molecular Medicine*, 18(1):13–26, 2012.

[33] Philip Martins Vitorino and Tobias Meyer. Modular Control of Endothelial Sheet Migration. *Genes & Development*, 22(23):3268–3281, 2008.

[34] Yoojin Shin, Sewoon Han, Euiheon Chung, and Seok Chung. Intratumoral phenotypic heterogeneity as an encourager of cancer invasion. *Integrative Biology*, 6(7):654–61, 2014.

[35] Bettina Weigelin, Gert-jan Bakker, and Peter Friedl. Intravital third harmonic generation microscopy of collective melanoma cell invasion. *IntraVital*, 1(1):32–43, 2012.

[36] Katarina Wolf, Yi I. Wu, Yueying Liu, Jörg Geiger, Eric Tam, Christopher Overall, M. Sharon Stack, and Peter Friedl. Multi-step pericellular proteolysis controls the transition from individual to collective cancer cell invasion. *Nature Cell Biology*, 9(8):893–904, 2007.

[37] Stephanie Alexander, Bettina Weigelin, Frank Winkler, and Peter Friedl. Preclinical intravital microscopy of the tumour-stroma interface: Invasion, metastasis, and therapy response. *Current Opinion in Cell Biology*, 25(5):659–671, 2013.

[38] Katarina Wolf, Irina Mazo, Harry Leung, Katharina Engelke, Ulrich H. Von Andrian, Elena I. Deryugina, Alex Y. Strongin, Eva B. Bröcker, and Peter Friedl. Compensation

mechanism in tumor cell migration: Mesenchymal-amoeboid transition after blocking of pericellular proteolysis. *Journal of Cell Biology*, 160(2):267–277, 2003.

[39] Andriy Marusyk, Vanessa Almendro, and Kornelia Polyak. Intra-tumour heterogeneity: a looking glass for cancer? *Nature reviews. Cancer*, 12(5):323–34, 2012.

[40] Kevin J. Cheung, Edward Gabrielson, Zena Werb, and Andrew J. Ewald. Collective invasion in breast cancer requires a conserved basal epithelial program. *Cell*, 155(7):1639–1651, 2013.

[41] Ravikanth Maddipati and Ben Z. Stanger. Pancreatic Cancer Metastases Harbor Evidence of Polyclonality. *Cancer Discovery*, 5(10):37–54, 2015.

[42] Jill M. Westcott, Amanda M. Prechtl, Erin A. Maine, Tuyen T. Dang, Matthew A. Esparza, Han Sun, Yunyun Zhou, Yang Xie, and Gray W. Pearson. An epigenetically distinct breast cancer cell subpopulation promotes collective invasion. *Journal of Clinical Investigation*, 125(5):1927–1943, 2015.

[43] Timothy A. Yap, Marco Gerlinger, P. Andrew Futreal, Lajos Pusztai, and Charles Swanton. Intratumor heterogeneity: Seeing the wood for the trees. *Science Translational Medicine*, 4(127):127ps10–127ps10, 2012.

[44] Michael A. Welte. Bidirectional transport along microtubules. *Current Biology*, 14(13):525–537, 2004.

[45] Lennart Dabelow, Stefano Bo, and Ralf Eichhorn. Irreversibility in Active Matter Systems: Fluctuation Theorem and Mutual Information. *Physical Review X*, 9(2):21009, 2019.

[46] A. P. Solon, Y. Fily, A. Baskaran, M. E. Cates, Y. Kafri, M. Kardar, and J. Tailleur. Pressure is not a state function for generic active fluids. *Nature Physics*, 11(8):673–678, 2015.

[47] Julian Bialké, Jonathan T. Siebert, Hartmut Löwen, and Thomas Speck. Negative Interfacial Tension in Phase-Separated Active Brownian Particles. *Physical Review Letters*, 115(9):1–5, 2015.

[48] Jörn Dunkel, Sebastian Heidenreich, Markus Bär, and Raymond E Goldstein. Minimal continuum theories of structure formation in dense active fluids. *New Journal of Physics*, 15(4):045016, 2013.

[49] V. D. Gordon, M. T. Valentine, M. L. Gardel, D. Andor-Ardó, S. Dennison, A. A. Bogdanov, D. A. Weitz, and T. S. Deisboeck. Measuring the mechanical stress induced by an expanding multicellular tumor system: a case study. *Experimental Cell Research*, 289(1):58–66, 2003.

[50] Olivia du Roure, Alexandre Saez, Axel Buguin, Robert H. Austin, Philippe Chavrier, Pascal Siberzan, and Benoit Ladoux. Force mapping in epithelial cell migration. *Proceedings of the National Academy of Sciences*, 102(7):2390–2395, 2005.

[51] Claudia Mierke, Daniel Rosel, Ben Fabry, and Jan Brabek. Contractile forces in tumor cell migration. *European Journal of Cell Biology*, 87(8):669–676, 2008.

[52] Xavier Trepat, Michael R. Wasserman, Thomas E. Angelini, Emil Millet, David A. Weitz, James P. Butler, and Jeffrey J. Fredberg. Physical forces during collective cell migration. *Nature Physics*, 5(6):426–430, 2009.

[53] C. Blanch-Mercader, R. Vincent, E. Bazellières, X. Serra-Picamal, X. Trepat, and J. Casademunt. Effective viscosity and dynamics of spreading epithelia: a solvable model. *Soft Matter*, 13(6):1235–1243, 2017.

[54] T. J. Mitchison and L. P. Cramer. Actin-based cell motility and cell locomotion. *Cell*, 84(3):371–379, 1996.

[55] R. B. Vaughan and J. P. Trinkaus. Movements of epithelial cell sheets in vitro. *Journal of Cell Science*, 1(4):407–413, 1966.

[56] Markus Basan, Jean Francois Joanny, Jacques Prost, and Thomas Risler. Undulation instability of epithelial tissues. *Physical Review Letters*, 106(15):1–4, 2011.

[57] Jae Hun Kim, Xavier Serra-Picamal, Dhananjay T Tambe, Enhua H Zhou, Chan Young Park, Monirosadat Sadati, Jin-Ah Park, Ramaswamy Krishnan, Bomi Gweon, Emil Millet, James P Butler, Xavier Trepat, and Jeffrey J Fredberg. Propulsion and navigation within the advancing monolayer sheet. *Nature materials*, 12(9):856–63, 2013.

[58] Jacob Notbohm, Shiladitya Banerjee, Kazage J.C. Utuje, Bomi Gweon, Hwanseok Jang, Yongdoo Park, Jennifer Shin, James P. Butler, Jeffrey J. Fredberg, and M. Cristina Marchetti. Cellular Contraction and Polarization Drive Collective Cellular Motion. *Biophysical Journal*, 110(12):2729–2738, 2016.

[59] Thomas E. Angelini, Edouard Hannezo, Xavier Trepat, Jeffrey J. Fredberg, and David A. Weitz. Cell migration driven by cooperative substrate deformation patterns. *Physical Review Letters*, 104(16):1–4, 2010.

[60] Lincoln Paterson. Radial fingering in a Hele Shaw cell. *Journal of Fluid Mechanics*, 113:513–529, 1981.

[61] Thierry Savin, Natasza A. Kurpios, Amy E. Shyer, Patricia Florescu, Haiyi Liang, L. Mahadevan, and Clifford J. Tabin. On the growth and form of the gut. *Nature*, 476(7358):57–63, 2011.

[62] P. Ciarletta. Buckling instability in growing tumor spheroids. *Physical Review Letters*, 110(15):1–5, 2013.

[63] Kevin J. Cheung, Edward Gabrielson, Zena Werb, and Andrew J. Ewald. Collective invasion in breast cancer requires a conserved basal epithelial program. *Cell*, 155(7):1639–1651, 2013.

[64] Laila Ritsma, Ernst J A Steller, Evelyne Beerling, Cindy J M Loomans, Anoek Zomer, Carmen Gerlach, Nienke Vrisekoop, Daniëlle Seinstra, Leon van Gurp, Ronny Schäfer, Daniëlle A Raats, Anko de Graaff, Ton N Schumacher, Eelco J P de Koning, Inne H Borel Rinkes, Onno Kranenburg, and Jacco van Rheenen. Intravital microscopy through an abdominal imaging window reveals a pre-micrometastasis stage during liver metastasis. *Science Translational Medicine*, 4(158):158ra145, 2012.

[65] Laila Ritsma, Nienke Vrisekoop, and Jacco van Rheenen. In vivo imaging and histochemistry are combined in the cryosection labelling and intravital microscopy technique. *Nature Communications*, 4(1):2366, 2013.

[66] Laila Ritsma, Ernst J A Steller, Saskia I J Ellenbroek, Onno Kranenburg, Inne H M Borel Rinkes, and Jacco van Rheenen. Surgical implantation of an abdominal imaging window for intravital microscopy. *Nature Protocols*, 8(3):583–94, 2013.

[67] Saskia I J Ellenbroek and Jacco van Rheenen. Imaging hallmarks of cancer in living mice. *Nature reviews. Cancer*, 14(6):406–18, 2014.

[68] R. Bordel, M. W. Laschke, M. D. Menger, and Brigitte Vollmar. Nicotine does not affect vascularization but inhibits growth of freely transplanted ovarian follicles by inducing granulosa cell apoptosis. *Human Reproduction*, 21(3):610–617, 2006.

[69] Mikael J. Pittet and Ralph Weissleder. Intravital imaging. *Cell*, 147(5):983–991, 2011.

[70] M W Laschke, B Vollmar, and M D Menger. The Dorsal Skinfold Chamber: Window into the Dynamic Interaction of Biomaterials with Their Surrounding Host Tissue. *European Cells and Materials*, 22:147–167, 2011.

[71] Antonia Patsialou, Jose Javier Bravo-Cordero, Yarong Wang, David Entenberg, Huiping Liu, Michael Clarke, and John S. Condeelis. Intravital multiphoton imaging reveals multicellular streaming as a crucial component of in vivo cell migration in human breast tumors. *IntraVital*, 2(2):e25294, 2013.

[72] Anoek Zomer, Carrie Maynard, Frederik Johannes Verweij, Alwin Kamermans, Ronny Schäfer, Evelyne Beerling, Raymond Michel Schiffelers, Elzo de Wit, Jordi Berenguer, Saskia Inge Johanna Ellenbroek, Thomas Wurdinger, Dirk Michiel Pegtel, and Jacco van Rheenen. In Vivo Imaging Reveals Extracellular Vesicle-Mediated Phenocopying of Metastatic Behavior. *Cell*, 161(5):1046–1057, 2015.

[73] Dmitriy Kedrin, Bojana Gligorijevic, Jeffrey Wyckoff, Vladislav V. Verkhusha, John Condeelis, Jeffrey E. Segall, and Jacco van Rheenen. Intravital imaging of metastatic behavior through a mammary imaging window. *Nature Methods*, 5(12):1019–1021, 2008.

[74] Gert Jan Bakker, Volker Andresen, Robert M. Hoffman, and Peter Friedl. Fluorescence lifetime microscopy of tumor cell invasion, drug delivery, and cytotoxicity. *Methods in Enzymology*, 504:109–125, 2012.

[75] Micah Dembo and Yu Li Wang. Stresses at the cell-to-substrate interface during locomotion of fibroblasts. *Biophysical Journal*, 76(4):2307–2316, 1999.

[76] James P. Butler, Iva Marija Toli-Nørrelykke, Ben Fabry, and Jeffrey J. Fredberg. Traction fields, moments, and strain energy that cells exert on their surroundings. *American Journal of Physiology - Cell Physiology*, 282(3):C595–C605, 2002.

[77] Rudolf Merkel, Norbert Kirchgeßner, Claudia M. Cesa, and Bernd Hoffmann. Cell force microscopy on elastic layers of finite thickness. *Biophysical Journal*, 93(9):3314–3323, 2007.

[78] Benedikt Sabass, Margaret L. Gardel, Clare M. Waterman, and Ulrich S. Schwarz. High resolution traction force microscopy based on experimental and computational advances. *Biophysical Journal*, 94(1):207–220, 2008.

[79] Silke Henkes, Yaouen Fily, and M. Cristina Marchetti. Active jamming: Self-propelled soft particles at high density. *Physical Review E - Statistical, Nonlinear, and Soft Matter Physics*, 84(4):84–87, 2011.

[80] Victoria Tarle, Andrea Ravasio, Vincent Hakim, and Nir S. Gov. Modeling the finger instability in an expanding cell monolayer. *Integrative Biology*, 7:1218–1227, 2015.

[81] Markus Basan, Jens Elgeti, Edouard Hannezo, W.-J. Wouter-Jan Rappel, and Herbert Levine. Alignment of cellular motility forces with tissue flow as a mechanism for efficient wound healing. *Proceedings of the National Academy of Sciences of the United States of America*, 110(7):2452–9, 2013.

[82] Adrien Hallou, Joel Jennings, and Alexandre J. Kabla. Tumour heterogeneity promotes collective invasion and cancer metastatic dissemination. *Royal Society Open Science*, 4(8):161007, 2017.

[83] A Szabó, R Ünnep, E Méhes, W O Twal, W S Argraves, Y Cao, and A Czirók. Collective cell motion in endothelial monolayers. *Physical Biology*, 7(4):46007, 2010.

[84] Felix J. Segerer, Florian Thuroff, Alicia Piera Alberola, Erwin Frey, and Joachim O. Radler. Emergence and persistence of collective cell migration on small circular micropatterns. *Physical Review Letters*, 114(22):1–5, 2015.

[85] James A. Glazier and François Graner. Simulation of the differential adhesion driven rearrangement of biological cells. *Physical Review E*, 47(3):2128–2154, 1993.

[86] G. Wayne Brodland and Jim H. Veldhuis. The Mechanics of Metastasis: Insights from a Computational Model. *PLoS ONE*, 7(9):e44281, 2012.

[87] Dapeng Bi, Xingbo Yang, M Cristina Marchetti, and M Lisa Manning. Motility-Driven Glass and Jamming Transitions in Biological Tissues. *Physical Review X*, 6(2):021011, 2016.

[88] Joel Jennings. *A New Computational Model for Multi-Cellular Biological Systems*. PhD thesis, University of Cambridge, 2014.

[89] Mark Alber, Nan Chen, Pavel M. Lushnikov, and Stuart A. Newman. Continuous macroscopic limit of a discrete stochastic model for interaction of living cells. *Physical Review Letters*, 99(16):1–4, 2007.

[90] Javier Palacio-Torralba, Steven Hammer, Daniel W. Good, S. Alan McNeill, Grant D. Stewart, Robert L. Reuben, and Yuhang Chen. Quantitative diagnostics of soft tissue through viscoelastic characterization using time-based instrumented palpation. *Journal of the Mechanical Behavior of Biomedical Materials*, 41:149–160, 2015.

[91] Edward K. Rodriguez. Stress-dependent finite growth in soft elastic tissues. *Journal of Biomechanics*, 27(4):455–467, 1994.

[92] Alain Goriely and Martine Ben Amar. Differential growth and instability in elastic shells. *Physical Review Letters*, 94(19):1–4, 2005.

[93] D. Ambrosi and F. Mollica. On the mechanics of a growing tumor. *International Journal of Engineering Science*, 40(12):1297–1316, 2002.

[94] Julien Dervaux and Martine Ben Amar. Morphogenesis of growing soft tissues. *Physical Review Letters*, 101(6):1–4, 2008.

[95] Martine Ben Amar and Alain Goriely. Growth and instability in elastic tissues. *Journal of the Mechanics and Physics of Solids*, 53(10):2284–2319, 2005.

[96] Martine Ben Amar and Pasquale Ciarletta. Swelling instability of surface-attached gels as a model of soft tissue growth under geometric constraints. *Journal of the Mechanics and Physics of Solids*, 58(7):935–954, 2010.

[97] V. Pettinati, D. Ambrosi, and P. Ciarletta. Active Stress as a Local Regulator of Global Size in Morphogenesis. *International Journal of Non-Linear Mechanics*, 75:5–14, 2015.

[98] Michael H. Köpf and Len M. Pismen. A continuum model of epithelial spreading. *Soft Matter*, 9(14):3727, 2013.

[99] Jonas Ranft, Markus Basan, Jens Elgeti, Jean-françois Joanny, Jacques Prost, and Frank Jülicher. Fluidization of tissues by cell division and apoptosis. *Proceedings of the National Academy of Sciences of the United States of America*, 107(49):20863–20868, 2010.

[100] Jonas M Ranft. *Mechanics of Growing Tissues: A Continuum Description Approach.* PhD thesis, l'Université Pierre et Marie Curie, 2012.

[101] E Hannezo, J Prost, and J-F Joanny. Growth, homeostatic regulation and stem cell dynamics in tissues. *Journal of the Royal Society Interface*, 11:20130895, 2014.

[102] Thomas Risler, Aurelien Peilloux, and Jacques Prost. Homeostatic Fluctuations of a Tissue Surface. *Physical Review Letters*, 115(25):258104, 2015.

[103] P. Tracqui. Biophysical models of tumour growth. *Reports on Progress in Physics*, 72(5):056701, 2009.

[104] Vittorio Cristini, John Lowengrub, and Qing Nie. Nonlinear simulation of tumor growth. *Journal of Mathematical Biology*, 46(3):191–224, 2003.

[105] Julia C Arciero, Qi Mi, Maria F Branca, David J Hackam, and David Swigon. Continuum Model of Collective Cell Migration in Wound Healing and Colony Expansion. *Biophysical Journal*, 100:535–543, 2011.

[106] Andrea Ravasio, Ibrahim Cheddadi, Tianchi Chen, Telmo Pereira, Hui Ting Ong, Cristina Bertocchi, Agusti Brugues, Antonio Jacinto, Alexandre J Kabla, Yusuke Toyama, Xavier Trepat, Nir Gov, Luís Neves de Almeida, and Benoit Ladoux. Gap geometry dictates epithelial closure efficiency. *Nature Communications*, 6:7683, 2015.

[107] John Toner and Yuhai Tu. Long-range order in a two-dimensional dynamical XY model: How birds fly together. *Physical Review Letters*, 75(23):4326–4329, 1995.

[108] John Toner and Yuhai Tu. Flocks, herds, and schools: A quantitative theory of flocking. *Physical Review E*, 58(4):4828–4858, 1998.

[109] John Toner, Yuhai Tu, and Sriram Ramaswamy. Hydrodynamics and phases of flocks. *Annals of Physics*, 318(1 SPEC. ISS.):170–244, 2005.

[110] Hugo Wioland, Francis G. Woodhouse, Jörn Dunkel, John O. Kessler, and Raymond E. Goldstein. Confinement stabilizes a bacterial suspension into a spiral vortex. *Physical Review Letters*, 110(26):1–5, 2013.

[111] J. Zimmermann, M. Basan, and H. Levine. An instability at the edge of a tissue of collectively migrating cells can lead to finger formation during wound healing. *European Physical Journal: Special Topics*, 223(7):1259–1264, 2014.

[112] David Nesbitt, Gunnar Pruessner, and Chiu Fan Lee. Edge instability in incompressible planar active fluids. *Physical Review E*, 96(6):1–7, 2017.

[113] Shiladitya Banerjee, Kazage J C Utuje, and M. Cristina Marchetti. Propagating Stress Waves during Epithelial Expansion. *Physical Review Letters*, 114(22):228101, 2015.

[114] Ricard Alert, Carles Blanch-Mercader, and Jaume Casademunt. Active fingering instability in tissue spreading. *Physical Review Letters*, 122(8):88104, 2019.

[115] Amarender Nagilla, Ranganathan Prabhakar, and Sameer Jadhav. Linear stability of an active fluid interface. *Physics of Fluids*, 30(2):022109, 2018.

[116] Shirley Mark, Roie Shlomovitz, Nir S Gov, Mathieu Poujade, Erwan Grasland-mongrain, and Pascal Silberzan. Physical Model of the Dynamic Instability in an Expanding Cell Culture. *Biophysical Journal*, 98(3):361–370, 2010.

[117] Philip Geoffrey Saffman and Geoffrey Ingram Taylor. The penetration of a fluid into a porous medium or Hele-Shaw cell containing a more viscous liquid. *Proceedings of the Royal Society A: Mathematical, Physical and Engineering Sciences*, 245(1242):312–329, 1958.

[118] Mireille Lambert, Olivier Thoumine, Julien Brevier, Daniel Choquet, Daniel Riveline, and René Marc Mège. Nucleation and growth of cadherin adhesions. *Experimental Cell Research*, 313(19):4025–4040, 2007.

[119] Ian Y Wong, Sarah Javaid, Elisabeth A Wong, Sinem Perk, Daniel A Haber, Mehmet Toner, and Daniel Irimia. Collective and individual migration following the epithelial-mesenchymal transition. *Nature materials*, 13(11):1063–71, 2014.

[120] Maren Diepenbruck and Gerhard Christofori. Epithelial–mesenchymal transition (EMT) and metastasis: yes, no, maybe? *Current Opinion in Cell Biology*, 43:7–13, 2016.

[121] C. Blanch-Mercader and J. Casademunt. Hydrodynamic instabilities, waves and turbulence in spreading epithelia. *Soft Matter*, 13(38):6913–6928, 2017.

[122] D. A. Beysens, G. Forgacs, and J. A. Glazier. Cell sorting is analogous to phase ordering in fluids. *Proceedings of the National Academy of Sciences*, 97(17):9467–9471, 2000.

[123] Philippe Marmottant, Abbas Mgharbel, Jos Käfer, Benjamin Audren, Jean Paul Rieu, Jean Claude Vial, Boudewijn Van Der Sanden, Athanasius F.M. Marée, François Graner, and Hélène Delanoë-Ayari. The role of fluctuations and stress on the effective viscosity of cell aggregates. *Proceedings of the National Academy of Sciences*, 106(45):19204, 2009.

[124] Lyubov E. Shimolina, Maria Angeles Izquierdo, Ismael López-Duarte, James A. Bull, Marina V. Shirmanova, Larisa G. Klapshina, Elena V. Zagaynova, and Marina K. Kuimova. Imaging tumor microscopic viscosity in vivo using molecular rotors. *Scientific Reports*, 7:41097, 2017.

[125] H. H. Wensink, J. Dunkel, S. Heidenreich, K. Drescher, R. E. Goldstein, H. Lowen, and J. M. Yeomans. Meso-scale turbulence in living fluids. *Proceedings of the National Academy of Sciences*, 109(36):14308–14313, 2012.

[126] David Selmeczi, Stephan Mosler, Peter H. Hagedorn, Niels B. Larsen, and Henrik Flyvbjerg. Cell Motility as Persistent Random Motion: Theories from Experiments. *Biophysical Journal*, 89(2):912–931, 2005.

[127] Rizwan Farooqui and Gabriel Fenteany. Multiple rows of cells behind an epithelial wound edge extend cryptic lamellipodia to collectively drive cell-sheet movement. *Journal of Cell Science*, 118(1):51–63, 2005.

[128] Jes K. Klarlund. Dual modes of motility at the leading edge of migrating epithelial cell sheets. *Proceedings of the National Academy of Sciences*, 109(39):15799–15804, 2012.

[129] Tilo Pompe, Martin Kaufmann, Maria Kasimir, Stephanie Johne, Stefan Glorius, Lars Renner, Manfred Bobeth, Wolfgang Pompe, and Carsten Werner. Friction-controlled traction force in cell adhesion. *Biophysical Journal*, 101(8):1863–70, 2011.

[130] Revathi Ananthakrishnan and Allen Ehrlicher. The forces behind cell movement. *International Journal of Biological Sciences*, 3(5):303–317, 2007.

[131] M. Lisa Manning, Ramsey A. Foty, Malcolm S. Steinberg, and Eva-Maria Schoetz. Coaction of intercellular adhesion and cortical tension specifies tissue surface tension. *Proceedings of the National Academy of Sciences*, 107(28):12517–12522, 2010.

[132] Thomas Lecuit and Pierre François Lenne. Cell surface mechanics and the control of cell shape, tissue patterns and morphogenesis. *Nature Reviews Molecular Cell Biology*, 8(8):633–644, 2007.

[133] Ramsey A. Foty, Gabor Forgacs, Cathie M. Pfleger, and Malcolm S. Steinberg. Liquid properties of embryonic tissues: Measurement of interfacial tensions. *Physical Review Letters*, 72(14):2298–2301, 1994.

[134] Assaf Zaritsky, Doron Kaplan, Inbal Hecht, Sari Natan, Lior Wolf, Nir S. Gov, Eshel Ben-Jacob, and Ilan Tsarfaty. Propagating Waves of Directionality and Coordination Orchestrate Collective Cell Migration. *PLoS Computational Biology*, 10(7):15–19, 2014.

[135] Assaf Zaritsky, Erik S Welf, Yun-yu Tseng, M Angeles Rabadan, Xavier Serra-picamal, Xavier Trepat, and Danuser Gaudenz. Seeds of Locally Aligned Motion and Stress Coordinate a Collective Cell Migration. *Biophysical Journal*, 109(12):2492–2500, 2015.

[136] Xingbo Yang and M. Cristina Marchetti. Hydrodynamics of Turning Flocks. *Physical Review Letters*, 115(25):1–5, 2015.

[137] M Cristina Marchetti, Yaouen Fily, Silke Henkes, Adam Patch, and David Yllanes. Minimal model of active colloids highlights the role of mechanical interactions in controlling the emergent behavior of active matter. *Current Opinion in Colloid & Interface Science*, 21(12):34–43, 2016.

[138] A. C. Callan-Jones, J. F. Joanny, and J. Prost. Viscous-fingering-like instability of cell fragments. *Physical Review Letters*, 100(25):27–30, 2008.

[139] Jonas Ranft, Maryam Aliee, Jacques Prost, Frank Jülicher, and Jean-François Joanny. Mechanically driven interface propagation in biological tissues. *New Journal of Physics*, 16(3):035002, 2014.

[140] Manfredo Perdigão Do Carmo. *Differential Geometry of Curves and Surfaces*. Prentice-Hall, Englewood Cliffs, N.J., January 1976.

[141] Steve Pawlizak, Anatol W. Fritsch, Steffen Grosser, Dave Ahrens, Tobias Thalheim, Stefanie Riedel, Tobias R. Kiessling, Linda Oswald, Mareike Zink, M. Lisa Manning, and Josef A. Käs. Testing the differential adhesion hypothesis across the epithelial-mesenchymal transition. *New Journal of Physics*, 17(8):83049, 2015.

[142] C. Flament, G. Pacitto, J. C. Bacri, I. Drikis, and A. Cebers. Viscous fingering in a magnetic fluid. I. Radial Hele-Shaw flow. *Physics of Fluids*, 10(10):2464–2472, 1998.

[143] M. Poujade, E. Grasland-Mongrain, A. Hertzog, J. Jouanneau, P. Chavrier, B. Ladoux, A. Buguin, and P. Silberzan. Collective migration of an epithelial monolayer in response to a model wound. *Proceedings of the National Academy of Sciences*, 104(41):15988–15993, 2007.

[144] Eduardo O. Dias and José A. Miranda. Wavelength selection in Hele-Shaw flows: A maximum-amplitude criterion. *Physical Review E - Statistical, Nonlinear, and Soft Matter Physics*, 88(1):1–6, 2013.

[145] H. Rodney Withers and Steve P. Lee. Modeling growth kinetics and statistical distribution of oligometastases. *Seminars in Radiation Oncology*, 16(2):111–119, 2006.

[146] Alexander B. Herman, Van M. Savage, and Geoffrey B. West. A Quantitative Theory of Solid Tumor Growth, Metabolic Rate and Vascularization. *PLoS ONE*, 6(9):e22973, 2011.

[147] Caterina Guiot, Piero Giorgio Degiorgis, Pier Paolo Delsanto, Pietro Gabriele, and Thomas S. Deisboeck. Does tumor growth follow a “universal law”? *Journal of Theoretical Biology*, 225(2):147–151, 2003.

[148] Sébastien Benzekry, Clare Lamont, Afshin Beheshti, Amanda Tracz, John M. L. Ebos, Lynn Hlatky, and Philip Hahnfeldt. Classical Mathematical Models for Description and Prediction of Experimental Tumor Growth. *PLoS Computational Biology*, 10(8):e1003800, 2014.

[149] Brian S Winters, Scott R Shepard, and Ramsey A Foty. Biophysical measurement of brain tumor cohesion. *International Journal of Cancer*, 14(3):371–379, 2005.

[150] Christine M. Butler and Ramsey A. Foty. Measurement of aggregate cohesion by tissue surface tensiometry. *Journal of Visualized Experiments*, 50:e2739, 2011.

[151] Kaspar Josche Streitberger, Ledia Lilaj, Felix Schrank, Jürgen Braun, Karl Titus Hoffmann, Martin Reiss-Zimmermann, Josef A. Käs, and Ingolf Sack. How tissue fluidity influences brain tumor progression. *Proceedings of the National Academy of Sciences of the United States of America*, 117(1):128–134, 2020.

[152] Marina K. Kuimova. Mapping viscosity in cells using molecular rotors. *Physical Chemistry Chemical Physics*, 14(37):12671–12686, 2012.

[153] Ming Guo, Allen J. Ehrlicher, Mikkel H. Jensen, Malte Renz, Jeffrey R. Moore, Robert D. Goldman, Jennifer Lippincott-Schwartz, Frederick C. Mackintosh, and David A. Weitz. Probing the stochastic, motor-driven properties of the cytoplasm using force spectrum microscopy. *Cell*, 158(4):822–832, 2014.

[154] Casey M. Kraning-Rush, Joseph P. Califano, and Cynthia A. Reinhart-King. Cellular traction stresses increase with increasing metastatic potential. *PLoS ONE*, 7(2):e32572, 2012.

[155] Hyeon-gi Kim, A. Ram Yu, Jae Joon Lee, Yong Jin Lee, Sang Moo Lim, and Jin Su Kim. Measurement of Tumor Pressure and Strategies of Imaging Tumor Pressure for Radioimmunotherapy. *Nuclear Medicine and Molecular Imaging*, 53(4):235–241, 2019.

[156] Yves Boucher, Laurence T. Baxter, and Rakesh K. Jain. Interstitial Pressure Gradients in Tissue-isolated and Subcutaneous Tumors: Implications for Therapy. *Cancer Research*, 50(15):4478–4484, 1990.

[157] Erik Meijering, Oleh Dzyubachyk, and Ihor Smal. Methods for Cell and Particle Tracking. In *Imaging and Spectroscopic Analysis of Living Cells - Optical and Spectroscopic Techniques*, pages 183–200. Elsevier, 2012.

[158] Nicolas Chenouard, Ihor Smal, Fabrice de Chaumont, Martin Maška, Ivo F Sbalzarini, Yuanhao Gong, Janick Cardinale, Craig Carthel, Stefano Coraluppi, Mark Winter, Andrew R Cohen, William J Godinez, Karl Rohr, Yannis Kalaidzidis, Liang Liang, James Duncan, Hongying Shen, Yingke Xu, Klas E G Magnusson, Joakim Jaldén, Helen M Blau, Perrine Paul-Gilloteaux, Philippe Roudot, Charles Kervrann, François Waharte, Jean-Yves Tinevez, Spencer L Shorte, Joost Willemse, Katherine Celler, Gilles P van Wezel, Han-Wei Dan, Yuh-Show Tsai, Carlos Ortiz de Solórzano, Jean-Christophe Olivo-Marin, and Erik Meijering. Objective comparison of particle tracking methods. *Nature methods*, 11(3):281–9, 2014.

[159] Carlo Manzo and Maria F Garcia-Parajo. A review of progress in single particle tracking: from methods to biophysical insights. *Reports on Progress in Physics*, 78(12):124601, 2015.

[160] Sébastien Courty, Camilla Luccardini, Yohanns Bellaiche, Giovanni Cappello, and Maxime Dahan. Tracking Individual Kinesin Motors in Living Cells Using Single Quantum-Dot Imaging. *Nano Lett.*, 6(7):1491–1495, July 2006.

[161] Mohamed El Beheiry, Maxime Dahan, and Jean-Baptiste Masson. InferenceMAP: mapping of single-molecule dynamics with Bayesian inference. *Nat. Neurosci.*, 12(7):594–595, July 2015.

[162] Rudolf Simson, Erin D Sheets, and Ken Jacobson. Detection of temporary lateral confinement of membrane proteins using single-particle tracking analysis. *Biophysical Journal*, 69(3):989–993, 1995.

[163] G I Mashanov and J E Molloy. Automatic Detection of Single Fluorophores in Live Cells. *Biophysical Journal*, 92(6):2199–2211, 2007.

[164] Boerries Brandenburg and Xiaowei Zhuang. Virus trafficking - learning from single-virus tracking. *Nature Reviews. Microbiology*, 5(3):197–208, 2007.

[165] W. J. Godinez, M. Lampe, S. Wörz, B. Müller, R. Eils, and K. Rohr. Deterministic and probabilistic approaches for tracking virus particles in time-lapse fluorescence microscopy image sequences. *Medical Image Analysis*, 13(2):325–342, 2009.

[166] Ryohei Yasuda, Hidetake Miyata, and Kazuhiko Kinosita Jr. Direct Measurement of the Torsional Rigidity of Single Actin Filaments. *Journal of Molecular Biology*, 263(2):227–236, 1996.

[167] Loïc Le Goff, Oskar Hallatschek, Erwin Frey, and François Amblard. Tracer Studies on F-Actin Fluctuations. *Physics Review Letters*, 89(25):258101, 2002.

[168] Songwan Jin, Peter M. Haggie, and Alan S. Verkman. Single-particle tracking of membrane protein diffusion in a potential: Simulation, detection, and application to confined diffusion of CFTR Cl-channels. *Biophysical Journal*, 93(3):1079–1088, 2007.

[169] Bernd Nöding and Sarah Köster. Intermediate Filaments in Small Configuration Spaces. *Physics Review Letters*, 108(8):088101, 2012.

[170] Kevin D. Dorfman, Scott B. King, Daniel W. Olson, Joel D. P. Thomas, and Douglas R. Tree. Beyond Gel Electrophoresis: Microfluidic Separations, Fluorescence Burst Analysis, and DNA Stretching. *Chemical Reviews*, 113(4):2584–2667, 2013.

[171] Megan C. Engel, Dustin B. Ritchie, Daniel AN. Foster, Kevin S. D. Beach, and Michael T. Woodside. Reconstructing Folding Energy Landscape Profiles from Nonequilibrium Pulling Curves with an Inverse Weierstrass Integral Transform. *Physics Review Letters*, 113(23):238104, 2014.

[172] H. Qian, M. P. Sheetz, and E. L. Elson. Single particle tracking. Analysis of diffusion and flow in two-dimensional systems. *Biophysical Journal*, 60(4):910–921, 1991.

[173] Michael J. Saxton. Single-particle tracking: The distribution of diffusion coefficients. *Biophysical Journal*, 72(4):1744–1753, 1997.

[174] Nicolas Fatin-Rouge, Konstantin Starchev, and Jacques Buffle. Size effects on diffusion processes within agarose gels. *Biophysical Journal*, 86(5):2710–2719, 2004.

[175] Thomas A. Waigh. Advances in the microrheology of complex fluids. *Reports on Progress in Physics*, 79(7):074601, 2016.

[176] John C. Crocker and David G. Grier. Interactions and dynamics in charge-stabilized colloids. *MRS Bulletin*, 23(10):24–31, 1998.

[177] John C. Crocker and David G. Grier. Microscopic Measurement of the Pair Interaction Potential of Charge-Stabilized Colloid. *Physical Review Letters*, 73(2):352–356, 1994.

[178] J. C. Crocker, J. A. Matteo, A. D. Dinsmore, and A. G. Yodh. Entropic attraction and repulsion in binary colloids probed with a line optical tweezer. *Physical Review Letters*, 82(21):4352–4355, 1999.

[179] K. Lin, J. C. Crocker, A. C. Zeri, and A. G. Yodh. Colloidal interactions in suspensions of rods. *Physical Review Letters*, 87(8):088301, 2001.

[180] Nassiredin Mojarad and Madhavi Krishnan. Measuring the size and charge of single nanoscale objects in solution using an electrostatic fluidic trap. *Nature Nanotechnology*, 7(7):448–452, 2012.

[181] Madhavi Krishnan, Nassiredin Mojarad, Philipp Kukura, and Vahid Sandoghdar. Geometry-induced electrostatic trapping of nanometric objects in a fluid. *Nature*, 467(7316):692–695, 2010.

[182] Nassir Mojarad, Vahid Sandoghdar, and Madhavi Krishnan. Measuring three-dimensional interaction potentials using optical interference. *Optics Express*, 21(8):1194–1203, 2013.

[183] Stefano Pagliara, Christian Schwall, and Ulrich F. Keyser. Optimizing diffusive transport through a synthetic membrane channel. *Advanced Materials*, 25(6):844–849, 2013.

[184] Nathanael Hoze, Deepak Nair, Eric Hosy, Christian Sieben, Suliana Manley, and Andreas Herrmann. Heterogeneity of AMPA receptor trafficking and molecular interactions revealed by superresolution analysis of live cell imaging. *Proceedings of the National Academy of Sciences*, 109(42), 2012.

[185] Jean-Baptiste Masson, Patrice Dionne, Charlotte Salvatico, Marianne Renner, Christian G. Specht, Antoine Triller, and Maxime Dahan. Mapping the Energy and Diffusion Landscapes of Membrane Proteins at the Cell Surface Using High-Density Single-Molecule Imaging and Bayesian Inference: Application to the Multiscale Dynamics of Glycine Receptors in the Neuronal Membrane. *Biophysical Journal*, 106(1):74–83, 2014.

[186] Ritu Verma, J. C. Crocker, T. C. Lubensky, and A. G. Yodh. Entropic colloidal interactions in concentrated DNA Solutions. *Physical Review Letters*, 81(18):4004–4007, 1998.

[187] M K Cheezum, W F Walker, and W H Guilford. Quantitative comparison of algorithms for tracking single fluorescent particles. *Biophysical Journal*, 81(4):2378–2388, 2001.

[188] I. Smal, K. Draegestein, N. Galjart, W. Niessen, and E. Meijering. Particle Filtering for Multiple Object Tracking in Dynamic Fluorescence Microscopy Images: Application to Microtubule Growth Analysis. *IEEE Transactions on Medical Imaging*, 27(6):789–804, 2008.

[189] Douglas S. Martin, Martin B. Forstner, and Josef A. Käs. Apparent Subdiffusion Inherent to Single Particle Tracking. *Biophysical Journal*, 83(4):2109–2117, 2002.

[190] Thierry Savin and Patrick S. Doyle. Static and Dynamic Errors in Particle Tracking Microrheology. *Biophysical Journal*, 88(1):623–638, 2005.

[191] Thierry Savin and Patrick S. Doyle. Role of a finite exposure time on measuring an elastic modulus using microrheology. *Physical Review E - Statistical, Nonlinear, and Soft Matter Physics*, 71(4):6–11, 2005.

[192] Ken Ritchie, Xiao Yuan Shan, Junko Kondo, Kokoro Iwasawa, Takahiro Fujiwara, and Akihiro Kusumi. Detection of non-Brownian diffusion in the cell membrane in single molecule tracking. *Biophysical Journal*, 88(3):2266–2277, 2005.

[193] Wesley P. Wong and Ken Halvorsen. The effect of integration time on fluctuation measurements: calibrating an optical trap in the presence of motion blur. *Optics Express*, 14(25):227–236, 2006.

[194] Astrid van der Horst and Nancy R. Forde. Power spectral analysis for optical trap stiffness calibration from high-speed camera position detection with limited bandwidth. *Optics Express*, 18(8):7670–7677, 2010.

[195] Xavier Michalet. Mean square displacement analysis of single-particle trajectories with localization error: Brownian motion in an isotropic medium. *Physical Review E*, 82(4):041914, 2010.

[196] Andrew J. Berglund. Statistics of camera-based single-particle tracking. *Physical Review E - Statistical, Nonlinear, and Soft Matter Physics*, 82(1):1–8, 2010.

[197] Ian C. Jenkins, John C. Crocker, and Talid Sinno. Interaction potentials from arbitrary multi-particle trajectory data. *Soft Matter*, 11(35):6948–6956, 2015.

[198] N. Hoze and D. Holcman. Recovering a stochastic process from super-resolution noisy ensembles of single-particle trajectories. *Physics Review E*, 92(5):052109, 2015.

[199] Christopher P. Calderon. Motion blur filtering: A statistical approach for extracting confinement forces and diffusivity from a single blurred trajectory. *Physics Review E*, 93(5):053303, 2016.

[200] Stanislav Burov, Patrick Figliozzi, Binhua Lin, Stuart A. Rice, Norbert F. Scherer, and Aaron R. Dinner. Single-pixel interior filling function approach for detecting and correcting errors in particle tracking. *Proceedings of the National Academy of Sciences*, 114(2):221–226, 2017.

[201] Nathanaël Hozé and David Holcman. Statistical Methods for Large Ensembles of Super-Resolution Stochastic Single Particle Trajectories in Cell Biology. *Annual Review of Statistics and Its Application*, 4(1):189–223, 2017.

[202] Thierry Savin, Patrick T. Spicer, and Patrick S. Doyle. A rational approach to noise discrimination in video microscopy particle tracking. *Applied Physics Letters*, 93(2):024102, 2008.

[203] Rachel M. Lee, Haicen Yue, Wouter-Jan Rappel, Wolfgang Losert, and Rachel M. Lee. Inferring single-cell behaviour from large- scale epithelial sheet migration patterns. *Journal of the Royal Society Interface*, 14(130):20170147, 2017.

[204] Lene Oddershede, Jakob Kisbye Dreyer, Sonia Grego, Stanley Brown, and Kirstine Berg-Sørensen. The Motion of a Single Molecule, the λ-Receptor, in the Bacterial Outer Membrane. *Biophysical Journal*, 83(6):3152–3161, 2002.

[205] M. Keller, J. Schilling, and Erich Sackmann. Oscillatory magnetic bead rheometer for complex fluid microrheometry. *Review of Scientific Instruments*, 72(9):3626–3634, 2001.

[206] Christian L. Vestergaard. Optimizing experimental parameters for tracking of diffusing particles. *Physical Review E*, 94(2):022401, 2016.

[207] J.-B. Masson, D. Casanova, S. Türkcan, G. Voisinne, M. R. Popoff, M. Vergassola, and A. Alexandrou. Inferring Maps of Forces inside Cell Membrane Microdomains. *Physical Review Letters*, 102(4):048103, 2009.

[208] Hans Christian Öttinger. *Stochastic Processes in Polymeric Fluids: Tools and Examples for Developing Simulation Algorithms*. Springer, Berlin, 1996.

[209] Izabela K. Piechocka, Rommel G. Bacabac, Max Potters, Fred C. MacKintosh, and Gijsje H. Koenderink. Structural Hierarchy Governs Fibrin Gel Mechanics. *Biophysical Journal*, 98(10):2281–2289, 2010.

[210] Mohammad Sarshar, Winson T. Wong, and Bahman Anvari. Comparative study of methods to calibrate the stiffness of a single-beam gradient-force optical tweezers over various laser trapping powers. *Journal of Biomedical Optics*, 19(11):115001, 2014.

[211] Philip Jones, Onofrio Marago, and Giovanni Volpe. *Optical Tweezers*. Principles and Applications. Cambridge University Press, Cambridge, 2015.

[212] Moshe Lindner, Guy Nir, Shlomi Medalion, Heidelinde R. C. Dietrich, Yitzhak Rabin, and Yuval Garini. Force-free measurements of the conformations of DNA molecules tethered to a wall. *Physical Review E - Statistical, Nonlinear, and Soft Matter Physics*, 83(1):1–7, 2011.

[213] Peter F. J. May, Justin N. M. Pinkney, Pawel Zawadzki, Geraint W. Evans, David J. Sherratt, and Achillefs N. Kapanidis. Tethered fluorophore motion: Studying large DNA conformational changes by single-fluorophore imaging. *Biophysical Journal*, 107(5):1205–1216, 2014.

[214] Gerrit Sitters, Niels Laurens, Emile de Rijk, Holger Kress, Erwin J. G. Peterman, and Gijs J. L. Wuite. Optical Pushing: A Tool for Parallelized Biomolecule Manipulation. *Biophysical Journal*, 110(1):44–50, 2016.

[215] Elizabeth J. Akin, Laura Solé, Ben Johnson, Mohamed El Beheiry, Jean-Baptiste Masson, Diego Krapf, and Michael M. Tamkun. Single-Molecule Imaging of Nav1.6 on the Surface of Hippocampal Neurons Reveals Somatic Nanoclusters. *Biophysical Journal*, 111(6):1235–1247, 2016.

[216] M. A. Kotlarchyk, E. L. Botvinick, and A. J. Putnam. Characterization of hydrogel microstructure using laser tweezers particle tracking and confocal reflection imaging. *Journal of Physics Condensed Matter*, 22(19):194121, 2010.

[217] Silvan Türkcan, Jean-Baptiste Masson, Didier Casanova, Geneviève Mialon, Thierry Gacoin, Jean-Pierre Boilot, Michel R. Popoff, and Antigoni Alexandrou. Observing the Confinement Potential of Bacterial Pore-Forming Toxin Receptors Inside Rafts with Nonblinking Eu3+-Doped Oxide Nanoparticles. *Biophysical Journal*, 102(10):2299–2308, 2012.

[218] Silvan Türkcan, Antigoni Alexandrou, and Jean-Baptiste Masson. A Bayesian Inference Scheme to Extract Diffusivity and Potential Fields from Confined Single-Molecule Trajectories. *Biophysical Journal*, 102(10):2288–2298, 2012.

[219] Silvan Türkcan, Maximilian U. Richly, Antigoni Alexandrou, and Jean-Baptiste Masson. Probing membrane protein interactions with their lipid raft environment using single-molecule tracking and Bayesian inference analysis. *PLoS ONE*, 8(1):e53073, 2013.

[220] Jacob N. Israelachvili. *Intermolecular and Surface Forces.* Academic Press, San Diego, 3rd edition, 2011.

[221] A. W. C. Lau, Keng Hui Lin, and A. G. Yodh. Entropic interactions in suspensions of semiflexible rods: Short-range effects of flexibility. *Physical Review E*, 66(2):1–4, 2002.

[222] Yizhou Tan, Jannes Gladrow, Ulrich F. Keyser, Leonardo Dagdug, and Stefano Pagliara. Particle transport across a channel via an oscillating potential. *Physical Review E*, 96(5):052401, 2017.

[223] Megan T. Valentine, P. D. Kaplan, D. Thota, John C. Crocker, T. Gisler, R. K. Prud'homme, M. Beck, and David A. Weitz. Investigating the microenvironments of inhomogeneous soft materials with multiple particle tracking. *Physical Review E*, 64(6):061506, 2001.

[224] John C. Crocker, Megan T. Valentine, Eric R. Weeks, T. Gisler, P. D. Kaplan, Arjun G. Yodh, and David A. Weitz. Two-Point Microrheology of Inhomogeneous Soft Materials. *Physical Review Letters*, 85(4):888–891, 2000.

[225] Jaume Casademunt. Viscous fingering as a paradigm of interfacial pattern formation: Recent results and new challenges. *Chaos*, 14(3):809–824, 2004.

[226] Philip R. Bevington and D. Keith Robinson. *Data Reduction and Error Analysis for the Physical Sciences.* McGraw-Hill, New York, 3rd edition, 2003.